IN THE NAME OF ALLAH, THE MOST BENEFICIENT,
THE MOST GRACIOUS, THE MOST MERCIFUL

Boundary Layer Flow of Micropolar Fluid by an Exponentially Stretching Surface

By

Maryam Subhani

Department of Mathematics
Quaid-i-Azam University
Islamabad, Pakistan
2020

Boundary Layer Flow of Micropolar Fluid by an Exponentially Stretching Surface

By

Maryam Subhani

Supervised By

Prof. Dr. Sohail Nadeem

Department of Mathematics
Quaid-i-Azam University
Islamabad, Pakistan
2020

Boundary Layer Flow of Micropolar Fluid by an Exponentially Stretching Surface

By

Maryam Subhani

A Dissertation Submitted in the Partial Fulfillment of the requirements for the degree of

DOCTOR OF PHILOSOPHY

IN

MATHEMATICS

Supervised By

Prof. Dr. Sohail Nadeem

Department of Mathematics
Quaid-i-Azam University
Islamabad, Pakistan
2020

Author's Declaration

I, **Maryam Subhani,** hereby state that my PhD thesis titled **Boundary Layer Flow of Micropolar Fluid by an Exponentially Stretching Surface** is my own work and has not been submitted previously by me for taking any degree from the Quaid-i-Azam University Islamabad, Pakistan or anywhere else in the country/world.

At any time, if my statement is found to be incorrect even after my graduation, the university has the right to withdraw my PhD degree.

Name of Student: **Maryam Subhani**

Date: **12th February, 2020**

Plagiarism Undertaking

I solemnly declare that research work presented in the thesis titled "**Boundary Layer Flow of Micropolar Fluid by an Exponentially Stretching Surface**" is solely my research work with no significant contribution from any other person. Small contribution/help wherever taken has been duly acknowledged and that complete thesis has been written by me.

I understand the zero tolerance policy of the HEC and **Quaid-i-Azam University** towards plagiarism. Therefore, I as an Author of the above titled thesis declare that no portion of my thesis has been plagiarized and any material used as reference is properly referred/cited.

I undertake that if I am found guilty of any formal plagiarism in the above titled thesis even afterward of PhD degree, the University reserves the rights to withdraw/revoke my PhD degree and that HEC and the University has the right to publish my name on the HEC/University Website on which names of students are placed who submitted plagiarized thesis.

Student/Author Signature

Name: **Maryam Subhani**

Boundary Layer Flow of Micropolar Fluid by an Exponentially Stretching Surface

By

Maryam Subhani

CERTIFICATE

A THESIS SUBMITTED IN THE PARTIAL FULFILLMENT OF THE REQUIREMENTS FOR THE DEGREE OF THE

DOCTOR OF PHILOSOPHY IN MATHEMATICS

We accept this thesis as conforming to the required standard

1. _____
Prof. Dr. Sohail Nadeem
(Chairman)

2. _____
Prof. Dr. Sohail Nadeem
(Supervisor)

3. _____
Dr. Noreen Sher Akbar
(External Examiner)

Department of Basic Humanities, CE & ME, National University of Science and Technology (NUST), Peshawar Road, Rawalpindi.

4. _____
Dr. Safia Akram
(External Examiner)

Department of Mathematics, Military College of Signals, National University of Science and Technology (NUST), Rawalpindi.

Department of Mathematics
Quaid-I-Azam University
Islamabad, Pakistan
2020

Acknowledgement

"فَبِأَيِّ آلاءِ رَبِّكُمَا تُكَذِّبَانِ"

"So, which of the favors of your Lord would you deny?"

Thanks to Allah Almighty whose innumerable blessings know no bounty. The Omnipotent and the Omniscient has lent His Mercy and made us the ummah of His Prophet ﷺ and enabled us to follow his teachings and seek the light of knowledge to enlighten our mind and soul. Allah, with His Kindness has enabled this humble creature to fulfil this strenuous and fabulous achievement of compiling my day to day untiring research endeavours into this binding which is indeed my own, my parents', my husband's and my mentor's moment of pride.

I extend my heartiest gratitude to my supervisor Prof. Dr. Sohail Nadeem who guided me at every step with his enlightened vision and boosted my morale up whenever I was stuck in and encouraged me in my moments of despair and despondence. I feel highly obliged to him as a guide, a mentor and a facilitator to pave the way for my success.

It is worth mentioning to acknowledge the cooperation of my seniors and fellow students who always lent a hand whenever I was stuck up in an enigmatic situation.

I extend my heartfelt regards to my friends who have been exuberant and energizing to surge up my morale and provided the friendly and supportive environment to conduct the research.

I am grateful to my mother, my father, my husband and my sister whose support and encouragement granted me a fitting crowning touch for accomplishment of this dissertation. I specially thank my mother who was a torch bearer for me in this journey of the pursuit of knowledge.

Dedicated

to my

Beloved

Parents

Table of Contents

List of Figures

List of Tables

Nomenclature

Dimensional	
ODE	Ordinary Differential Equations
PDE	Partial Differential Equations
t	Time coordinate
x, y, z	Spatial coordinates
$\boldsymbol{V}$	Velocity field
$\boldsymbol{N}$	Micro-rotation field
u, v, w	Components of velocity in x, y, z directions
u_p, v_p, w_p	Components of velocity of dust particles in x, y, z directions
N_1, N_2, N_3	Micro-rotation components in x, y, z directions respectively
T	Temperature field
T_p	Temperature field of dust particles
C	Concentration profile
C_p	Concentration profile of dust particles
U_0, V_0, T_0	Constants
U_w	Velocity at surface along *x-axis*
V_w	Velocity at surface along *y-axis*
T_w	Temperature of the surface
T_∞	Ambient fluid temperature
C_w	Concentration along surface
C_∞	Ambient fluid concentration
L	Reference length
b_1	Temperature exponent
c_1	Concentration exponent
k	Vortex viscosity
n	Boundary parameter

ρ_{hnf}	Density of hybrid nanofluid
ρ_{nf}	Density of nanofluid
ρ_f	Density of base fluids
ρ_s	Density of solid fraction
μ_{hnf}	Dynamic viscosity of hybrid nanofluid
μ_{nf}	Dynamic viscosity of nanofluid
μ_f	Dynamic viscosity of base fluids
μ_s	Dynamic viscosity of solid fraction
ν_{hnf}	Kinematic viscosity of hybrid nanofluid
ν_{nf}	Kinematic viscosity of nanofluid
ν_f	Kinematic viscosity of base fluids
ν_s	Kinematic viscosity of solid fraction
ν	Kinematic viscosity
k_{hnf}	Thermal conductivity of hybrid nanofluid
k_{nf}	Thermal conductivity of nanofluid
k_f	Thermal conductivity of base fluids
k_s	Thermal conductivity of solid fraction
k^*	Mean absorption coefficient
$(\rho C_p)_{hnf}$	Heat capacity of hybrid nanofluid
$(\rho C_p)_{nf}$	Heat capacity of nanofluid
$(\rho C_p)_f$	Heat capacity of base fluids
$(\rho C_p)_s$	Heat capacity of solid fraction
α_{hnf}	Thermal diffusivity of hybrid nanofluid
α_{nf}	Thermal diffusivity of nanofluid
α_f	Thermal diffusivity of base fluid
α_s	Thermal diffusivity of solid fraction
σ_{hnf}	Electrical conductivity of hybrid nanofluid

σ_f	Electrical conductivity of base fluids
σ	Electrical conductivity
σ^*	Stefan-Boltzmann constant
χ_{hnf}	Spin gradient viscosity of hybrid nanofluid
χ_{nf}	Spin gradient viscosity of nanofluid
χ	Spin gradient viscosity of fluid
ϕ_1, ϕ_2	Nanoparticle volume fraction
j	Micro-inertia per unit mass
α	Positive constant
Ω	Angular velocity of fluid
Ω_0	Reference angular velocity
K^*	Permeability of porous media
B_0	Strength of magnetic field
K	Stoke's resistance
N^*	Number density of dust particles
S	Suction parameter
m	Mass of dust particles
c_p	Specific heat capacity of fluid
c_m	Specific heat capacity of dust particles
Q	Heat source
q_r	Radiative heat flux
D_B	Brownian diffusion coefficient
D_T	Thermophoresis coefficient
D	Coefficient of mass diffusivity
τ_v	Relaxation time of dust phase
τ_T	Thermal equilibrium time
C_{fx}, C_{fy}	Local skin friction coefficients

Nu_x	Local Nusselt number
Sh_x	Sherwood number
τ_{wx}, τ_{wy}	Surface shear stresses
q_w	Surface heat flux
q_m	Surface mass flux
Cu	Copper nanoparticles
TiO_2	Titanium Oxide nanoparticles
Al_2O_3	Aluminium Oxide nanoparticles
η	Dimensionless parameter
$f'(\eta), g'(\eta)$	Dimensionless velocity profiles
$h_1(\eta), h_2(\eta)$	Dimensionless micro-rotation components
$F'(\eta)$	Dimensionless velocity of dust particle phase
$\theta(\eta)$	Dimensionless temperature profile
$\theta_p(\eta)$	Dimensionless temperature profile of dust particles
$\phi(\eta)$	Dimensionless concentration profile
$\phi_p(\eta)$	Dimensionless concentration profile of dust particles
R_1	Vortex viscosity parameter
R_2	Spin gradient viscosity parameter
R_3	Micro-inertia density parameter
K_p	Porosity parameter
λ	Stretching ratio parameter
$A_1(\phi)$	Effective dynamic viscosity of nanofluid
$A_2(\phi)$	Effective dynamic viscosity of hybrid nanofluid
A	Unsteadiness parameter
M	Magnetic parameter
ε	Rotation parameter
Pr	Prandtl number
l	Mass concentration

γ	Ratio of specific heat capacity
β	Fluid particle interaction parameter for velocity
β_T	Fluid particle interaction parameter for heat transfer
Ec	Eckert number
R	Radiation parameter
λ^*	Heat source/sink parameter
Nt	Thermophoresis parameter
Nb	Brownian motion parameter
Sc	Schmidt number
Re_x	Local Reynold's number
Sc	Brinkman number
δ	Dimensionless temperature difference

Chapter 1

1. Introduction

In the contemporary period, new substances are incorporated in the industrial processes which cannot be characterized as Newtonian fluids such as colloids, surfactant solution, liquid crystals, etc. Consequentially, several non-Newtonian fluids have been put forward. Among these occur certain rheologically complex fluids, that is fluids consisting of particles with microstructure, which have conspicuous utilization in chemical, pharmaceutical, engineering and food industries. The discrete particles of the aforementioned fluids may vary in shape, may have the ability to shrink or expand and above all they might rotate on their own not depending upon the movement and rotation of the fluid. So, the flow properties of these fluids cannot be adequately described by Navier-Stokes equations alone, due to their diversified structure. Hence it was the need of the hour to formulate a theory considering deformation, geometry, local structure and intrinsic motion of the individual particles. Therefore, Eringen [1-2] propounded the hypothesis of micropolar fluids, which gives an accurate model for such fluids by including the micro-rotational momentum equation besides the classical momentum equation. This new equation is based on the principle of conservation of angular momentum by introducing a new vector field (the micro-rotation) also involving spin vector and micro-inertia tensor besides the velocity vector giving the total angular velocity of rotating particles. Micropolar fluids physically characterize fluids that comprise rigid, arbitrarily aligned spherical particles dispersed within a viscid medium exhibiting intrinsic rotational micro-motions. Due to its diverse applications in various industries such as pharmaceutical, food, chemical and

technological processes, the micropolar fluid phenomenon is more significant and realistic. Applications of micropolar fluids include colloidal solutions, complex fluids containing additives like crystals, fluids with fibrous structures, muddy fluids, particle suspensions, exotic lubricants as well as there exist some biological fluids which model micropolar fluid such as animal blood. Several analytical and experimental attempts have been conducted to examine the flow behavior of micropolar nanofluid under various circumstances, geometries and attributes. After the initial manifestation of the concept of micropolar fluid, a detailed overview of the phenomenon was given by Lukaszewicz [3] and Eringen [4] in their books. Chaim [5] discussed solution for micropolar fluid flow past a stretching surface. Then the heat transfer analysis of micropolar fluid by a stretching sheet was performed numerically by Hassanien et al. [6]. The influence of uniform suction/blowing through the stretching surface on the boundary layer flow of micropolar fluid was probed by Kelson et al. [7]. The impact of variable thermal conductivity, magnetic field as well as radiation over the flow and heat transfer characteristics of micropolar fluid past a stretched surface was studied by Mahmoud [8]. Mohanty et al. [9] investigated the properties related to the transfer of heat and mass of micropolar fluid past a stretching sheet embedded within a porous medium along with viscous dissipation effects. The conduct of micropolar nanofluid over stretching sheet considering various compatible models which comprise different nanoparticles and base fluids was probed by Hussain et al. [10]. Chamkha et al. [11] explored the flow regime in three-dimensions of micropolar fluid. Ahmad et al. [12] scrutinized the flow behavior of unsteady three-dimensional micropolar fluid over a stretching sheet under boundary layer approximation. A comparative analysis between optimal and numerical solutions of MHD flow of micropolar nanofluid across a porous channel, also considering radiation effects was performed by Mohyud-din et al. [13]. Later, Abd El-Aziz [14]

explored the flow behavior of micropolar fluid by an exponentially stretched sheet considering viscous dissipation effects. Shelukhin et al. [15] discussed the thermodynamic properties of Bingham fluids under micropolar theory.

Common heat transport fluids particularly water, several mineral oils as well as ethylene glycol possess weak thermal conductivity, which is a great hindrance in the progression of thermal systems. To overcome this barrier, abundant research has been allocated to make the thermal transport characteristics of these fluids better. Introducing nano-meter sized metallic solid particles in the base fluid was a cutting-edge solution brought forward by Choi [16], which proved to be a breakthrough in technological and industrial advancement. Nanoparticles boost the thermal conductivity of traditional fluids resulting in improved heat transfer properties. Therefore, nanofluids are characterized as a homogeneous solid-fluid mixture with base fluid of low conductivity and nano-meter sized particles with high thermal conductivity. So, owing to the higher thermal conductivity of consequential nanofluids, they lower the pumping cost of heat exchangers to a greater extent. Nanoparticles characterized by their little fractional volume, stable condition and remarkable myriad applications in multifarious fields such as biomedical, optical and electronic fields have paved the way for new lines of research. A thorough investigation of nanofluid's convective transport was executed by Buongiorno [17]. In the present era many researchers have laid their hands on the latest phenomena of nanoparticles different cadres with relevant physical characteristics of fluids, see references [18-26]. Additionally, an innumerable amount of theoretical and experimental literature can be found on the properties, synthetization and conduct of nanofluids in various mediums [27-28]. Since nanoparticles are minute in size, they can haul with them slip velocity through the base fluid molecules (see Buongiorno [17]). Particle rotation is also an essential aspect in heat transfer

enhancement which was observed by Ahuja [29]. Keeping in view that nanoparticles can schlep slip velocity with base fluid molecules, the likelihood of translation and micro-rotation arises. The micropolar theory considers the effects of micro-rotation hence implementation of this hypothesis in case of nanoparticles yields a valuable comprehension to the prodigious rise in nanofluid's thermal conductivity. Subsequently, research conducted over micropolar nanofluid gained momentum and [30-31] analyzed the impact of different attributes over the micropolar nanofluids.

Nanofluids play a vital role in heat exchange systems because of their promising attributes which can be modified in accordance with the requirements. To upgrade the features of conventional nanofluids regarding heat transfer scientists have designed a new genre of fluid termed as hybrid nanofluid. It has been streamlined as a new class of nanofluids, marked by its thermal properties and potential utilities which serve the purpose to upgrade the level of heat transfer. By dispersion of two or more dissimilar nanoparticles in a base fluid, hybrid nanofluids are formulated which have higher thermal conductivity relative to mono nanofluids by virtue of the synergistic effect. Hybrid nanofluids show great enhancement in thermal and rheological properties as compared to mono nanofluids (fluids with only one kind of nanoparticles) as a consequence of augmented thermal conductivity. The quantities of nanoparticle volume fraction can be varied to acquire the desired heat flow rate. Hybrid nanofluids have optimum utility in heat transport fields such as micro fluidics, transportation, defense, acoustics, medical, naval structures etc. A lot of theoretical plus experimental data is available discussing the behavior of hybrid nanofluid in different flow regimes. Madhesh et al. [30] carried out a profound experiment upon the characteristics and convective heat flow properties of $Cu - TiO_2/water$ hybrid nanofluid. Esfe et al. [31] experimentally verified thermal conductivity plus other

physical properties of $Silver - Magnesium\ Oxide/water$ hybrid nanofluid. Suresh et al. [32] inspected the influence of $Aluminum\ Oxide - Cu/water$ hybrid nanofluid on heat transfer rate. Numerical analysis for flow behavior of hybrid nanofluid has been carried out by [33-37].

Fluid particle suspension due to its multiple applications and bountiful utility in the fields of geophysics, engineering and medical science has gained utmost importance. Fluid particle suspension or dusty fluid deals with the combination of liquid/gas and inert, immiscible solid particles such as dust in gas cooling systems. Their immense application is traced in cement process and steel manufacturing industry, fluidized bed, magneto hydrodynamic generators (MHG), gas purification, sedimentation pipe flows and bio fluids. The foremost task of deriving the equations for the dusty fluid flow was undertaken by Saffman [38] who also gave the stability analysis for laminar flowing fluid with uniformly distributed dust particles. Vajravelu et al. [39] conducted investigation on hydro-magnetic flow of a dusty fluid and highlighted the outcome of fluid particle collisions and suction on fluid properties. Extensive research has been done on fluid with dust particles by Gireesha et al. [40-41], on various aspects such as for nanofluids, convective surface conditions, unsteady flow upon a stretching sheet, and MHD flow in conjunction with heat transfer analysis.

Magnetohydrodynamics is a branch of mathematics and physics that brings to light the dynamics of magnetic field in fluids which are electrical conductors. The fundamental principle behind magnetohydrodynamics theory is that conductive fluids can also be acted upon by magnetic fields. MHD studies have been carried out for several astrophysical and geophysical problems. Nowadays MHD has several applications appearing in engineering, metallurgical, medical and petroleum industries as well due to which it has gained attention of researchers. MHD is of vital importance especially in metallurgical procedures for example, the process of

cooling of filaments and strips being pulled out from an inert fluid and exclusion of non-metallic materials from molten metals. The filaments are being drawn through an electric conductor fluid exposed to magnetic field; this helps in controlling the cooling rate. Magnetohydrodynamics also has its applications in the process of cooling of nuclear reactors, power generators, in the pattern of heat exchanges, MHD accelerators and electrostatic filters. So, these fluid flows were analyzed by numerous researchers amongst which some prominent work was done by Andersson [42] in 1992, after that by Al-Odat et al. [43] in 2006 and later by Ishak [44] in 2011. Currently research is being sought on MHD flows over exponentially stretching sheets [45-46].

It is worth mentioning that unsteady flow conditions are encountered in case when flow turns out to be time dependent because of unusual change in temperature or stretching of surface or heat flux at the surface. In literature there are many investigations regarding the steady flow of micropolar fluid. However, relatively fewer studies exist dealing the unsteady flow of micropolar fluid caused by an exponentially stretching surface. Ibrahim et al. [47] investigated the influence of unsteady mixed convection flow of micropolar fluid. Elbashbeshy [48] discussed the thermal radiation plus magnetic field impact upon unsteady flow. Quiet recently some researchers [49-51] have performed a qualitative research over unsteady flows involving various geometries.

Entropy is termed as the amount of disorder in a thermodynamically closed framework it is the measure of the number of distinct processes for the setting of a system. Entropy has pivotal role in explaining several diverse phenomena varying from cosmology to biology. The utility of entropy generation has become a focal point in the study of heat transfer process. In recent times, scientists emphasized towards effectiveness of entropy generation during the process of heat transfer. This concept has marginal utility in numerous processes of heat transfer

convection. A close study of this concept facilitates us to evaluate the irreversibility's due to viscous dissipation plus heat transport. The heat transfer pace and friction lost in the system [52, 53] are discriminated by the entropy generation in a particular framework. Nanoparticle's magneto hydrodynamic flow by convection process through permeable surface with entropy generation was inspected by Chu and Liu [54], they applied Finite Difference Method (FDM). Process of irreversibility considering viscous dissipation, joule heating and thermal radiation is assessed by the rate of total entropy generation. Dalir et al. [55] probed flow of visco-elastic nanofluid accompanied by entropy generation through a stretching medium. Flow problem was resolved by implicit numerical based algorithm named Keller's box technique. Rate of irreversibility proportion and entropy generation depending upon volume were examined. Analysis divulges that Lewis, Reynolds, Prandtl number and thermophoresis parameter controls the rate of entropy generation. Refs. [56–61] mentions the modern improvement on entropy generation.

Since the past few decades, many researchers are inquiring the features of flow besides the heat transport inside porous medium owing to its incessantly growing industrial and technological applications. Problems associated with porous surfaces incorporate insulation engineering, geo-mechanics such as geo thermal reservoirs and enhanced oil recovery. Main use of porous medium is to shield a heated body so that its temperature can be maintained. Porous media are also thought to be beneficial in vanishing the naturally caused free convection otherwise which would affect the stretching surface immensely. Kamel et al. [62] and Heruska [63] have examined the micropolar fluid's flow across a porous medium. MHD 3D flow of Casson fluid by a porous stretching surface was evaluated by Nadeem et al. [64]. Very recently

a number of studies [65-67] have explored the behavior of micropolar fluid induced by a stretching porous sheet.

Keeping all these factors in mind the present thesis consists of following six chapters in which chapter one is devoted to the introduction section while other are stated below.

In the second chapter we have studied the numerical examination of 3D micropolar nanofluid prompted due to exponential rate of stretching of surface placed inside a porous medium. The complicated coupled scheme of differential equations is modified into non-dimensional form via apt similarity transformations. Solution of consequential equations is derived by using bvp-4c technique. The outcomes are observed through tables and graphs. European Physical Journal Plus has included the subject matter of this chapter in its journal.

In the third chapter, 3D flow of micropolar hybrid nanofluid with rotation and porous medium has been analyzed numerically. We considered water based hybrid nanofluid with $Cu - TiO_2$ nanoparticles. The computational outcomes are acquired by means of bvp-4c built in MATLAB programme. A comparison of nanofluid and hybrid nanofluid has been presented. A graphic representation of the consequence of physical parameters on the flow has been provided and discussed quantitatively. Owing to its due importance this chapter has found room for publication in Applied Nanoscience.

Fourth chapter examines the unsteady magneto-hydrodynamic flow of a micropolar fluid with hybrid nanoparticles via porous medium. A relative study is executed for copper Cu and $Cu - TiO_2/water$ nanoparticles while supposing water as its base fluid. Transformed coupled system of governing equations is solved numerically. The obtained results are compared with

the existing literature. An exemplary conformity has been traced leading to the validity of the current analysis. Physica Scripta has honoured this chapter as its publication.

In fifth chapter, entropy generation in micropolar hybrid nanofluid has been investigated. Viscous degeneracy effects have also been considered. By utilizing second law of thermodynamics entropy generation analysis is conducted. It also examines the effects of micropolar hybrid nanofluid on dimensionless physical quantities and entropy generation. Net T entropy generation rate is brought into consideration for various involved variables. The problem is resolved computationally through bvp-4c technique. The subject matter of this section has been extended for publication to International Journal of Heat and Mass Transfer.

Sixth chapter investigates the 2D unsteady heat and mass transfer analysis of MHD micropolar dusty nanofluid flow. The nanofluid model considered here is Buoungiorno model. Considering the impact of heat generation/absorption, viscous degeneracy and thermal radiation, PDE's are modelled. Then they are changed to ODE's by employing similarity transformations for two cases of boundary conditions and then the analytical solution is found using Optimal Homotopy Analysis Method. In the end, the influence on the velocity, temperature and concentration profiles of various important physical parameters are explored in detail with graphical illustrations and tables. The findings of this segment are forwarded in Journal of Molecular Liquids.

Chapter 2

2. Numerical study of micropolar nanofluid due to an exponentially stretching surface in a porous medium

2.1 Introduction

Present chapter addresses the flow of a three-dimensional micropolar nanofluid caused by an exponentially stretched surface confined within a porous medium. Mathematical model is elaborated with the help of PDE's by executing boundary layer methodology. After that by engaging similarity transformations, modeled PDE's are transmuted to ODE's. Solution of these ODE's is acquired by means of bvp-4c method. The graphical representations are put up to understand the prominent features of physical parameters on concerning profiles for several sorts of nanoparticles such as Copper, Titania and Alumina with base fluid being water. For better interpretation of flow regime variations in skin friction coefficients and Nusselt number are scrutinized through tables. We perceive from the present study that omission of porous matrix enhances the flow of the fluid and the occurrence of nanoparticles aggravates the degree of heat transfer.

2.2 Momentum and Temperature Description

We have considered steady 3D incompressible flow of micropolar nanofluid due to an exponentially stretching surface embedded in a porous medium. It is supposed that the surface is being stretched in two adjacent directions with different velocities, U_w which is along x-axis and V_w is along y-axis. The surface is located at the plane $z = 0$ and the flow is kept in the region $z > 0$ (see ***Fig. 2.1***). The transport equations are mentioned below

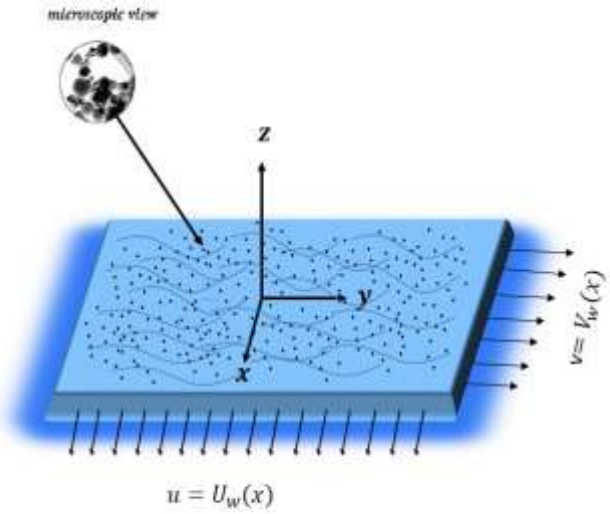

Fig. 2.1. Physical regime of the problem

$$\nabla . \vec{V} = 0, \tag{2.1}$$

$$\rho_{nf}\left((\vec{V}.\nabla)\vec{V}\right) = -\nabla p + (\mu_{nf} + k)\nabla^2\vec{V} + k(\nabla \times \vec{N}) - \frac{\nu_{nf}\vec{V}}{K^*}, \tag{2.2}$$

$$\rho_{nf}\, j\left((\vec{V}.\nabla)\vec{N}\right) = \chi_{nf}\nabla^2\vec{N} - 2k\vec{N} + k(\nabla \times \vec{V}), \tag{2.3}$$

$$\left((\vec{V}.\nabla)\vec{T}\right) = \alpha_{nf}\nabla^2\vec{T}. \tag{2.4}$$

Where,

$$\left.\begin{aligned}
&\vec{V} = [u(x,y,z),\ v(x,y,z),\ w(x,y,z)],\\
&\vec{N} = [N_1(x,y,z),\ N_2(x,y,z),\ N_3(x,y,z)],\\
&\vec{T} = T(x,y,z),\\
&\alpha_{nf} = \frac{k_{nf}}{(\rho c_p)_{nf}},\ \mu_{nf} = \frac{\mu_f}{(1-\phi_1)^{2.5}},\ \rho_{nf} = (1-\phi_1)\rho_f + \phi_1\rho_s,\\
&\left(\rho C_p\right)_{nf} = (1-\phi_1)\left(\rho C_p\right)_f + \phi_1\left(\rho C_p\right)_s,\\
&k_{nf} = \frac{\left(k_s + 2k_f\right) - 2\phi_1\left(k_f - k_s\right)}{\left(k_s + 2k_f\right) + \phi_1\left(k_f - k_s\right)},\ \nu_{nf} = \frac{\mu_{nf}}{\rho_{nf}},\\
&\chi_{nf} = (\mu_{nf} + k/2)\, j.
\end{aligned}\right\} \tag{2.5}$$

After implementing boundary layer approximations, we attain following equations

$$\left[\frac{\partial u}{\partial x} + \frac{\partial v}{\partial y} + \frac{\partial w}{\partial z}\right] = 0, \tag{2.6}$$

$$\left[u\frac{\partial u}{\partial x} + v\frac{\partial u}{\partial y} + w\frac{\partial u}{\partial z}\right] = \left(\frac{\mu_{nf} + k}{\rho_{nf}}\right)\frac{\partial^2 u}{\partial z^2} - \frac{k}{\rho_{nf}}\left(\frac{\partial N_2}{\partial z}\right) - \frac{\nu_{nf}u}{K^*}, \tag{2.7}$$

$$\left[u\frac{\partial v}{\partial x} + v\frac{\partial v}{\partial y} + w\frac{\partial v}{\partial z}\right] = \left(\frac{\mu_{nf} + k}{\rho_{nf}}\right)\frac{\partial^2 v}{\partial z^2} + \frac{k}{\rho_{nf}}\left(\frac{\partial N_1}{\partial z}\right) - \frac{\nu_{nf}v}{K^*}, \tag{2.8}$$

$$\rho_{nf}\, j\left[u\frac{\partial N_1}{\partial x} + v\frac{\partial N_1}{\partial y} + w\frac{\partial N_1}{\partial z}\right] = \chi_{nf}\frac{\partial^2 N_1}{\partial z^2} - 2kN_1 - k\frac{\partial v}{\partial z}, \tag{2.9}$$

$$\rho_{nf} j\left[u\frac{\partial N_2}{\partial x}+v\frac{\partial N_2}{\partial y}+w\frac{\partial N_2}{\partial z}\right]=\chi_{nf}\frac{\partial^2 N_2}{\partial z^2}-2kN_2+k\frac{\partial u}{\partial z}. \tag{2.10}$$

$$u\frac{\partial T}{\partial x}+v\frac{\partial T}{\partial y}+w\frac{\partial T}{\partial z}=\alpha_{nf}\left(\frac{\partial^2 T}{\partial z^2}\right). \tag{2.11}$$

Boundary Conditions

$$\left.\begin{aligned} &u=U_w,\ v=V_w,\ T=T_w,\ N_1=n\frac{\partial v}{\partial z},\ N_2=-n\frac{\partial u}{\partial z},\ \text{at z}=0,\\ &u\to 0,\ v\to 0,\ T\to T_\infty,\ N_1\to 0,\ N_2\to 0,\qquad \text{as z}\to\infty. \end{aligned}\right\} \tag{2.12}$$

Here n signifies the boundary parameter, n ranges from $0\le n\le 1$. Here $n=0$ signifies strong concentration of microelements at wall and in this case the microelements at the stretching surface are incapable of rotation. When $n=0.5$ it exhibits weak concentration of microelements and $n=1$ symbolizes the turbulent boundary layer flows.

The stretching velocities at surface and temperature at the wall are described as follows:

$$U_w=U_0e^{\frac{x+y}{L}},\ V_w=V_0e^{\frac{x+y}{L}},\ T_w=T_\infty+T_0e^{\frac{b_1(x+y)}{2L}}. \tag{2.13}$$

Appropriate similarity transformations utilized are given below:

$$\left.\begin{aligned} &u=U_0e^{\frac{x+y}{L}}f'(\eta),\ v=U_0e^{\frac{x+y}{L}}g'(\eta),\ w=-\left(\frac{\nu U_0}{2L}\right)^{\frac{1}{2}}e^{\frac{x+y}{2L}}\{f+\eta f'+g+\eta g'\},\\ &N_1=\frac{U_0}{2\nu L}\left(U_0 2\nu L\right)^{\frac{1}{2}}e^{3\left(\frac{x+y}{2L}\right)}h_1(\eta),\ N_2=\frac{U_0}{2\nu L}\left(U_0 2\nu L\right)^{\frac{1}{2}}e^{3\left(\frac{x+y}{2L}\right)}h_2(\eta),\\ &T=T_\infty+T_0e^{\frac{B(x+y)}{2L}}\theta(\eta),\ \eta=\left(\frac{U_0}{2\nu L}\right)^{\frac{1}{2}}e^{\frac{x+y}{2L}}z. \end{aligned}\right\} \tag{2.14}$$

After applying these transformations on eqs. (2.6-2.11), continuity equation satisfies identically while linear momentum, angular momentum and energy equations are transformed as

$$\frac{\rho_f}{\rho_{nf}}\left(A_1(\phi)+R_1\right)f'''+f''(f+g)-2f'(f'+g')-\frac{\rho_f}{\rho_{nf}}R_1h_2'-\frac{\nu_{nf}}{\nu_f}K_p f'=0, \tag{2.15}$$

$$\frac{\rho_f}{\rho_{nf}}\left(A_1(\phi)+R_1\right)g'''+g''(f+g)-2g'(f'+g')+\frac{\rho_f}{\rho_{nf}}R_1h_1'-\frac{\nu_{nf}}{\nu_f}K_p g'=0, \tag{2.16}$$

$$\frac{\rho_f}{\rho_{nf}}R_2h_1''-R_1R_3(2h_1+g'')-3h_1(f'+g')+h_1'(f+g)=0, \tag{2.17}$$

$$\frac{\rho_f}{\rho_{nf}}R_2h_2''-R_1R_3(2h_2-f'')-3h_2(f'+g')+h_2'(f+g)=0, \tag{2.18}$$

$$\frac{1}{\mathrm{Pr}}\frac{\left(k_{nf}/k_f\right)\theta''}{(1-\phi_1)+\left(\phi_1(\rho c_p)_s/(\rho c_p)_f\right)}-b_1(f'+g')\theta+(f+g)\theta'=0. \tag{2.19}$$

And associated boundary conditions become:

$$\left.\begin{aligned} &f(0)=0,\ f'(0)=1,\\ &g(0)=0,\ g'(0)=\lambda,\ \theta(0)=0,\\ &h_1(0)=ng''(0),\ h_2(0)=-nf''(0), \quad as\ \eta\to 0,\\ &f'\to 0,\ g'\to 0,\ \theta\to 0,\\ &h_1\to 0,\ h_2\to 0, \qquad as\ \eta\to\infty. \end{aligned}\right\} \tag{2.20}$$

Where

$$\left.\begin{aligned} \mathrm{R}_1 = \frac{k}{\mu},\ \mathrm{R}_2 = \frac{\chi_{nf}}{\mu j},\ \mathrm{R}_3 = \frac{2\nu L}{jU_w},\ K_p = \frac{2\nu L}{K^* U_w},\ \mathrm{Pr} = \frac{(\mu C_p)_f}{k_f},\ \lambda = \frac{V_0}{U_0}, \\ and\ \ A_1(\phi) = \frac{\mu_{nf}}{\mu_f} = \frac{1}{(1-\phi_1)^{2.5}}. \end{aligned}\right\} \tag{2.21}$$

The skin friction co-efficients and the Nusselt number can be described as:

$$C_{fx} = \frac{\tau_{wx}}{\frac{1}{2}\rho_{nf} U_w^2},\ C_{fy} = \frac{\tau_{wy}}{\frac{1}{2}\rho_{nf} U_w^2},\ Nu_x = \frac{x q_w}{k_f (T_w - T_\infty)}, \tag{2.22}$$

where, τ_{wx}, τ_{wy} and q_w are surface shear stress and surface heat flux, which can be defined as:

$$\left.\begin{aligned} \tau_{wx} &= (\mu_{nf} + k)\left(\frac{\partial u}{\partial z}\right)_{z=0} + k(N_2)_{z=0}, \\ \tau_{wy} &= (\mu_{nf} + k)\left(\frac{\partial v}{\partial z}\right)_{z=0} + k(N_1)_{z=0}, \\ q_w &= -k_{nf}\left(\frac{\partial T}{\partial z}\right)_{z=0}. \end{aligned}\right\} \tag{2.23}$$

After simplification, the non-dimensional form of skin friction coefficients and local Nusselt number are:

$$\left.\begin{aligned} \frac{1}{\sqrt{2}} C_{fx} (\mathrm{Re})^{\frac{1}{2}} &= \left(\frac{A_1(\phi) + (1-n)R_1}{(1-\phi_1) + \phi_1(\rho_s/\rho_f)}\right) f''(0), \\ \frac{1}{\sqrt{2}} C_{fy} (\mathrm{Re})^{\frac{1}{2}} &= \left(\frac{A_1(\phi) + (1+n)R_1}{(1-\phi_1) + \phi_1(\rho_s/\rho_f)}\right) g''(0), \\ \sqrt{2}\,\frac{L}{x} Nu_x\, \mathrm{Re}^{\frac{1}{2}} &= -\frac{k_{nf}}{k_f}\theta'(0). \end{aligned}\right\} \tag{2.24}$$

2.3 Numerical Schemes

The non-linear coupled equations (2.15-2.19) together with their boundary conditions given in equation (2.20) are solved numerically using bvp-4c technique invoking shooting methodology. The built-in MATLAB program bvp-4c contains finite difference method that executes the Lobatto IIIa formula with 3 stages. This applied algorithm is based on the collocation method and we obtain a scheme of non-linear algebraic equations and the collocation conditions are levied on all subintervals. In this process, firstly the system of equations (2.15-2.19) and boundary conditions are transformed to first order differential equations. Then appropriate initial guesses are adopted which satisfy the boundary conditions. For further details of this procedure see reference [71]. The results acquired portray the behavior of velocity, micro-rotation and temperature profiles in accordance with variations of certain considered factors.

2.4 Results and Discussion

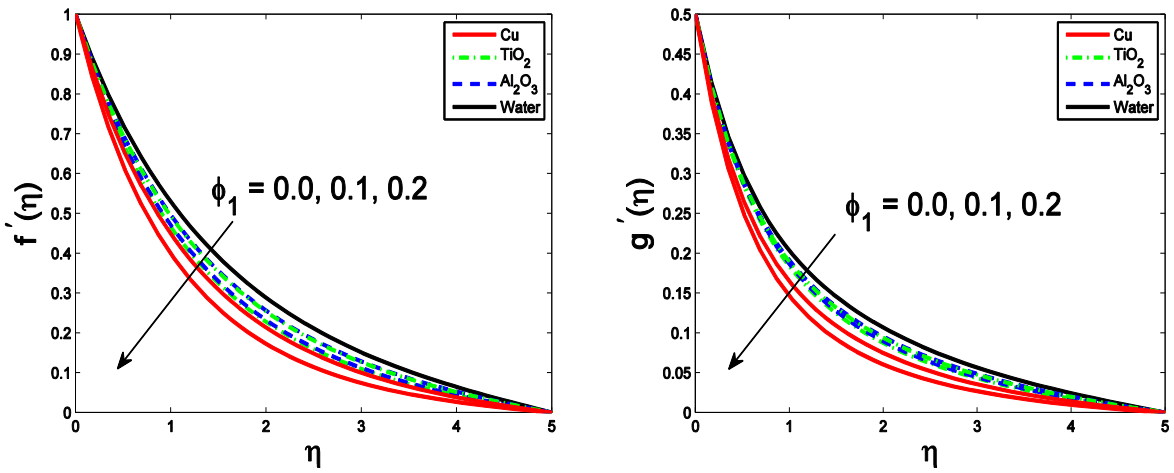

Fig. 2.2. Impact of ϕ_1 on velocity in **(a)** x-direction $f'(\eta)$ and **(b)** y-direction $g'(\eta)$.

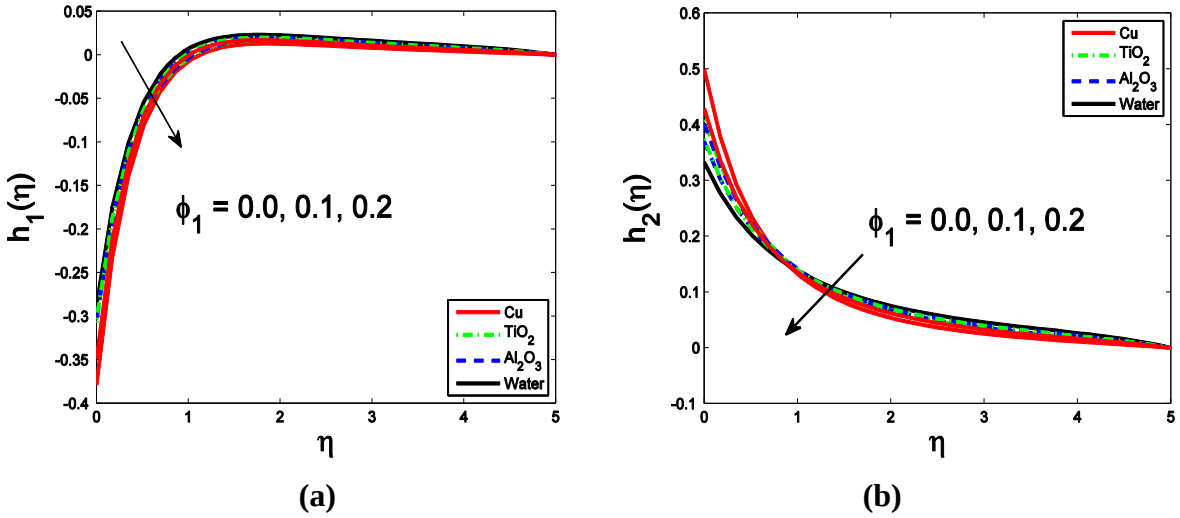

Fig. 2.3. Variation of ϕ_1 on components of micro-rotation **(a)** $h_1(\eta)$ and **(b)** $h_2(\eta)$.

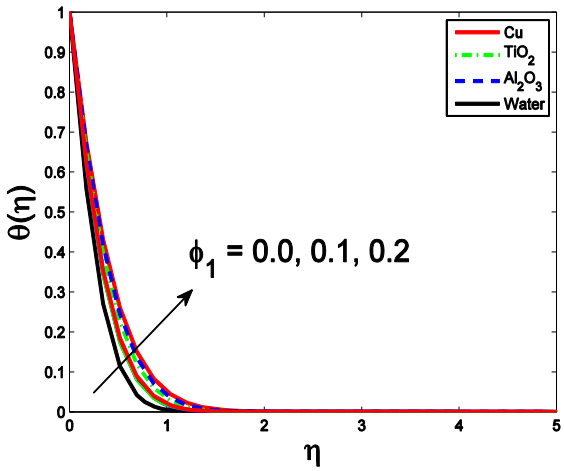

Fig. 2.4. Variation of various nanoparticle volume fractions on temperature distribution $\theta(\eta)$.

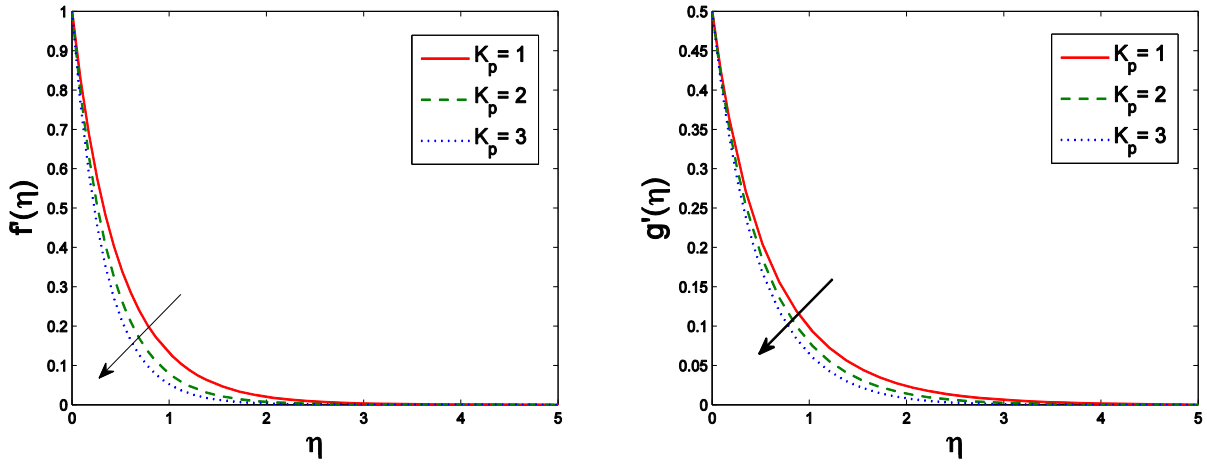

(a) **(b)**

Fig. 2.5. Influence of porosity parameter on velocity profile in **(a)** x-direction $f'(\eta)$ and **(b)** y-direction $g'(\eta)$.

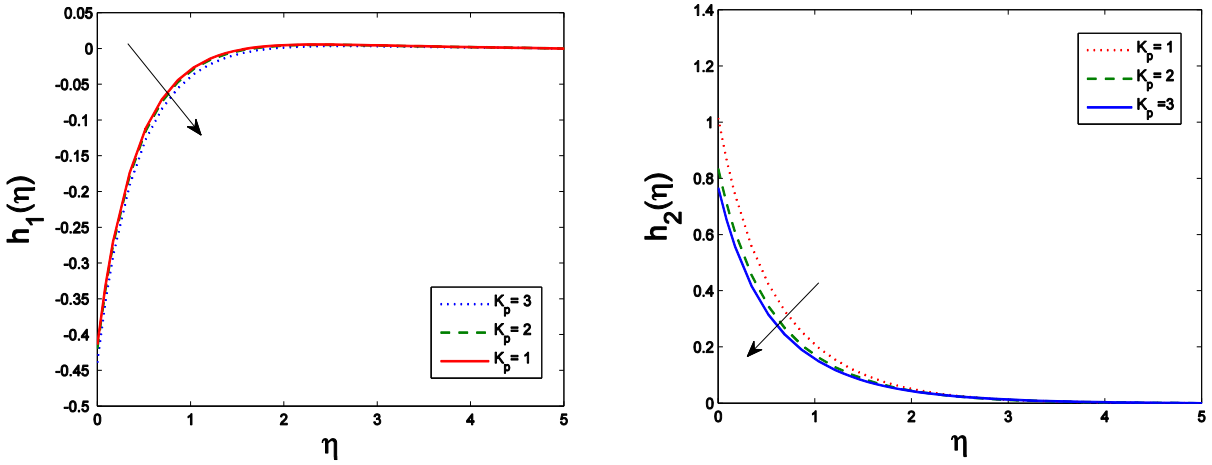

(a) **(b)**

Fig. 2.6. Influence of K_p on micro-rotation components **(a)** $h_1(\eta)$ and **(b)** $h_2(\eta)$.

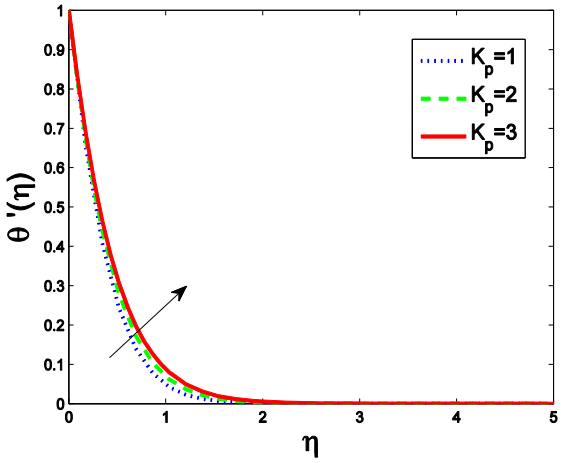

Fig. 2.7. Outcomes in temperature profile due to changes in porosity parameter.

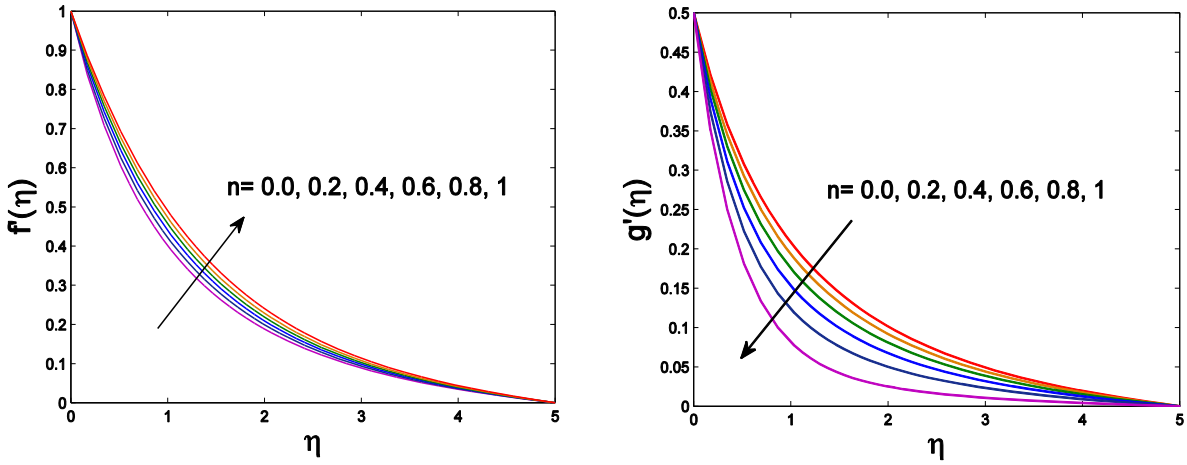

(a) **(b)**

Fig. 2.8. Impact of n on velocity profile in **(a)** x-direction and **(b)** y-direction.

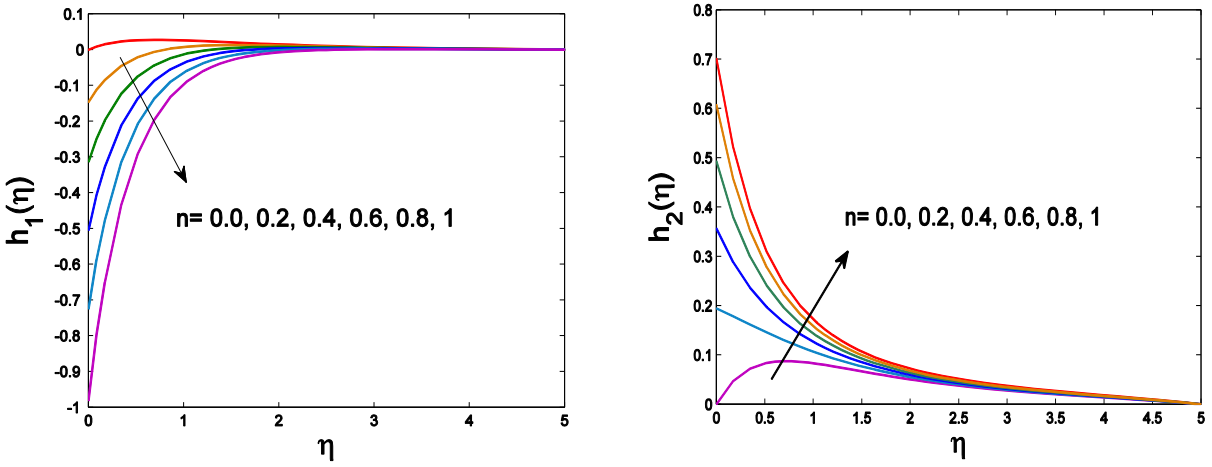

(a) **(b)**

Fig. 2.9. Impact of n on micro-rotation components **(a)** $h_1(\eta)$ and **(b)** $h_2(\eta)$

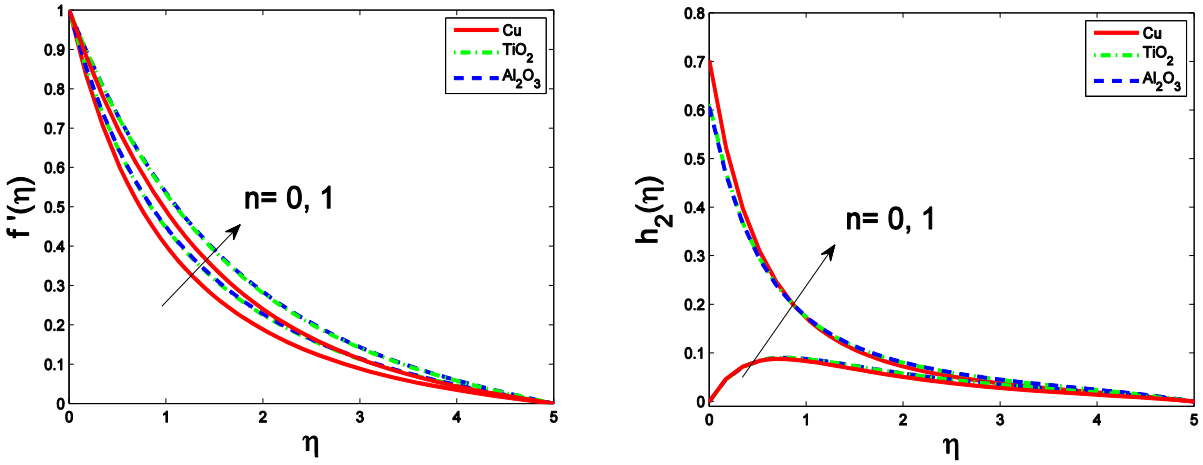

(a) **(b)**

Fig. 2.10. Behavior of different nanoparticles w.r.t n on **(a)** velocity profile in x-direction **(b)** micro-rotation $h_2(\eta)$.

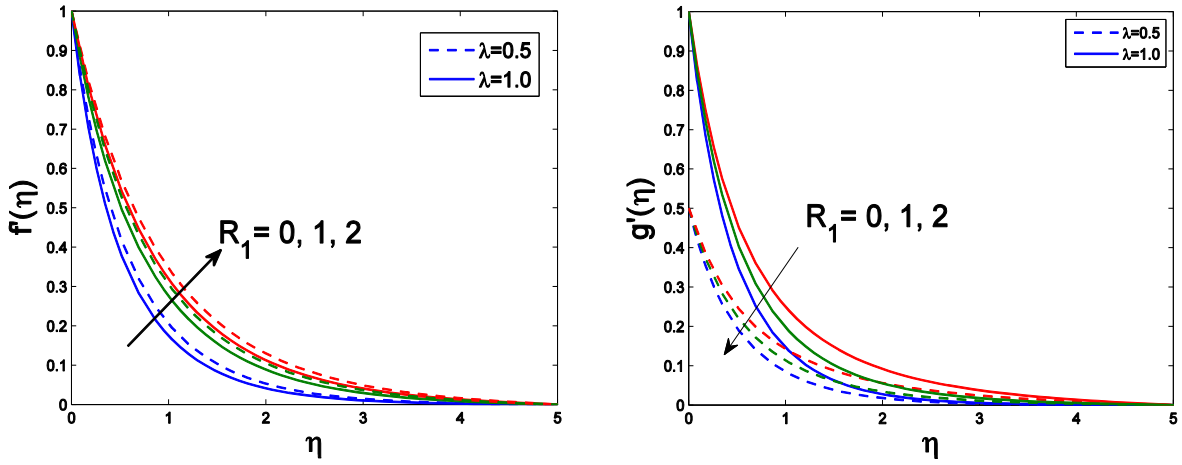

(a) **(b)**

Fig. 2.11. Influence of R_1 upon velocity profile in **(a)** x-direction and **(b)** y-direction.

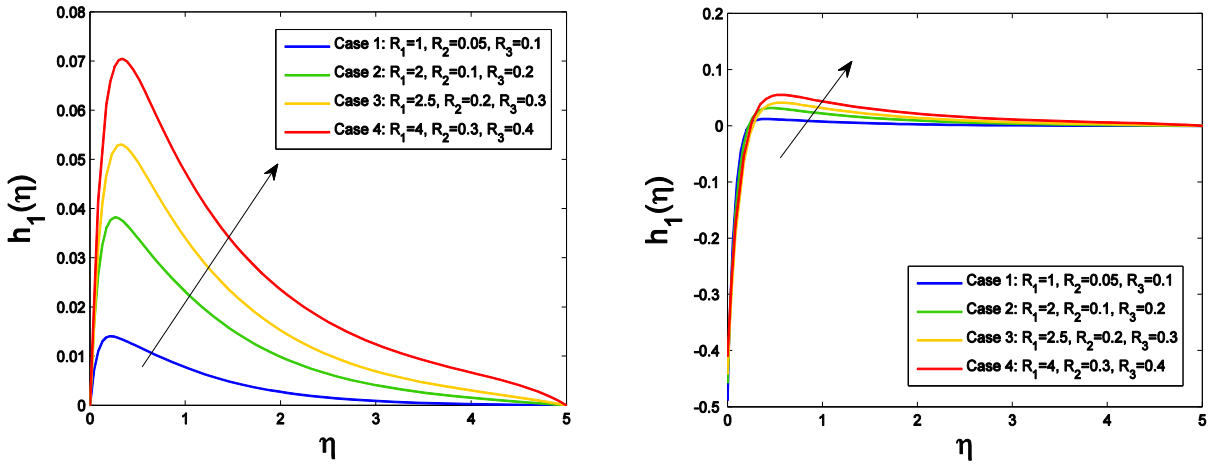

(a) **(b)**

Fig. 2.12. Behavior due to variations in R_1, R_2, R_3 on angular velocity profile $h_1(\eta)$ when **(a)** $n = 0.0$ **(b)** $n = 0.5$.

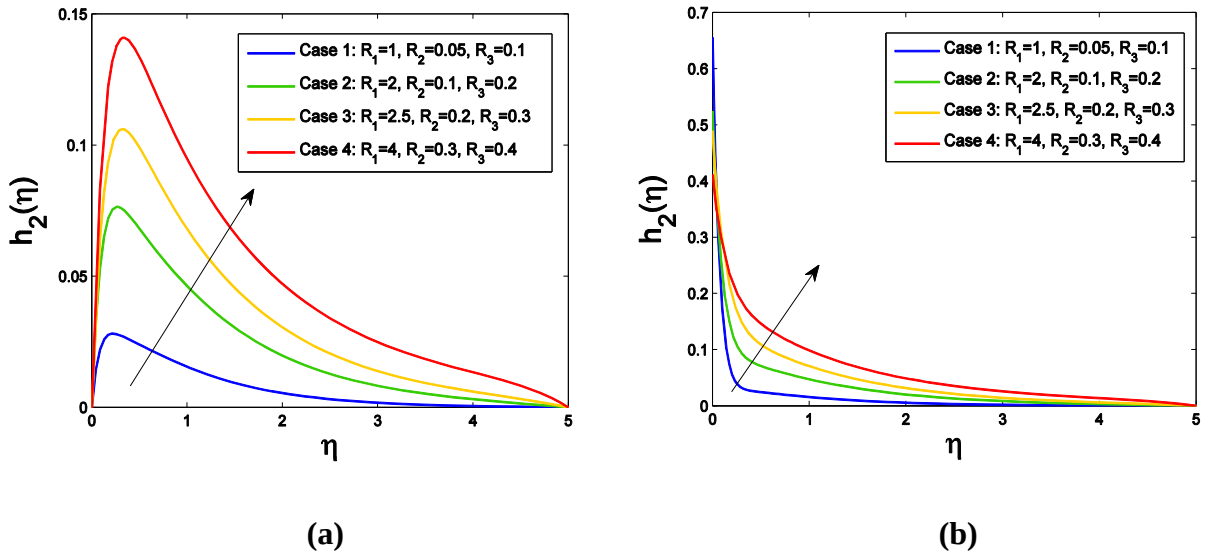

Fig. 2.13. Influence of micro-rotation parameters on $h_2(\eta)$ when **(a)** $n = 0.0$ **(b)** $n = 0.5$.

Table 2.1. Some physical properties of fluid and particles used in our study.

Thermo-physical Properties	Cu	TiO_2	Al_2O_3	Fluid phase(water)
$\rho(kg/m^3$	8933	4250	3970	997.1
$C_p(j/kg)K$	385	686.2	765	4179
$k(W/mK)$	400	8.9538	40	0.613
$\alpha \times 107(m^2/s)$	1163.1	30.7	131.7	1.47

In ***Figs. 2.2, 2.3*** and ***2.4*** scrutiny of velocity profiles $f'(\eta)$, $g'(\eta)$ in both x and y directions respectively, micro-rotation profiles $h_1(\eta)$ and $h_2(\eta)$ and temperature $\theta(\eta)$ has been performed for numerous amount of the nanoparticle's volume fraction ϕ_1. It is learnt from ***Figs. 2.2(a)*** and ***2.2(b)*** that $Cu - water$ gives a low velocity profile assessed with Al_2O_3 and TiO_2. Furthermore, in the absence of nanoparticles, water has greater velocity in comparison to all three nanofluids i.e. Copper, Alumina and Titania. Therefore, it is discovered that increment in ϕ_1 will hinder the motion of the fluid so velocity as well as the boundary layer width decreases. ***Figs. 2.3(a)*** and ***2.3(b)*** depict the behavior of the micro-

rotation profile with variation of nanoparticle volume fraction for set values of vortex viscosity parameter $R_1 = 3$. It is concluded that as we enhance ϕ_1, the behavior of $h_1(\eta)$ is decreasing while $h_2(\eta)$ is fluctuating within the domain. In case of $h_2(\eta)$ we learnt that for $\eta < 1$, the base fluid has minimal micro-rotation, whereas in case of $\eta > 1$, the base fluid exhibits a boost in micro-rotation as compared to the remaining mixture (see ***Fig. 2.3(b)***). Furthermore, it is noticed that adjacent to the wall, the effects of nanoparticles for the micro-rotation are much sturdier if compared with away from the wall. ***Fig. 2.4*** interprets the influence of $\phi_1$on temperature $\theta(\eta)$. It is evident through this graph that the base fluid has a low temperature in comparison with *Cu-water, TiO_2-water* and *Al_2O_3-water*. Increase in ϕ_1 amplifies the thermal conductivity of nanofluid and hence the thermal boundary layer.

It is demonstrated through ***Figs. 2.5, 2.6*** and ***2.7*** the impact of porosity parameter K_p on velocity distribution, micro-rotation and temperature profile. Greater values of porosity parameter relate to lower velocity as visible in ***Figs. 2.5(a)*** and ***2.5(b)***. The main dependence of porosity parameter is upon the permeability K^* of the medium. An increment in porosity results in lower permeability as they are inversely proportional, this lower permeability instigates a reduction in velocity. As the existence of porous medium causes more hindrance to fluid flow hence velocity decelerates and also the micro-rotation as observed through ***Figs. 2.6(a)*** and ***2.6(b)***. It is observed in ***Figs. 2.7*** that an elevation in porosity parameter rises the temperature noticeably. Thus, it may be concluded that owing to the resistance offered by the porous medium temperature rises.

Now we analyze the impact of boundary parameter n on velocity and angular velocity profiles via ***Figs. 2.8*** and ***2.9***. n indicates the rotation of microelements close to the wall. As mentioned earlier $n = 0$ signifies concentrated flow of particles i.e. strong concentration wherein the microelements near the surface of the wall are not able to rotate, $n = 0.5$ is used to specify the diminishing of antisymmetric fragment of the stress tensor i.e. weak concentration and $n = 1$ denotes the turbulent flows of boundary layer. It is exemplified through ***Fig. 2.8(a)*** and ***2.8(b)*** that the gradient of velocity at the surface is greater for enlarging values of n. And the couple stress $h(0)$ enlarges for higher values of n, as visible in ***Fig. 2.9(a)*** and ***2.9(b)***. Through ***Fig. 2.10(a)*** and ***2.10(b)*** a comparison between 3 diff types of nanoparticles is provided with a variation of n against velocity $f'(\eta)$ and angular

velocity $h_2(\eta)$. It is observed that Cu has a low velocity profile in comparison with Al_2O_3 and TiO_2.

Fig. 2.11(a) and ***2.11(b)*** presents the nature of velocity with changes in material parameter $R_1 = {}^{k}/_{\mu}$, which is the ratio of two viscosities of the fluid under consideration i.e. dynamic viscosity and vortex viscosity. It was revealed that the velocity enhances with an increase in R_1. This is due to the vortex viscosity which makes fluid particles speed up whereas the permeability and local inertia coefficient slows the flow motion. It is apparent from this figure that the thickness of boundary layer grows with R_1. Henceforth, there occurs a drag reduction in micropolar fluids as compared with Newtonian i.e. viscous fluids. The negative sign with velocity gradient close to the surface, $f''(0) < 0$, as displayed in ***Fig. 2.11(a)*** and ***2.11(b)*** means that there is resistance to the fluid motion due to the stretching surface. We can also notice from the figures that with a rise in stretching parameter λ there is a decrease in x-direction velocity whereas the velocity profile in y-direction amplifies. The latter behavior is due to the boundary condition $g'(0) = \lambda$.

Figs. 2.12 and ***2.13*** and are drafted to portray the behavior of R_1, R_2 and R_3 on micro-rotation profiles. ***Fig. 2.12(a)*** and ***2.12(b)*** are plotted with a variation of $n = 0$ and $n = 0.5$ respectively, with $h_1(\eta)$. In both cases an increment in the profile behavior is reported for numerous values of micropolar parameters. Similarly, ***Figs. 2.13(a)*** and ***2.13(b)*** are sketched to show variation of R_1, R_2 and R_3 on $h_2(\eta)$ when $n = 0$ and $n = 0.5$. Four different variations are evaluated, there is an enhancement witnessed in velocity profiles when $n = 0$ and $n = 0.5$. This is because as there is an increment in micropolar parameters, rotation of the micropolar components is stimulated in the boundary layer excluding the region near the surface since kinematic viscosity is dominating the flow over there. ***Table. 2.1*** illustrates some thermal and physical properties of the fluid and the metallic particles involved in our study. In ***Table. 2.2*** effects of various relevant parameters on skin frictions $\mathrm{C}f_x$ and $\mathrm{C}f_y$ and Nusselt number are displayed.

Table 2.2. Effects of various parameters upon skin friction co-efficients and Nusselt number.

R_1	n	λ	K_p	ϕ_1	Cf_x	Cf_y	$\theta'(0)$
1					**1.31474**	**0.98076**	**-1.3316**
2	**0.5**	**0.5**	**1**	**0.1**	**1.34378**	**1.17343**	**-1.4267**
3					**1.39027**	**1.25559**	**-1.5172**
1					**2.00873**	**1.00437**	**-1.3157**
2	**0.0**	**0.5**	**1**	**0.1**	**2.44874**	**1.22437**	**-1.4186**
3					**2.66306**	**1.33153**	**-1.5028**
		0.5			**1.39027**	**1.25559**	**-1.3316**
3	**0.5**	**1.0**	**1**	**0.1**	**1.48147**	**2.59159**	**-1.3316**
		1.5			**1.60774**	**4.22325**	**-1.3316**
			1		**1.39027**	**1.25559**	**-1.3316**
3	**0.5**	**0.5**	**2**	**0.1**	**1.49663**	**1.29706**	**-1.3316**
			3		**1.63583**	**1.40815**	**-1.3316**
				0	**1.6855**	**1.25559**	**-1.0000**
3	**0.5**	**0.5**	**1**	**0.1**	**1.39027**	**1.17343**	**-1.3316**
				0.15	**1.18793**	**1.09006**	**-1.5266**

2.5 Key Results

A numerical survey is implemented to investigate three-dimensional flow of micropolar nanofluid stimulated by an exponentially stretching porous surface. Influence of pertinent physical parameters upon velocities in x, y directions, angular velocities as well as on temperature profile are discussed. The main verdicts of this chapter are itemized as follows:

- Increment in nanoparticle volume fraction ϕ_1 has decreasing influence on velocity profiles whereas it increases the temperature, while the micro-rotation $h_2(\eta)$ shows a fluctuating behavior at $\eta = 1$.
- The skin friction coefficient declines for increasing values of ϕ_1, while the local Nusselt number shows an escalated behavior.
- The velocity profiles and momentum boundary layer thickness display an increasing behavior for vortex viscosity parameter R_1.
- The micro-rotation parameter R_1 exhibits increasing effects on skin friction coefficient and also an aggravating impact on the rate of heat transfer of the nanofluid.
- The micro-rotation profiles $h_1(\eta)$ and $h_2(\eta)$ have a parabolic distribution when $n = 0$.
- Both the velocity and angular velocity profiles show a decelerating behavior with increasing values of the porosity parameter K_p, while there is a rise in the temperature distribution.

Chapter 3

3. Numerical analysis of micropolar hybrid nanofluid in presence of external rotation

3.1 Introduction

In this chapter we presented a comparison between the behavior of traditional nanofluid and emerging hybrid nanofluid in the presence of micropolar fluid theory, rotation and porous medium over an exponentially stretched surface. The constructed mathematical differential system is solved numerically by means of the bvp-4c technique. The comparison between behavior of pure water, $Cu/water$ nanofluid, $Cu-TiO_2/water$ hybrid nanofluid over velocity, micro-rotation and temperature distribution has been visualized graphically. For better comprehension of flow characteristics and heat transfer rate, variation in skin friction coefficients in addition to the Nusselt number of nanofluid along with hybrid nanofluid are scrutinized. We perceive from the present study that the rate of heat transfer of nanofluid is lower than that of hybrid nanofluid even in the presence of micropolar effects, rotation and porosity.

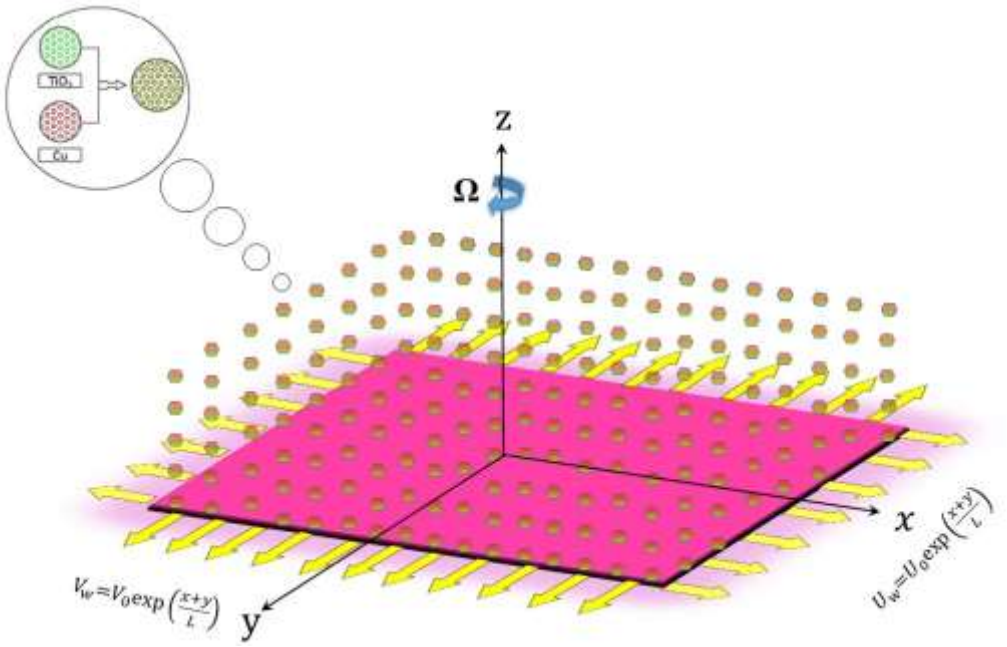

Fig. 3.1. Physical regime of the problem

3.2 Problem description

Three-dimensional rotating incompressible flow of hybrid nanofluid together with micropolar theory instigated by an exponentially stretched surface placed inside a porous media has been considered. It is presumed that surface is stretched in bilateral directions. The flow is bounded in the section $z > 0$ whereas the stretching surface is located at the plane $z = 0$ (see ***Fig. 3.1***). We have considered Copper Cu and Titanium Oxide TiO_2 nanoparticles dispersed in base fluid water H_2O. To achieve the thermal equilibrium, $Cu/water$ nanofluid is constituted by dispersing a nanoparticle volume fraction ϕ_1 in water. This particle volume fraction ϕ_1 is kept constant throughout our problem. Now, to acquire our anticipated results second nanoparticle volume fraction ϕ_2 of TiO_2 nanoparticles is disseminated in $Cu/water$ nanofluid to constitute our desired hybrid nanofluid $Cu - TiO_2/water$. Nanofluid rotates along vertical z-

axis with uniform angular velocity Ω. Implying these assumptions in conjunction with boundary layer estimation, the mathematical equations are formulated as:

$$\left[\frac{\partial u}{\partial x}+\frac{\partial v}{\partial y}+\frac{\partial w}{\partial z}\right]=0, \tag{3.1}$$

$$\left[u\frac{\partial u}{\partial x}+v\frac{\partial u}{\partial y}+w\frac{\partial u}{\partial z}-2\Omega v\right]=\left(\frac{\mu_{hnf}+k}{\rho_{hnf}}\right)\frac{\partial^2 u}{\partial z^2}-\frac{k}{\rho_{hnf}}\left(\frac{\partial N_2}{\partial z}\right)-\frac{\nu_{hnf}u}{K^*}, \tag{3.2}$$

$$\left[u\frac{\partial v}{\partial x}+v\frac{\partial v}{\partial y}+w\frac{\partial v}{\partial z}+2\Omega u\right]=\left(\frac{\mu_{hnf}+k}{\rho_{hnf}}\right)\frac{\partial^2 v}{\partial z^2}+\frac{k}{\rho_{hnf}}\left(\frac{\partial N_1}{\partial z}\right)-\frac{\nu_{hnf}v}{K^*}. \tag{3.3}$$

$$\rho_{hnf}\,j\left[u\frac{\partial N_1}{\partial x}+v\frac{\partial N_1}{\partial y}+w\frac{\partial N_1}{\partial z}\right]=\chi_{hnf}\frac{\partial^2 N_1}{\partial z^2}-2kN_1-k\frac{\partial v}{\partial z}, \tag{3.4}$$

$$\rho_{hnf}\,j\left[u\frac{\partial N_2}{\partial x}+v\frac{\partial N_2}{\partial y}+w\frac{\partial N_2}{\partial z}\right]=\chi_{hnf}\frac{\partial^2 N_2}{\partial z^2}-2kN_2+k\frac{\partial u}{\partial z}. \tag{3.5}$$

$$u\frac{\partial T}{\partial x}+v\frac{\partial T}{\partial y}+w\frac{\partial T}{\partial z}=\alpha_{hnf}\left(\frac{\partial^2 T}{\partial z^2}\right). \tag{3.6}$$

The variables involved are mathematically defined as

$$\left.\begin{aligned}
&\alpha_{hnf}=\frac{k_{hnf}}{(\rho c_p)_{hnf}},\quad \mu_{hnf}=\frac{\mu_f}{(1-\phi_1)^{2.5}(1-\phi_2)^{2.5}},\\
&\left(\rho C_p\right)_{hnf}=(1-\phi_2)\left[(1-\phi_1)\left(\rho C_p\right)_f+\phi_1\left(\rho C_p\right)_{s_1}\right]+\phi_2(\rho C_p)_{s_2},\\
&\frac{k_{hnf}}{k_{nf}}=\frac{\left(k_{s_2}+2k_{nf}\right)-2\phi_2\left(k_{nf}-k_{s_2}\right)}{\left(k_{s_2}+2k_{nf}\right)+\phi_2\left(k_{nf}-k_{s_2}\right)},\ \frac{k_{nf}}{k_f}=\frac{\left(k_{s_1}+2k_f\right)-2\phi_1\left(k_f-k_{s_1}\right)}{\left(k_{s_1}+2k_f\right)+\phi_1\left(k_f-k_{s_1}\right)},\\
&\nu_{hnf}=\frac{\mu_{hnf}}{\rho_{hnf}},\quad \rho_{hnf}=(1-\phi_2)\left[(1-\phi_1)\rho_f+\phi_1\rho_{s_1}\right]+\phi_2\rho_{s_2},\\
&\chi_{hnf}=(\mu_{hnf}+k/2)\,j,\quad \Omega=\Omega_0 e^{\frac{x+y}{L}},
\end{aligned}\right\} \tag{3.7}$$

Here the subscripts hnf, nf and f are employed for hybrid nanofluid, nanofluid and the base fluid respectively while s_1 is for Cu nanoparticles and s_2 is used to denote TiO_2 nanoparticles.

Boundary Conditions

$$\left.\begin{aligned} &u = U_w,\ v = V_w,\ T = T_w,\ N_1 = n\frac{\partial v}{\partial z},\ N_2 = -n\frac{\partial u}{\partial z},\ \text{at } z = 0,\\ &u \to 0,\ v \to 0,\ T \to T_\infty,\ N_1 \to 0,\ N_2 \to 0, \qquad \text{as } z \to \infty. \end{aligned}\right\} \tag{3.8}$$

The stretching velocities on the surface and the temperature close to the wall are described as follows:

$$U_w = U_0 e^{\frac{x+y}{L}},\ V_w = V_0 e^{\frac{x+y}{L}},\ T_w = T_\infty + T_0 e^{\frac{B(x+y)}{2L}}. \tag{3.9}$$

Similarity transmutations are listed below:

$$\left.\begin{aligned} &u = U_0 e^{\frac{x+y}{L}} f'(\eta),\ v = U_0 e^{\frac{x+y}{L}} g'(\eta),\ w = -\left(\frac{\nu U_0}{2L}\right)^{\frac{1}{2}} e^{\frac{x+y}{2L}} \left[f + \eta f' + g + \eta g'\right],\\ &N_1 = \frac{U_0}{2\nu L}\left(2U_0 \nu L\right)^{\frac{1}{2}} e^{3\left(\frac{x+y}{2L}\right)} h_1(\eta),\ N_2 = \frac{U_0}{2\nu L}\left(2U_0 \nu L\right)^{\frac{1}{2}} e^{3\left(\frac{x+y}{2L}\right)} h_2(\eta),\\ &T = T_\infty + T_0 e^{\frac{B(x+y)}{2L}} \theta(\eta),\ \eta = \left(\frac{U_0}{2\nu L}\right)^{\frac{1}{2}} e^{\frac{x+y}{2L}} z. \end{aligned}\right\} \tag{3.10}$$

These transformations are applied on eq's. (3.1-3.6), resulting in continuity equation being satisfied identically whereas momentum, micro rotational and energy equations reduce into the following form:

$$\frac{\rho_f}{\rho_{hnf}}\left(A_2(\phi)+R_1\right)f'''+f''(f+g)-2f'(f'+g')-\frac{\rho_f}{\rho_{hnf}}R_1h_2'-\frac{\nu_{hnf}}{\nu_f}K_pf'+4\varepsilon g'=0, \tag{3.11}$$

$$\frac{\rho_f}{\rho_{hnf}}\left(A_2(\phi)+R_1\right)g'''+g''(f+g)-2g'(f'+g')+\frac{\rho_f}{\rho_{hnf}}R_1h_1'-\frac{\nu_{hnf}}{\nu_f}K_pg'-4\varepsilon f'=0, \tag{3.12}$$

$$\frac{\rho_f}{\rho_{hnf}}R_2h_1''-R_1R_3(2h_1+g'')-3h_1(f'+g')+h_1'(f+g)=0, \tag{3.13}$$

$$\frac{\rho_f}{\rho_{hnf}}R_2h_2''-R_1R_3(2h_2-f'')-3h_2(f'+g')+h_2'(f+g)=0, \tag{3.14}$$

$$\frac{1}{\Pr}\frac{k_{hnf}/k_f}{(1-\phi_2)\left[(1-\phi_1)+\phi_1\dfrac{(\rho C_p)_{s_1}}{(\rho C_p)_f}\right]+\phi_2\dfrac{(\rho C_p)_{s_2}}{(\rho C_p)_f}}\theta''-B(f'+g')\theta+(f+g)\theta'=0. \tag{3.15}$$

And associated boundary conditions are transformed as follows:

$$\left.\begin{aligned} &f(0)=0,\ f'(0)=1,\\ &g(0)=0,\ g'(0)=\lambda,\ \theta(0)=0,\\ &h_1(0)=ng''(0),\ h_2(0)=-nf''(0), \quad as\ \eta\to 0,\\ &f'\to 0,\ g'\to 0,\ \theta\to 0,\\ &h_1\to 0,\ h_2\to 0, \qquad\qquad as\ \eta\to\infty. \end{aligned}\right\} \tag{3.16}$$

The dimensionless parameters are mathematically represented as:

$$\left.\begin{aligned} &\mathrm{R}_1=\frac{k}{\mu},\ \mathrm{R}_2=\frac{\chi_{hnf}}{\mu j},\ \mathrm{R}_3=\frac{2\nu L}{jU_w},\ K_p=\frac{2\nu L}{K^*U_w},\ \Pr=\frac{(\mu C_p)_f}{k_f},\ \lambda=\frac{V_0}{U_0},\\ &\varepsilon=\frac{\Omega_0 L}{U_0}\quad and\quad A_2(\phi)=\frac{\mu_{hnf}}{\mu_f}=\frac{1}{(1-\phi_1)^{2.5}(1-\phi_2)^{2.5}}. \end{aligned}\right\} \tag{3.17}$$

The skin friction coefficients in addition to the Nusselt number are stated as:

$$C_{fx} = \frac{\tau_{wx}}{\frac{1}{2}\rho_{nf} U_w^2}, \; C_{fy} = \frac{\tau_{wy}}{\frac{1}{2}\rho_{nf} U_w^2}, \; Nu_x = \frac{x q_w}{k_f (T_w - T_\infty)}, \tag{3.18}$$

τ_{wx}, τ_{wy} and q_w are mathematically defined as:

$$\left.\begin{aligned} \tau_{wx} &= \left(\mu_{hnf} + k\right)\left(\frac{\partial u}{\partial z}\right)_{z=0} + k\left(N_2\right)_{z=0}, \\ \tau_{wy} &= \left(\mu_{hnf} + k\right)\left(\frac{\partial v}{\partial z}\right)_{z=0} + k\left(N_1\right)_{z=0}, \\ q_w &= -k_{hnf}\left(\frac{\partial T}{\partial z}\right)_{z=0}. \end{aligned}\right\} \tag{3.19}$$

In dimensionless form, the coefficients of skin friction and Nusselt number can be represented as:

$$\left.\begin{aligned} \frac{1}{\sqrt{2}} C_{fx} \left(\mathrm{Re}\right)^{\frac{1}{2}} &= \left(\frac{A_2(\phi) + (1-n)R_1}{(1-\phi_2)\left[(1-\phi_1) + \phi_1(\rho_{s_1}/\rho_f)\right] + \phi_2(\rho_{s_2}/\rho_f)}\right) f''(0), \\ \frac{1}{\sqrt{2}} C_{fy} \left(\mathrm{Re}\right)^{\frac{1}{2}} &= \left(\frac{A_2(\phi) + (1-n)R_1}{(1-\phi_2)\left[(1-\phi_1) + \phi_1(\rho_{s_1}/\rho_f)\right] + \phi_2(\rho_{s_2}/\rho_f)}\right) g''(0), \\ \sqrt{2}\,\frac{L}{x} Nu_x \,\mathrm{Re}^{-\frac{1}{2}} &= -\frac{k_{hnf}}{k_f}\theta'(0). \end{aligned}\right\} \tag{3.20}$$

3.3 Solution procedure

The coupled non-linear ODE's (3.11-3.15) accompanied by boundary conditions specified in equation (3.16) are numerically calculated invoking bvp-4c technique. For this procedure, initially the set of equations (3.11-3.15) accompanied by boundary conditions (3.16) are converted to first order differential equations. To solve this system, Newton's method is utilized and the derivatives are calculated approximately using the finite difference method. The solver

then approximates the error in the obtained numerical solution over every subinterval. In case the solution fails to attain the convergence criterion of 10^{-4}, the solver employs the mesh and the process is reiterated. The points of the initial mesh in addition to an initial estimation of the solution, which satisfied the boundary conditions, were provided.

3.4 Outcomes

The outcomes of the numerical analysis portraying the impact of several pertinent parameters upon velocity profile, micro rotation and temperature distribution are presented in graphical and tabular form below.

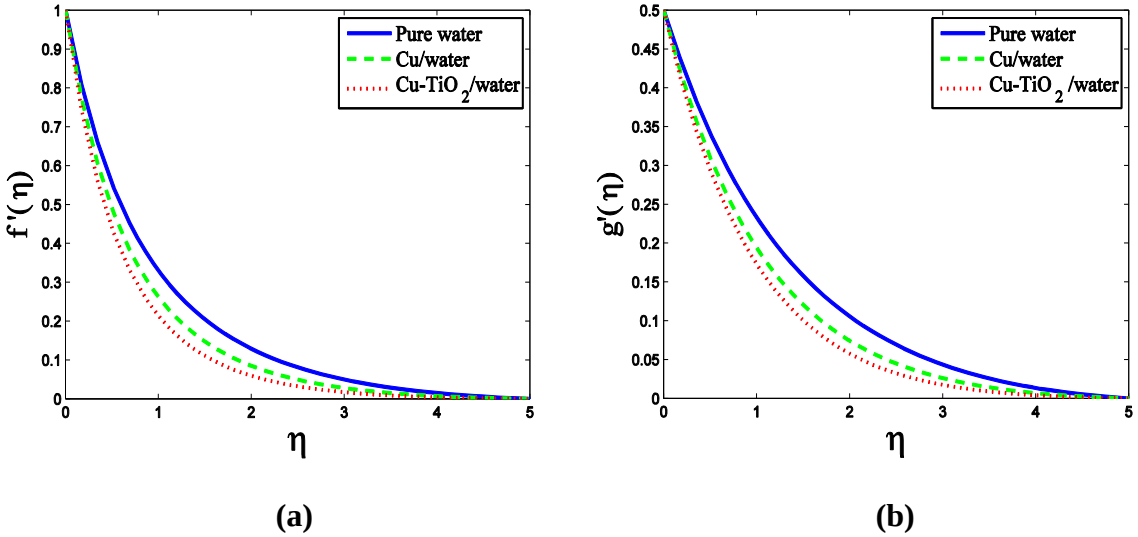

Fig. 3.2. Comparison of velocity profiles $f'(\eta)$ of water, nanofluid and hybrid in **(a)** x-direction $f'(\eta)$ and **(b)** y-direction $g'(\eta)$.

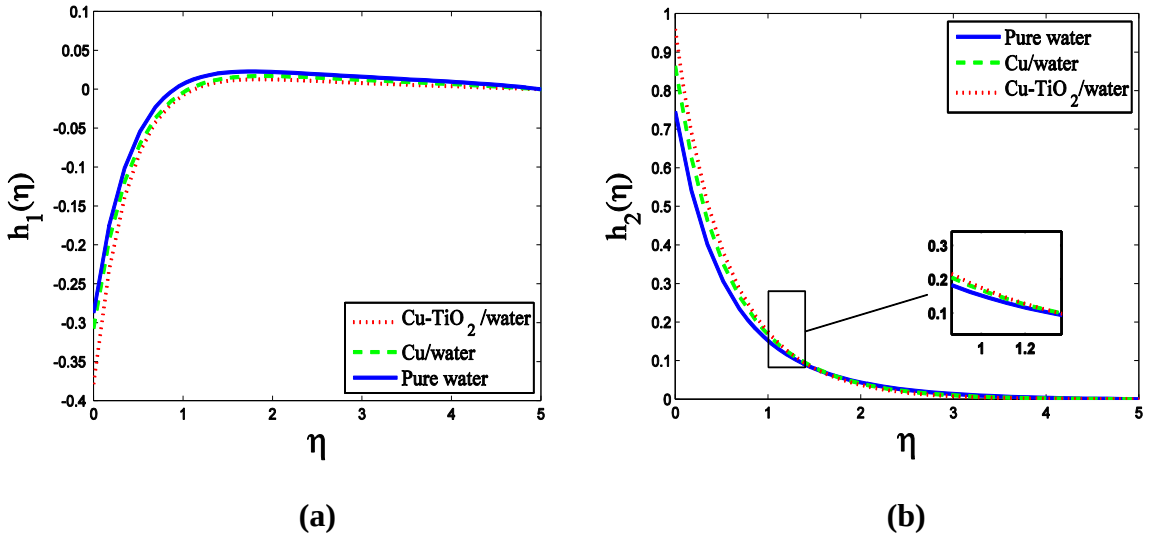

Fig. 3.3. Comparison of water, nanofluid and hybrid nanofluid's micro-rotational components **(a)** $h_1(\eta)$ and **(b)** $h_2(\eta)$.

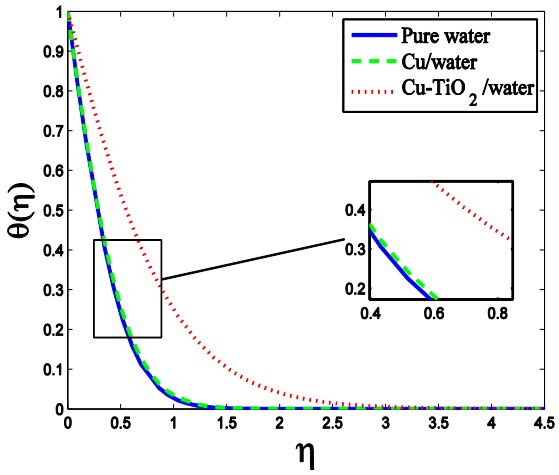

Fig. 3.4. Comparison of temperature distribution $\theta(\eta)$ for different fluids.

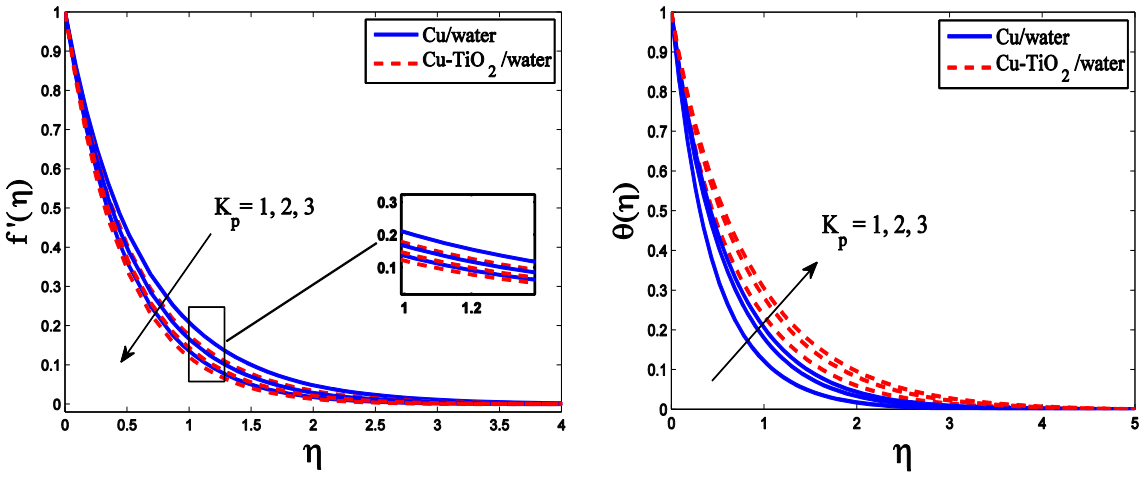

Fig. 3.5. Changes in (a) velocity $f'(\eta)$ (b) temperature profiles against K_p.

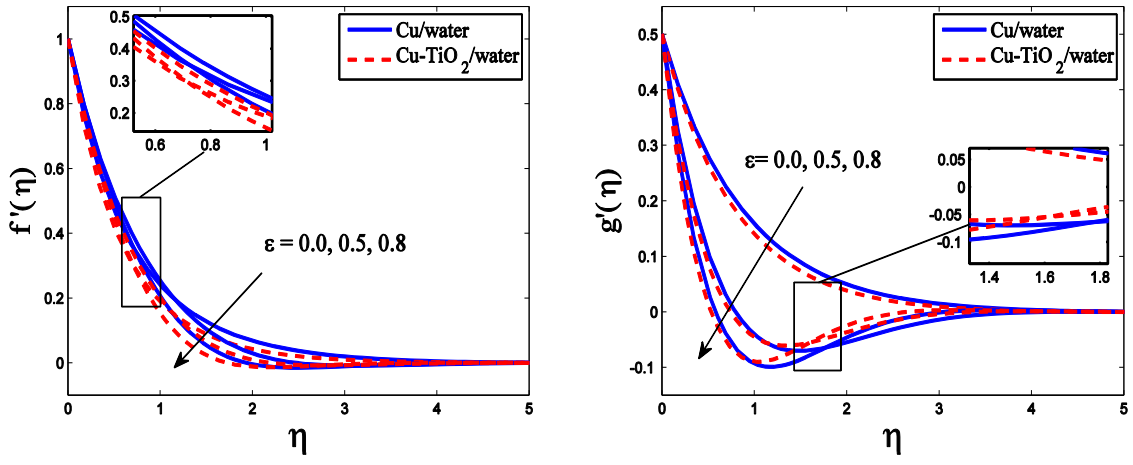

Fig. 3.6. Comparison between velocity (a) x-direction $f'(\eta)$ and (b) y-direction $g'(\eta)$.

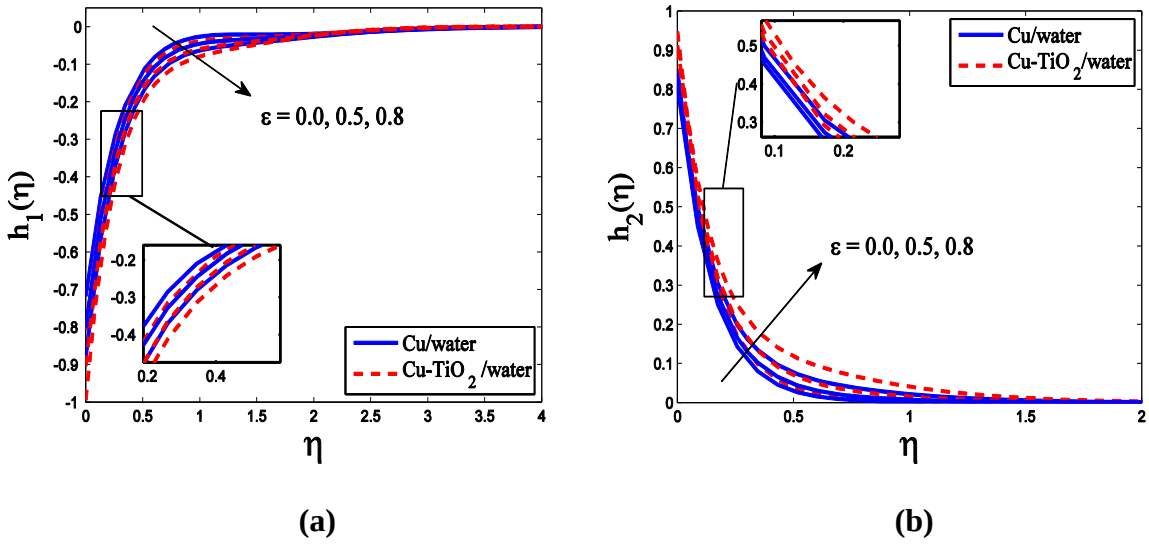

(a) **(b)**

Fig. 3.7. Comparison between micro-rotation **(a)** $h_1(\eta)$ and **(b)** $h_2(\eta)$ of nanofluid and hybrid nanofluid with variation of rotation ε.

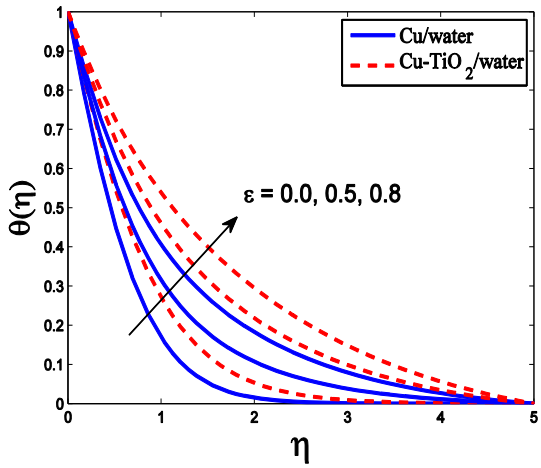

Fig. 3.8. Influence of the rotation parameter upon temperature profile of hybrid and simple nanofluid.

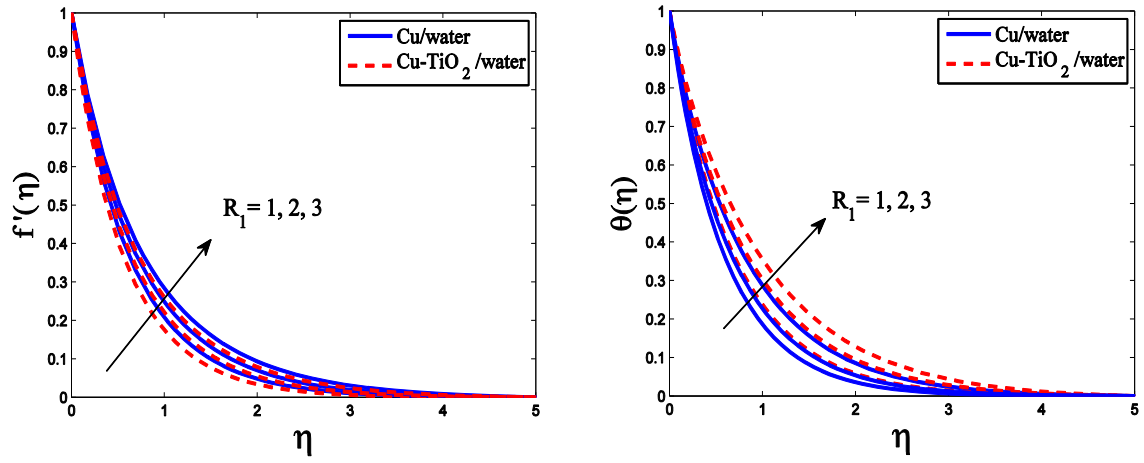

Fig. 3.9. Influence of R_1 on velocity profile **(a)** x-direction $f'(\eta)$ and **(b)** temperature.

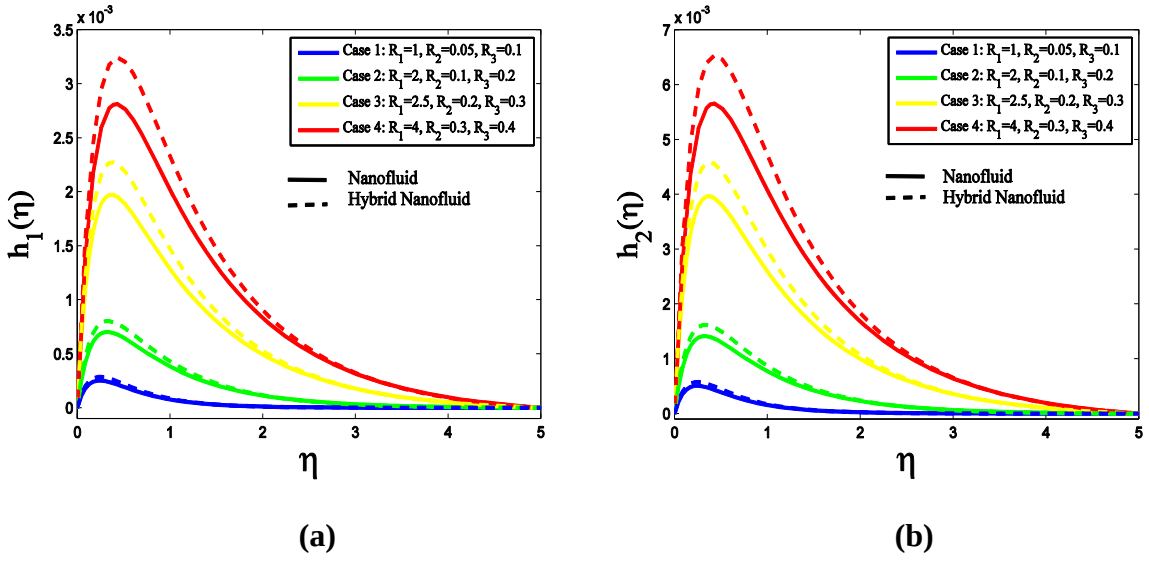

Fig. 3.10. Influence of R_1, R_2, R_3 on micro-rotation profiles **(a)** $h_1(\eta)$ and **(b)** $h_2(\eta)$ at $n = 0$.

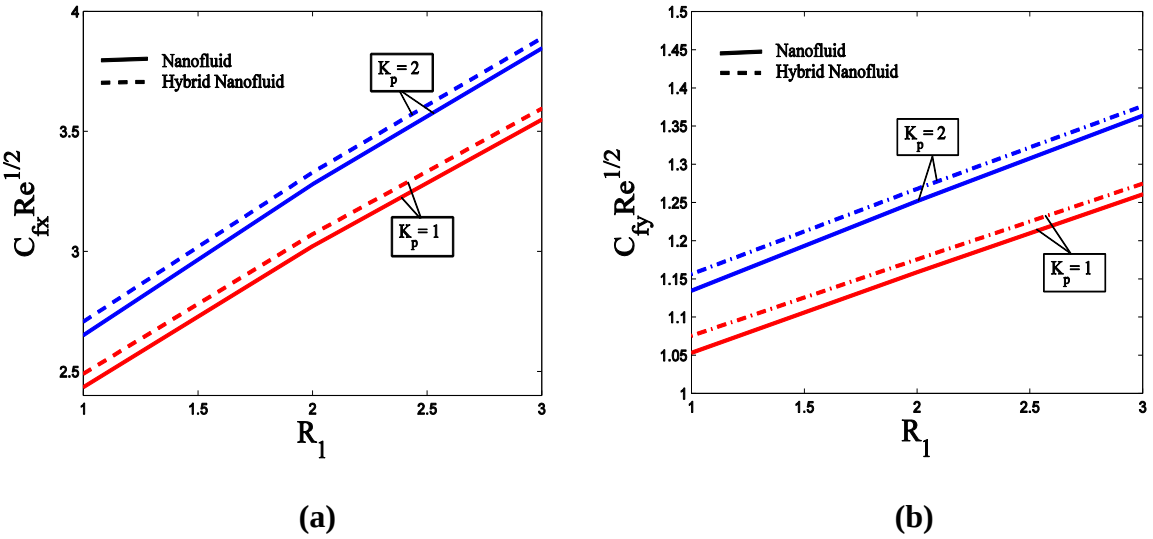

Fig. 3.11. Comparison of skin friction coefficients **(a)** C_{fx} **(b)** C_{fy} of nanofluid and hybrid nanofluid for different values K_p and R_1.

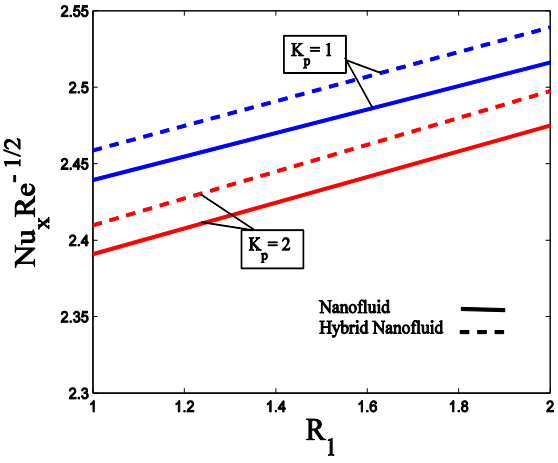

Fig. 3.12. Comparison of Nusselt number for nanofluid and hybrid nanofluid with variation in vortex viscosity and porosity parameter.

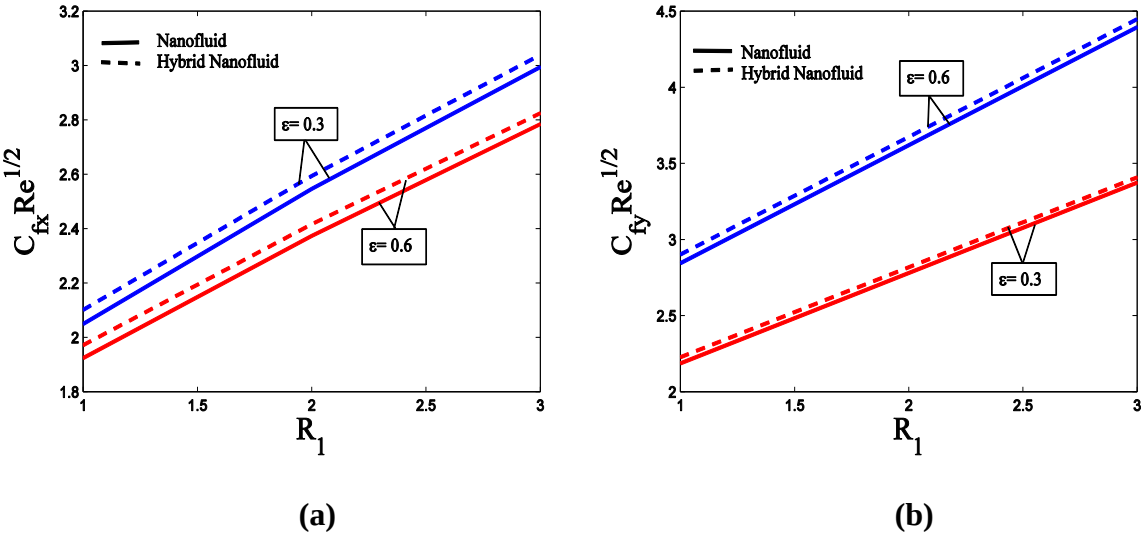

Fig. 3.13. Comparison of skin friction coefficients **(a)** C_{fx} **(b)** C_{fy} of nanofluid and hybrid nanofluid for different values ε and R_1.

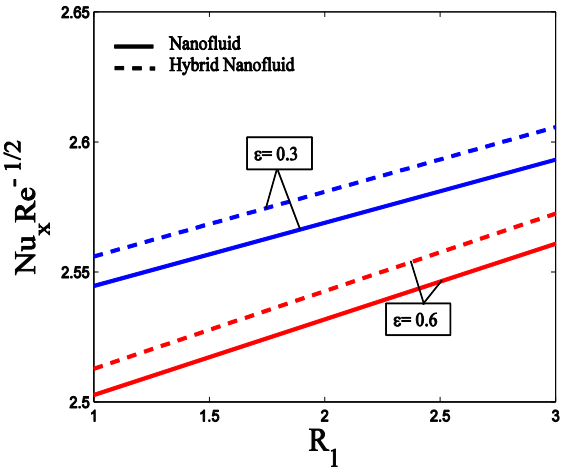

Fig. 3.14. Comparison of local Nusselt number of nanofluid and hybrid nanofluid.

Figs. 3.2, 3.3 and ***3.4*** exhibit analysis of velocity profiles $f'(\eta)$, $g'(\eta)$ in x and y directions respectively, micro-rotation profiles $h_1(\eta)$ and $h_2(\eta)$ and temperature profile $\theta(\eta)$, presenting a comparison between simple base fluid water, nanofluid $(Cu/water)$ and hybrid nanofluid

($Cu - TiO_2/water$). Velocity profile for pure water is observed to be the highest followed by $Cu/water$ and then $Cu - TiO_2/water$. Density and dynamic viscosity are the causes of reduction in fluid velocity which are enhanced by hybridity as there is addition of more colossal particles so as a result velocity decreases. It is learnt from ***Figs. 3.3(a)*** and ***3.3(b)*** that micro-rotation velocity is augmented with increase in number of nanoparticles as there will be more particle rotation. ***Fig. 3.4*** shows the behavior of temperature profile for water, nanofluid and hybrid nanofluid. It is elucidated that the temperature profile for hybrid nanofluid is significantly higher as compared to nanofluid and water. Further addition of nanoparticles exerts more energy and rises the temperature as well as increases the thermal boundary layer thickness. Moreover, it is also visualized that even under the similar circumstances and equal summative quantities of nanoparticle volume fraction, $Cu - TiO_2/water$ hybrid nanofluid achieves higher temperature as compared to nanofluid ($Cu/water$). Due to hybrid nanofluid ($Cu - TiO_2/water$) a sudden increase in temperature is observed since it boosts the thermal conductivity.

Figs. 3.5(a) and ***3.5(b)*** illustrate the conduct of velocity and temperature distribution with variation of porosity parameter K_p along with comparison of nanofluid ($Cu/water$) and hybrid nanofluid ($Cu - TiO_2/water$). A reduction in velocity is instigated due to the increment in porosity parameter K_p since increase in porosity lowers the permeability because of being inversely proportional so there is a greater obstruction to fluid flow hence velocity decelerates. It is witnessed via ***Fig. 3.5(b)*** that the greater the porosity parameter K_p is, the higher the temperature will be which is because of the resistance caused by porous medium.

Through ***Figs. 3.6, 3.7*** and ***3.8*** the effect on velocity profiles $f'(\eta)$, $g'(\eta)$, micro-rotation profiles $h_1(\eta)$, $h_2(\eta)$ and temperature profile $\theta(\eta)$ against the variation of rotation parameter ε is portrayed for nanofluid ($Cu/water$) in addition to hybrid nanofluid ($Cu-TiO_2/water$). For minor values of η the velocity fields in x direction $f'(\eta)$ as well as in y direction $g'(\eta)$ reduce monotonically with increment in ε in both the cases of nanofluid ($Cu/water$) and hybrid nanofluid ($Cu-TiO_2/water$). However, the variation in $f'(\eta)$ and $g'(\eta)$ with ε is non-monotonic when η is sufficiently large. In fact, there is an oscillatory behavior in the profiles near the wall which is due to rotation effects. Physically as ε enlarges, rotation effects become dominant as compared to stretching effects this causes the fluctuating behavior and hence decelerate the flow. Now we observed by means of ***Figs. 3.7(a)*** and ***3.7*****(b)** that with an increase in ε the micro-rotations also increase this is ascribed to the fact that rotational effects enhance the molecular motions and interactions increasing the micro-rotations of particles. ***Fig. 3.8*** illustrates that if we increase the rotation parameter the temperature rises. Due to boost in rotation, the particle motion and interactions are intensified causing the viscous forces to enhance which resists the fluid motion so consequently temperature increases.

Figs. 3.9(a) and ***3.9(b)*** exhibit the nature of velocity profile and temperature profile of $Cu/water$ and $Cu-TiO_2/water$ with variation of parameter $R_1 = {}^{k}/_{\mu}$, known as the material parameter that provides the ratio of two viscosities, the vortex viscosity and the dynamic viscosity. As the material parameter R_1 increases the velocity escalates since the fluid particles are accelerated due to vortex viscosity. It is perceptible from ***Fig. 3.9(a)*** that the thickness of boundary layer extends with R_1. Whereas it is learnt from ***Fig. 3.9(b)*** that temperature shoots up because of the drag reduction offered by micropolar fluids which causes resistance to the fluid motion. We also perceive from this figure that the temperature of hybrid nanofluid ($Cu-TiO_2/$

$water$) is higher than ($Cu/water$) nanofluid. ***Figs. 3.10(a)*** and ***3.10(b)*** delineates the behavior of R_1, R_2 and R_3 on micro-rotation profiles $h_1(\eta)$ and $h_2(\eta)$ for hybrid nanofluid besides mono-nanofluid. Four different variations of micropolar parameters are evaluated and in both directions an enhancement in the profile behavior is recorded, concurrently we observe that the micro-rotations in case of hybrid nanofluid ($Cu - TiO_2/water$) are much intense as compared to simple nanofluid ($Cu/water$). With an increase in the micropolar parameters, rotation of the micropolar components is stimulated in the boundary layer apart from the region adjacent to the surface as kinematic viscosity governs the flow.

The effects of R_1 and K_p upon skin friction coefficients C_{fx} and C_{fy} are displayed in ***Fig. 3.11(a)*** and ***3.11(b)***. We comprehend from these figures that as we increase R_1 and K_p both the skin friction co-efficients C_{fx} and C_{fy} intensify. While ***Fig. 3.12*** reveals that hybrid nanofluid has a higher heat transfer rate as compared to mono-nanofluid. And the Nusselt number declines with rise in the porosity parameter where as it increases with increment in material parameter R_1. In ***Figs. 3.13*** and ***3.14*** we explored the impact of rotation parameter ε along with R_1 over skin friction co-efficients and Nusselt number. Skin friction co-efficient in the x-direction decreases however it increases in the y-direction.

Table 3.1. Some physical properties of fluid and particles used in our study.

Thermo-physical Properties	**Cu**	$\boldsymbol{TiO_2}$	**Fluid phase(water)**
$\boldsymbol{\rho(kg/m^3)}$	**8933**	**4250**	**997.1**
$\boldsymbol{C_p(j/kg)K}$	**385**	**686.2**	**4179**
$\boldsymbol{k(W/mK)}$	**400**	**8.9538**	**0.613**
$\boldsymbol{\alpha \times 107(m^2/s)}$	**1163.1**	**30.7**	**1.47**

Table 3.2. Effects of pertinent parameters on Skin friction coefficients in x and y direction for nanofluid and hybrid nanofluid.

R_1	ε	λ	K_p	ϕ_2	$\frac{-1}{(1-\phi_1)^{2.5}} f''(0)$	$\frac{-(1-\phi_2)^{-2.5}}{(1-\phi_1)^{2.5}} f''(0)$	$\frac{-1}{(1-\phi_1)^{2.5}} g''(0)$	$\frac{-(1-\phi_2)^{-2.5}}{(1-\phi_1)^{2.5}} g''(0)$
1					**2.11377**	**2.76532**	**1.95947**	**2.14307**
2	**0.5**	**0.5**	**1**	**0.1**	**2.28644**	**2.93451**	**2.17343**	**2.34267**
3					**2.40597**	**3.11802**	**2.35661**	**2.51726**
	0.2				**2.26306**	**2.94826**	**1.70437**	**2.02793**
1	**0.5**	**0.5**	**1**	**0.1**	**2.11377**	**2.76532**	**1.95947**	**2.14307**
	0.8				**1.90873**	**2.55348**	**2.23153**	**2.35028**
		0.5			**2.11377**	**2.76532**	**1.95947**	**2.14307**
1	**0.5**	**1.0**	**1**	**0.1**	**2.32486**	**2.91746**	**2.39159**	**2.35691**
		1.5			**2.50774**	**3.12975**	**3.12325**	**2.61317**
			1		**2.11377**	**2.76532**	**1.95947**	**2.14307**
1	**0.5**	**0.5**	**2**	**0.1**	**2.49663**	**2.96510**	**2.29706**	**2.28712**
			3		**2.63583**	**3.17654**	**2.40815**	**2.39450**
				0	**1.6855**	**3.07389**	**2.38356**	**2.46207**
1	**0.5**	**0.5**	**1**	**0.1**	**1.39027**	**2.76532**	**1.95947**	**2.14307**
				0.15	**1.18793**	**2.28749**	**1.59006**	**1.5266**

Table 3.3. Effects of a number of parameters upon Nusselt number for nanofluid and hybrid nanofluid.

R_1	ε	λ	K_p	ϕ_2	$\frac{-K_{nf}}{K_f}\theta'(0)$	$\frac{-K_{hnf}}{K_f}\theta'(0)$
1					**2.11377**	**2.76532**
2	**0.5**	**0.5**	**1**	**0.1**	**2.28644**	**2.93451**
3					**2.40597**	**3.11802**
	0.2				**2.26306**	**2.94826**
1	**0.5**	**0.5**	**1**	**0.1**	**2.11377**	**2.76532**
	0.8				**1.90873**	**2.55348**
		0.5			**2.11377**	**2.76532**
1	**0.5**	**1.0**	**1**	**0.1**	**2.32486**	**2.91746**
		1.5			**2.50774**	**3.12975**
			1		**2.11377**	**2.76532**
1	**0.5**	**0.5**	**2**	**0.1**	**2.49663**	**2.96510**
			3		**2.63583**	**3.17654**
				0	**1.6855**	**3.14790**
1	**0.5**	**0.5**	**1**	**0.1**	**1.39027**	**2.76532**
				0.15	**1.18793**	**2.19824**

3.5 Conclusion

A numerical investigation on the steady three-dimensional boundary layer flow of micropolar hybrid nanofluid past an exponentially stretching surface has been executed in the presence of rotation and porous medium. A qualitative comparison between $Cu/water$ nanofluid and $Cu-TiO_2/water$ hybrid nanofluid was involved for the examination. The main findings of current analysis are itemized as follows:

- We observe that in the case of hybrid nanofluid the heat transfer rate is substantially high in comparison with simple nanofluid.
- There is also seen a visible increment in the temperature of the micropolar hybrid nanofluid even under the same quantity of nanoparticle volume fraction.
- Due to rotation, the velocity profile decreases of both hybrid and simple nanofluid.
- Local Nusselt number increases due to hybridity as well as with increment in particle volume fraction and vortex viscosity parameter R_1 but decreases with augmentation in rotation and porosity parameter.
- The skin friction coefficients $C_{fx}\ and\ C_{fy}$ escalate for increasing values of vortex viscosity parameter R_1, stretching ratio parameter λ, and porosity parameter K_p both in the case of nanofluid and hybrid nanofluid.
- Rotation parameter ε has diminishing impact on C_{fx} whereas opposite behavior is witnessed in case of C_{fy} for both nanofluid and hybrid nanofluid.
- The micro-rotation profiles $h_1(\eta)$ and $h_2(\eta)$ exhibit a parabolic distribution at $n = 0$.
- Velocity and micro-rotation profiles decelerate with higher values of the porosity parameter K_p, but there is a rise in temperature distribution.

Chapter 4

4. Unsteady MHD flow of micropolar hybrid nanofluid

4.1 Introduction

This chapter gives an insight into the magnetohydrodynamic flow of time dependent rotating hybrid nanofluid with micropolar fluid theory. The medium containing the fluid is considered as porous while the surface is being stretched exponentially. Mathematical composition of this problem is then numerically solved utilizing bvp-4c technique. An assessment between flow behavior and properties of conventional nanofluid along with hybrid nanofluid upon velocity profiles, micro-rotation and temperature distribution is presented. Additionally, modifications in the local Nusselt number of nanofluid as well as hybrid nanofluid have been observed.

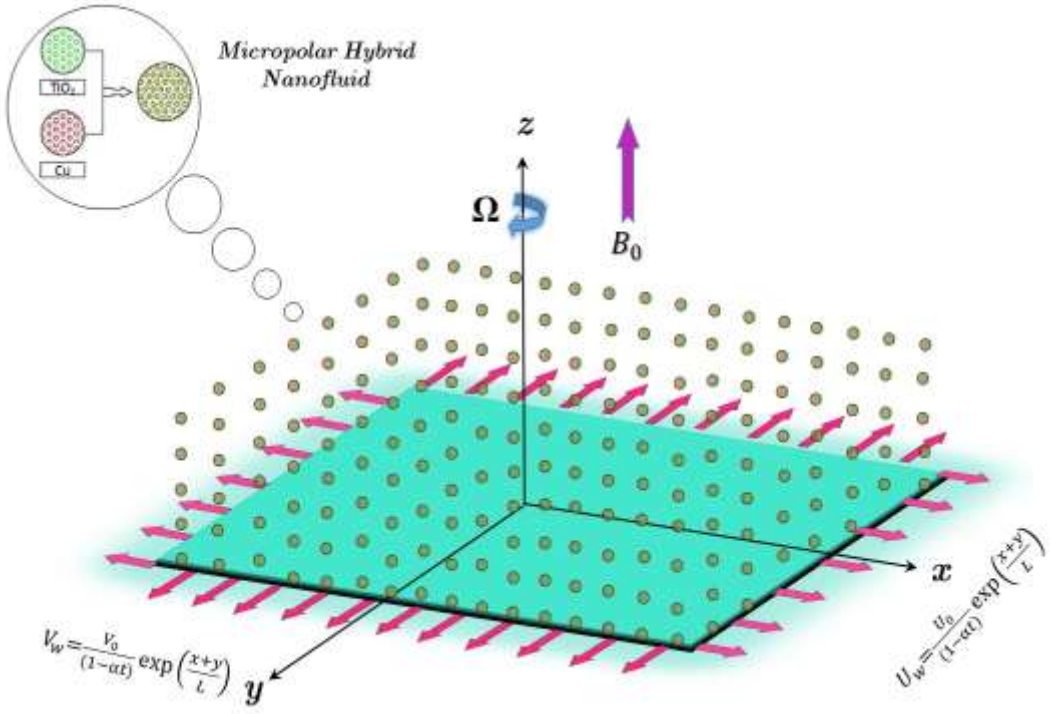

Fig. 4.1. Flow description of the problem

4.2 Problem description

We have considered a three dimensional time dependent rotating flow of an electric conductor micropolar hybrid nanofluid as a consequence of an exponentially stretched region coinciding with the plane at $z = 0$. The medium is considered as porous and flow is confined in the section $z > 0$. Surface is being stretched along *x* and *y*-axis in both directions as shown through ***Fig. 4.1***. A magnetic field having constant intensity B_0 is taken in perpendicular direction to the surface parallel to z-axis. By invoking these assumptions in addition to boundary layer estimation, the governing equations are formulated as:

$$\left[\frac{\partial u}{\partial x}+\frac{\partial v}{\partial y}+\frac{\partial w}{\partial z}\right]=0, \tag{4.1}$$

$$\left[\frac{\partial u}{\partial t}+u\frac{\partial u}{\partial x}+v\frac{\partial u}{\partial y}+w\frac{\partial u}{\partial z}-2\Omega v\right]=\left(\frac{\mu_{hnf}+k}{\rho_{hnf}}\right)\frac{\partial^2 u}{\partial z^2}-\frac{k}{\rho_{hnf}}\left(\frac{\partial N_2}{\partial z}\right)-\frac{\nu_{hnf}}{K^*}u-\frac{\sigma_{hnf}B_0^2}{\rho_{hnf}}u, \tag{4.2}$$

$$\left[\frac{\partial v}{\partial t}+u\frac{\partial v}{\partial x}+v\frac{\partial v}{\partial y}+w\frac{\partial v}{\partial z}+2\Omega u\right]=\left(\frac{\mu_{hnf}+k}{\rho_{hnf}}\right)\frac{\partial^2 v}{\partial z^2}+\frac{k}{\rho_{hnf}}\left(\frac{\partial N_1}{\partial z}\right)-\frac{\nu_{hnf}}{K^*}v-\frac{\sigma_{hnf}B_0^2}{\rho_{hnf}}v. \tag{4.3}$$

$$\rho_{hnf}\,j\left[\frac{\partial N_1}{\partial t}+u\frac{\partial N_1}{\partial x}+v\frac{\partial N_1}{\partial y}+w\frac{\partial N_1}{\partial z}\right]=\chi_{hnf}\frac{\partial^2 N_1}{\partial z^2}-2kN_1-k\frac{\partial v}{\partial z}, \tag{4.4}$$

$$\rho_{hnf}\,j\left[\frac{\partial N_2}{\partial t}+u\frac{\partial N_2}{\partial x}+v\frac{\partial N_2}{\partial y}+w\frac{\partial N_2}{\partial z}\right]=\chi_{hnf}\frac{\partial^2 N_2}{\partial z^2}-2kN_2+k\frac{\partial u}{\partial z}. \tag{4.5}$$

$$\frac{\partial T}{\partial t}+u\frac{\partial T}{\partial x}+v\frac{\partial T}{\partial y}+w\frac{\partial T}{\partial z}=\alpha_{hnf}\left(\frac{\partial^2 T}{\partial z^2}\right). \tag{4.6}$$

Boundary Conditions

$$\left.\begin{aligned} &u = U_w,\ v = V_w,\ T = T_w,\ N_1 = n\frac{\partial v}{\partial z},\ N_2 = -n\frac{\partial u}{\partial z},\ \text{at } z = 0,\\ &u \to 0,\ v \to 0,\ T \to T_\infty,\ N_1 \to 0,\ N_2 \to 0, \qquad \text{as } z \to \infty. \end{aligned}\right\} \tag{4.8}$$

The velocities at the surface and temperature close to the wall are described as follows:

$$U_w = \frac{U_0}{(1-\alpha t)} e^{\frac{x+y}{L}},\ V_w = \frac{V_0}{(1-\alpha t)} e^{\frac{x+y}{L}},\ T_w = T_\infty + \frac{T_0}{(1-\alpha t)^2} e^{\frac{B(x+y)}{2L}}. \tag{4.9}$$

Below are the similarity transformations incorporated in this chapter:

$$\left.\begin{aligned} &u = \frac{U_0}{(1-\alpha t)} e^{\frac{x+y}{L}} f'(\eta),\ v = \frac{U_0}{(1-\alpha t)} e^{\frac{x+y}{L}} g'(\eta),\\ &w = -\left(\frac{\nu U_0}{2L(1-\alpha t)}\right)^{\frac{1}{2}} e^{\frac{x+y}{2L}} \{ f + \eta f' + g + \eta g' \},\\ &N_1 = \frac{U_0 (U_0 2\nu L)^{\frac{1}{2}}}{2\nu L (1-\alpha t)^{\frac{3}{2}}} e^{3\left(\frac{x+y}{2L}\right)} h_1(\eta),\ N_2 = \frac{U_0 (U_0 2\nu L)^{\frac{1}{2}}}{2\nu L (1-\alpha t)^{\frac{3}{2}}} e^{3\left(\frac{x+y}{2L}\right)} h_2(\eta),\\ &T = T_\infty + \frac{T_0}{(1-\alpha t)^2} e^{\frac{B(x+y)}{2L}} \theta(\eta),\ \eta = \left(\frac{U_0}{2\nu L(1-\alpha t)}\right)^{\frac{1}{2}} e^{\frac{x+y}{2L}} z. \end{aligned}\right\} \tag{4.10}$$

By employing these transformations on eq's. (4.2 - 4.6) momentum, micro-rotational and temperature equations convert to the following equations:

$$\frac{\rho_f}{\rho_{hnf}}\left(A_2(\phi)+R_1\right)f'''+f''(f+g)-2f'(f'+g')-\frac{\rho_f}{\rho_{hnf}}R_1h_2'-\frac{\nu_{hnf}}{\nu_f}K_pf' \\ +4\varepsilon g'-Mf'-A\left(2f'+\eta f''\right)=0, \tag{4.11}$$

$$\frac{\rho_f}{\rho_{hnf}}\left(A_2(\phi)+R_1\right)g'''+g''(f+g)-2g'(f'+g')+\frac{\rho_f}{\rho_{hnf}}R_1h_1'-\frac{\nu_{hnf}}{\nu_f}K_pg' \\ -4\varepsilon f'-Mg'-A\left(2g'+\eta g''\right)=0, \tag{4.12}$$

$$\frac{\rho_f}{\rho_{hnf}}\left(\left(A_2(\phi)+\frac{R_1}{2}\right)h_1''-R_1(2h_1+g'')\right)-3h_1(f'+g')+h_1'(f+g)-A\left(3h_1+\eta h_1'\right)=0, \tag{4.13}$$

$$\frac{\rho_f}{\rho_{hnf}}\left(\left(A_2(\phi)+\frac{R_1}{2}\right)h_2''-R_1(2h_2-f'')\right)-3h_2(f'+g')+h_2'(f+g)-A\left(3h_2+\eta h_2'\right)=0, \tag{4.14}$$

$$\frac{1}{\Pr}\frac{\left(k_{hnf}/k_f\right)\theta''}{\left[\left(1-\phi_2\right)\left\{(1-\phi_1)+\phi_1\frac{\left(\rho C_p\right)_{s_1}}{\left(\rho C_p\right)_f}\right\}+\phi_2\frac{(\rho C_p)_{s_2}}{\left(\rho C_p\right)_f}\right]}-B\left(f'+g'\right)\theta+\left(f+g\right)\theta'-A\left(4\theta+\eta\theta'\right)=0. \tag{4.15}$$

Boundary conditions are transformed as follows:

$$\left.\begin{aligned} &f(0)=0,\ f'(0)=1, \\ &g(0)=0,\ g'(0)=\lambda,\ \theta(0)=0, \\ &h_1(0)=ng''(0),\ h_2(0)=-nf''(0), \quad as\ \eta\to 0, \\ &f'\to 0,\ g'\to 0,\ \theta\to 0, \\ &h_1\to 0,\ h_2\to 0, \qquad as\ \eta\to\infty. \end{aligned}\right\} \tag{4.16}$$

The dimensionless parameters involved in eq's (4.11-4.15) are mathematically represented as:

$$\left.\begin{aligned} \mathrm{R}_1 = \frac{k}{\mu},\ M = \frac{2\sigma_{hnf} B_0^2 L}{\rho_{hnf} U_w},\ K_p = \frac{2\nu L}{K^* U_w},\ \mathrm{Pr} = \frac{\left(\mu C_p\right)_f}{k_f},\ \lambda = \frac{V_0}{U_0}, \\ A = \frac{\alpha L}{U_0 e^{\frac{x+y}{L}}},\ \varepsilon = \frac{\Omega_0 L}{U_0}\ \ and\ \ A_2(\phi) = \frac{\mu_{hnf}}{\mu_f} = \frac{1}{\left(1-\phi_1\right)^{2.5}\left(1-\phi_2\right)^{2.5}}. \end{aligned}\right\} \tag{4.17}$$

The skin friction coefficients in addition to the Nusselt number are stated as:

$$C_{fx} = \frac{\tau_{wx}}{\frac{1}{2}\rho_{nf} U_w^2},\ C_{fy} = \frac{\tau_{wy}}{\frac{1}{2}\rho_{nf} U_w^2},\ Nu_x = \frac{x q_w}{k_f (T_w - T_\infty)}, \tag{4.18}$$

Where τ_{wx}, τ_{wy} represent shear stresses at the surface and q_w denotes the surface heat flux, mathematically defined as:

$$\left.\begin{aligned} \tau_{wx} = \left(\mu_{hnf} + k\right)\left(\frac{\partial u}{\partial z}\right)_{z=0} + k\left(N_2\right)_{z=0}, \\ \tau_{wy} = \left(\mu_{hnf} + k\right)\left(\frac{\partial v}{\partial z}\right)_{z=0} + k\left(N_1\right)_{z=0}, \\ q_w = -k_{hnf}\left(\frac{\partial T}{\partial z}\right)_{z=0}. \end{aligned}\right\} \tag{4.19}$$

In non-dimensional form, the skin friction coefficients and Nusselt number are represented as follows, where $\mathrm{Re} = \frac{U_w L}{\nu}$:

$$\left.\begin{aligned} \frac{1}{\sqrt{2}} C_{fx} \left(\mathrm{Re}\right)^{\frac{1}{2}} = \left(\frac{A_2(\phi) + (1-n)R_1}{(1-\phi_2)\left[(1-\phi_1) + \phi_1(\rho_{s_1}/\rho_f)\right] + \phi_2(\rho_{s_2}/\rho_f)}\right) f''(0), \\ \frac{1}{\sqrt{2}} C_{fy} \left(\mathrm{Re}\right)^{\frac{1}{2}} = \left(\frac{A_2(\phi) + (1-n)R_1}{(1-\phi_2)\left[(1-\phi_1) + \phi_1(\rho_{s_1}/\rho_f)\right] + \phi_2(\rho_{s_2}/\rho_f)}\right) g''(0), \\ \sqrt{2}\,\frac{L}{x} Nu_x\, \mathrm{Re}^{-\frac{1}{2}} = -\frac{k_{hnf}}{k_f}\theta'(0). \end{aligned}\right\} \tag{4.20}$$

4.3 Numerical Technique

It is very challenging to find the exact solutions of highly non-linear and coupled ODE's (4.11 - 4.15) hence the numerical solution is attained using the bvp-4c technique. The complete process of the built-in MATLAB program bvp-4c is explained in detail by [71]. In this technique, the set of equations (4.11 - 4.15) alongside boundary conditions (4.16) have been converted to first order linear differential equations. Subsequently suitable initial guesses are chosen which satisfy boundary conditions. A convergence criterion of 10^{-4} is set for the acquired solution.

4.4 Outcomes and Discussion

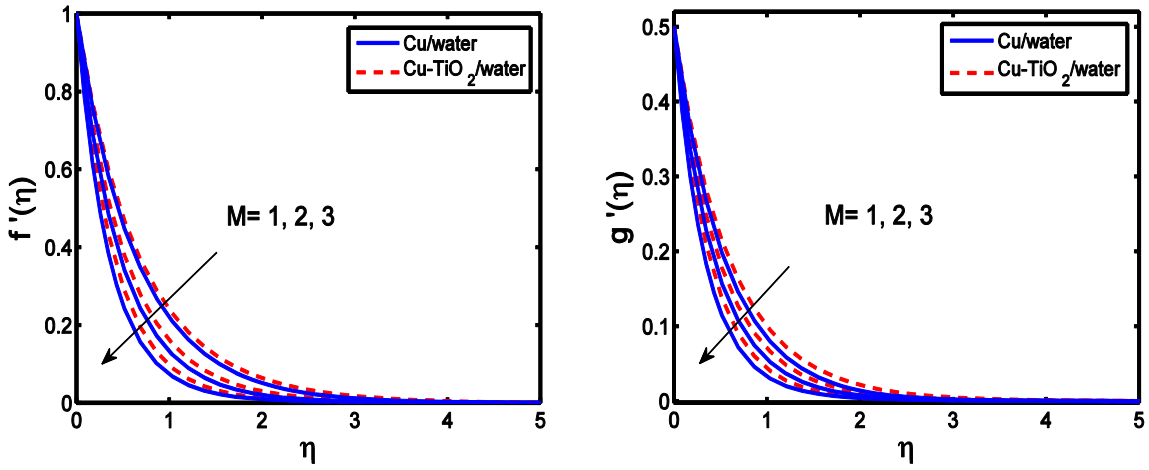

(a) **(b)**

Fig. 4.2. Comparison of velocity field **(a)** $f'(\eta)$ and **(b)** $g'(\eta)$ between nanofluid and hybrid nanofluid w.r.t *M*.

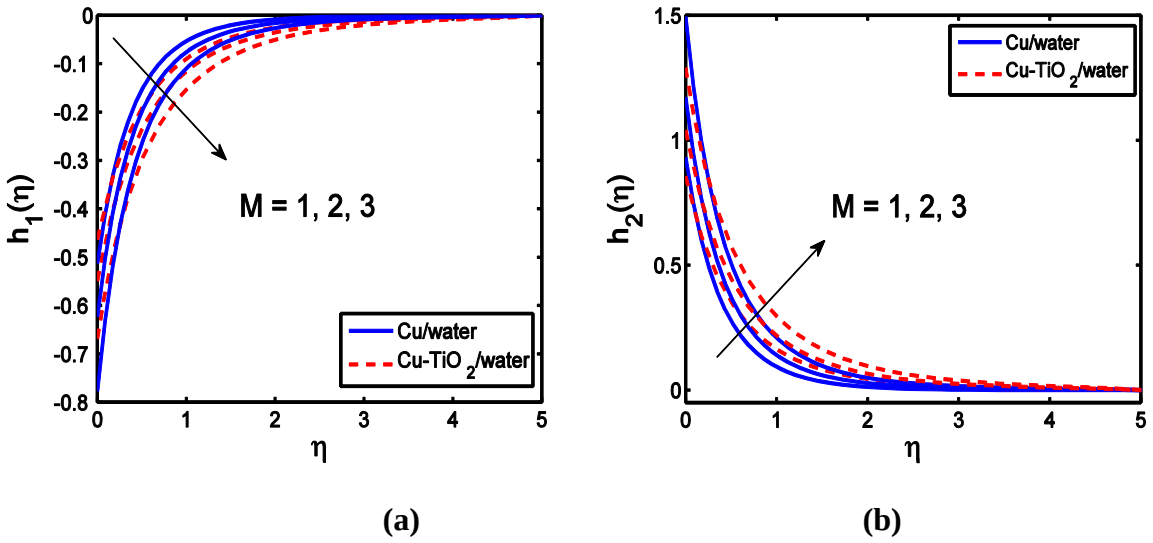

Fig. 4.3. Comparison of micro-rotation profiles **(a)** $h_1(\eta)$ and **(b)** $h_2(\eta)$of nanofluid and hybrid nanofluid for variation in *M*.

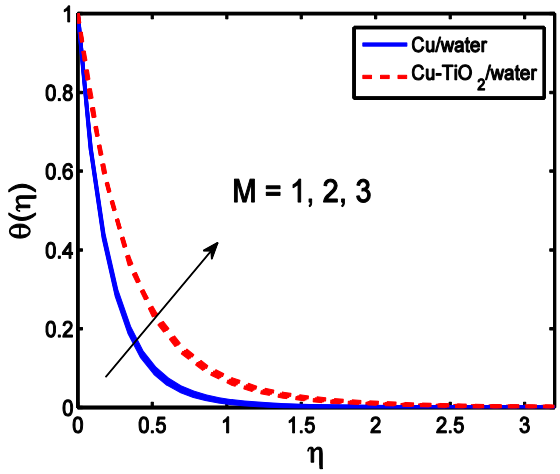

Fig. 4.4. Comparison of temperature distribution with magnetic field parameter.

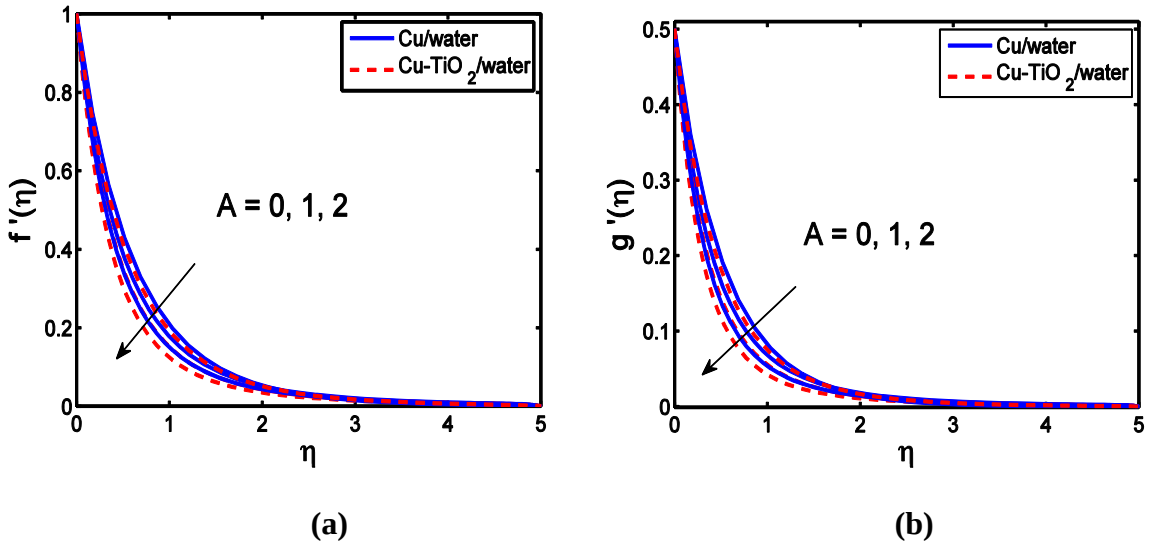

Fig. 4.5. Comparison between velocity **(a)** $f'(\eta)$ and **(b)** $g'(\eta)$ of $Cu/water$ and $Cu - TiO_2/water$ with variation of unsteadiness parameter.

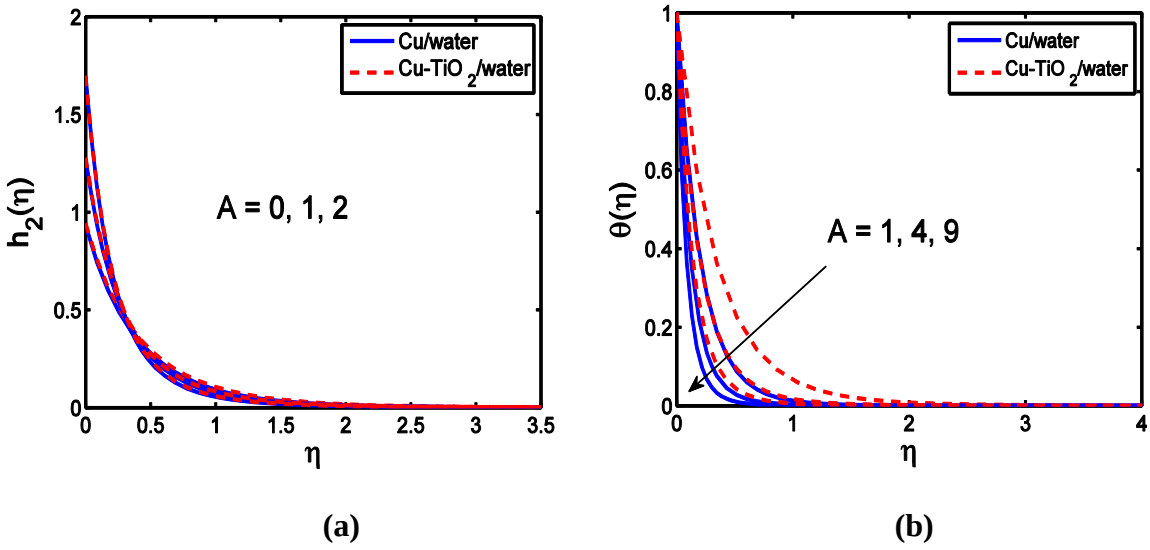

Fig. 4.6. Comparison between **(a)** micro-rotation $h_2(\eta)$ and **(b)** temperature of $Cu/water$ and $Cu - TiO_2/water$ with variation of unsteadiness parameter.

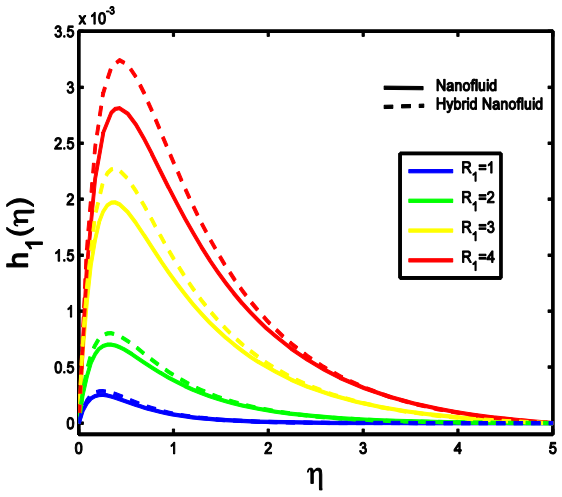

Fig. 4.7. Resulting behavior of micro-rotation profile $h_1(\eta)$ due to variations in R_1 at $n = 0$.

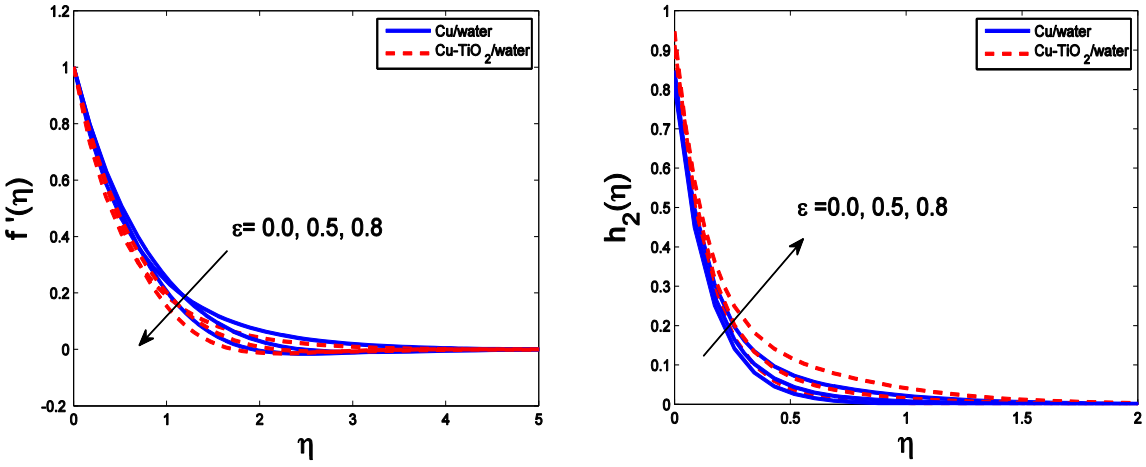

Fig. 4.8. Comparison of **(a)** velocity field $f'(\eta)$ **(b)** micro-rotation profile $h_2(\eta)$ with variation of rotation parameter ε.

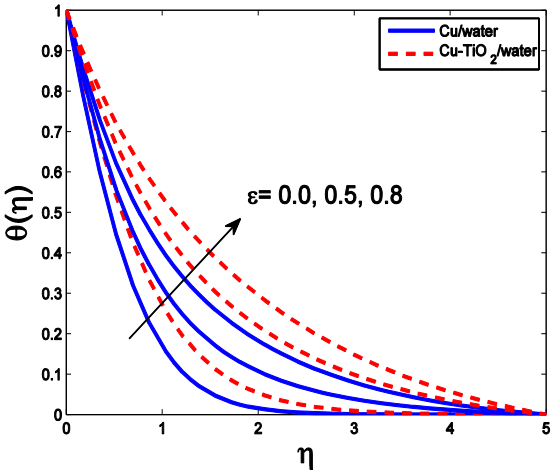

Fig. 4.9. Variation of rotation parameter ε for temperature distribution of hybrid and simple nanofluid.

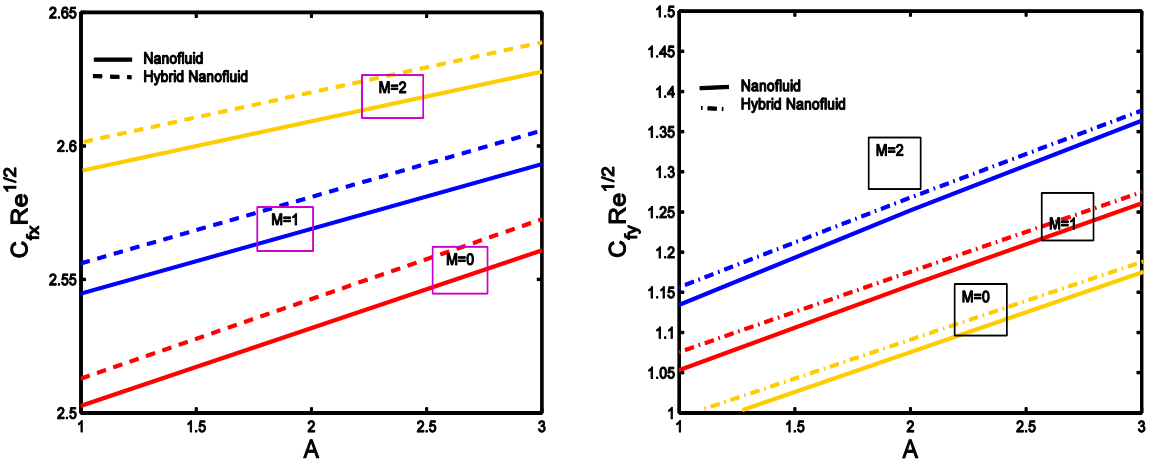

(a) **(b)**

Fig. 4.10. Comparison of skin friction coefficients **(a)** C_{fx} **(b)** C_{fy} between nanofluid along with hybrid nanofluid against modifications in values of M and A.

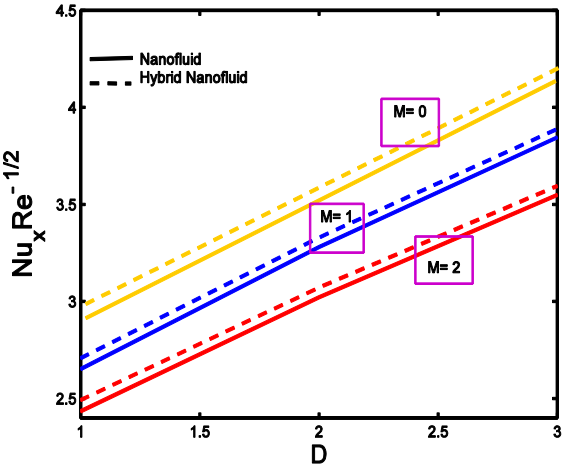

Fig. 4.11. Comparison of Nusselt number against changes in values of *M* and *A*.

The following outcomes and discussion are based upon numerical analysis for three-dimensional flow of micropolar hybrid nanofluid. The linear velocity plus micro-rotation and temperature profiles are exhibited through ***Figs. 4.2 - 4.9*** giving a comparison between nanofluid and hybrid nanofluid. Additionally local skin friction and Nusselt number are also evaluated through ***Figs. 4.10, 4.11*** and ***Tables. 4.3-4.4***. ***Table. 4.1*** and ***Table. 4.2*** present a comparison of our results with previously published work validating our outcomes.

Magnetic field parameter

Figs. 4.2, 4.3 and ***4.4*** are drawn to depict the conduct of magnetic field over velocity, micro-rotation and temperature profiles also comparing flow behaviors of nanofluid ($Cu/water$) and hybrid nanofluid ($Cu - TiO_2/water$). From ***Figs. 4.2(a)*** and ***4.2(b)*** it is evident that the velocity in x and y directions decline as the value of magnetic parameter increments. This is because as the magnetic field is in the oblique direction of the electrically conducting fluid, Lorentz force (which is a resistive force) is created which increases resistance to the flow. Through ***Figs. 4.3(a)*** and ***4.3(b)*** we can note that micro-rotation profiles $h_1(\eta)$ and $h_2(\eta)$

decrease with increase in magnetic field parameter. ***Fig. 4.4*** demonstrates the conduct of temperature distribution for hybrid nanofluid besides simple nanofluid. The temperature rises as the intensity of magnetic field increases as heat is generated due to the resistive nature of the Lorentz force. We also observed that hybrid nanofluid has higher temperature in comparison to mono nanofluid. Through ***Figs. 4.10*** and ***4.11*** the impact of magnetic field upon skin friction coefficients and heat transfer rate can be witnessed. It is noticed through ***Fig. 4.10*** that for intense magnetic field the value of skin friction coefficients increases. Physically, this is as a consequence of the Lorentz force which increases the friction. The conduct of local Nusselt number is presented through ***Fig. 4.11*** and ***Table 4.4*** along with variation of magnetic field parameter and it is perceived that level of heat transfer declines as *M* increases. Magnetic field parameter is the proportion of electromagnetic forces to viscous forces therefore when it is increased the electromagnetic forces become dominant reducing the rate of heat transfer near the surface.

Unsteadiness parameter

The impact of the unsteadiness parameter *A* upon velocity profiles $f'(\eta)$, $g'(\eta)$ in x and y directions respectively, micro-rotation profile $h_2(\eta)$ and temperature profile $\theta(\eta)$ can be witnessed in ***Figs. 4.5*** and ***4.6***. The type of motion is determined by the value of *A*, *A=0* corresponds to steady case while $A \neq 0$ corresponds to unsteady motion. A drop in linear as well as angular velocity is observed when unsteadiness parameter is increased but for angular velocity this outcome is opposite far away from the surface. As *A* increases there is a decrease in temperature profile because when we increase *A* the surface temperature gradient also increases resulting in higher heat transfer level. Thus, for greater values of *A* the rate of cooling is very fast. From ***Figs. 4.10*** and ***4.11*** the influence of unsteadiness parameter on skin friction co-

efficients and Nusselt number is observed. Unlike steady flows, the unsteady flow has higher rate of skin friction and heat transfer. The greater the value of unsteadiness parameter the greater is the gradient of velocity at the surface resulting in an increase in skin friction coefficients.

Material parameter R_1

Fig. 4.7 shows us the impact of the vortex viscosity parameter on micro-rotation profile. Variations of micropolar parameters are evaluated and improvement in micro-rotation's of the fluid is noticed, alongside we perceive that the micro-rotation's in case of micropolar hybrid nanofluid ($Cu - TiO_2/water$) are stronger in comparison with simple nanofluid ($Cu/water$).

R_1 demonstrates the ratio of vortex to dynamic viscosities. Physically, when $R_1 < 1$ it means that dynamic viscosity is dominant and fluid becomes thick so the velocity declines. When $R_1 = 1$ it represents that dynamic and vortex viscosity are of same magnitude. Thus we have normal fluid velocity. For $R_1 > 1$ depicts that vortex viscosity is greater than dynamic viscosity so here fluid velocity accelerates. Increasing the micropolar parameter induces rotation of micropolar modules around the boundary layer excluding the section close to the surface since kinematic viscosity administers the flow over there.

Rotation parameter ε

A fluctuating behavior of velocity is identified in ***Fig. 4.8(a)*** with variation in the rotation parameter ε for nanofluid alongside hybrid nanofluid. Physically as ε increases, influence of rotation gets dominant over the stretching effects this causing the fluctuating behavior and consequentially decelerating the flow. In ***Fig. 4.8(b)*** we observe that as the value of rotation parameter increases the micro-rotations of the particles also increase. Reason behind this

behavior is that rotational effects enhance the molecular motion and interactions increasing the micro-rotation. ***Fig. 4.9*** demonstrates that by amplifying the rotation parameter the temperature proliferates. This is due to enhancement in rotation which intensifies the motion of particles and interactions causing the viscous forces to boost which resists the fluid motion.

Table 4.1. Comparison with the existing literature for Skin friction of traditional nanofluid taking $\phi_2 = R_1 = \varepsilon = A = K_p = 0$.

ϕ_1	b_1	λ	Nadeem et al.	Present analysis
0.1	**-0.5**	**0.5**	**-2.39997**	**-2.39994**
		1.5	**-3.09835**	**-3.09832**
0.2	**0.5**	**0.5**	**-3.34046**	**-3.34044**
		1.5	**-4.31252**	**-4.31250**

Table 4.2. Comparison with existing literature for heat transfer rate of traditional nanofluid taking $\phi_2 = R_1 = \varepsilon = A = K_p = 0$.

ϕ_1	b_1	λ	Nadeem et al.	Present analysis
0.1	**-0.5**	**0.5**	**4.78978**	**4.78982**
		1.5	**7.36737**	**7.36741**
0.2	**0.5**	**0.5**	**1.13201**	**1.13206**
		1.5	**1.13124**	**1.13128**

Table 4.3. Effect of pertinent parameters on Skin friction coefficients.

M	R_1	ε	A	K_p	ϕ_2	$\frac{-1}{(1-\phi_1)^{2.5}} f''(0)$	$\frac{-(1-\phi_2)^{-2.5}}{(1-\phi_1)^{2.5}} f''(0)$	$\frac{-1}{(1-\phi_1)^{2.5}} g''(0)$	$\frac{-(1-\phi_2)^{-2.5}}{(1-\phi_1)^{2.5}} g''(0)$
1						**2.62834**	**2.68390**	**1.13698**	**1.58294**
2	**1**	**0.5**	**1**	**1**	**0.1**	**2.69741**	**2.72386**	**1.19430**	**1.86492**
3						**2.73206**	**2.78438**	**1.26935**	**2.23682**
	1					**2.62834**	**2.68390**	**1.13698**	**1.58294**
1	**2**	**0.5**	**1**	**1**	**0.1**	**2.85624**	**2.83451**	**1.27343**	**2.34267**
	3					**2.98597**	**2.91802**	**1.43861**	**2.51726**
		0.2				**2.71305**	**2.84826**	**1.08497**	**2.02793**
1	**1**	**0.5**	**1**	**1**	**0.1**	**2.62834**	**2.68390**	**1.13698**	**1.58294**
		0.8				**2.39873**	**2.55348**	**1.31453**	**2.35028**
			1			**2.62834**	**2.68390**	**1.13698**	**1.58294**
1	**1**	**0.5**	**2**	**1**	**0.1**	**2.71890**	**2.91746**	**1.39159**	**1.75691**
			3			**2.96576**	**3.12975**	**1.41925**	**1.97317**
				1		**2.62834**	**2.68390**	**1.13698**	**1.58294**
1	**1**	**0.5**	**1**	**2**	**0.1**	**2.87498**	**2.96510**	**1.29706**	**1.61712**
				3		**3.12930**	**3.17654**	**1.40815**	**1.87450**
					0	**2.62834**	**2.62834**	**0.87365**	**1.04627**
1	**1**	**0.5**	**1**	**1**	**0.05**	**2.62834**	**2.65342**	**1.09542**	**1.36357**
					0.1	**2.62834**	**2.68390**	**1.13698**	**1.58294**

Table 4.4. Impact of several relevant parameters on Nusselt number.

M	R_1	ε	A	K_p	ϕ_2	$\frac{-K_{nf}}{K_f}\theta'(0)$	$\frac{-K_{hnf}}{K_f}\theta'(0)$
1						**2.84917**	**3.17824**
2	**1**	**0.5**	**1**	**1**	**0.1**	**2.73956**	**2.94620**
3						**2.63485**	**2.81798**
	1					**2.84917**	**3.17824**
1	**2**	**0.5**	**1**	**1**	**0.1**	**2.98614**	**3.31751**
	3					**3.20597**	**3.45102**
		0.2				**2.96306**	**3.39425**
1	**1**	**0.5**	**1**	**1**	**0.1**	**2.84917**	**3.17824**
		0.8				**2.60873**	**2.85348**
			1			**2.84917**	**3.17824**
1	**1**	**0.5**	**2**	**1**	**0.1**	**2.96482**	**3.32510**
			3			**3.21574**	**3.57654**
				1		**2.84917**	**3.17824**
1	**1**	**0.5**	**0.5**	**2**	**0.1**	**2.71905**	**2.96043**
				3		**2.58346**	**2.75328**
					0	**2.84917**	**2.84917**
1	**1**	**0.5**	**0.5**	**1**	**0.05**	**2.84917**	**2.96532**
					0.1	**2.84917**	**3.17824**

4.5 Conclusion

Unsteady magnetohydrodynamic 3D flow of micropolar hybrid nanofluid prompted by the exponentially stretching of the surface beneath the fluid is examined numerically. Also, the effects of rotation and porosity have been considered. A qualitative comparison between nanofluid and hybrid nanofluid was presented for better analysis. The noteworthy findings of present work are enumerated below:

- We perceive from this study that the level of heat transfer of hybrid nanofluid is significantly higher in comparison with simple mono-nanofluid.
- For stronger magnetic field both linear and angular velocities decrease whereas the temperature increases.
- A decrease in linear as well as angular velocities and in the temperature distribution is observed when unsteadiness parameter is increased but for angular velocity this outcome is opposite far away from the surface.
- The values of skin friction co-efficients C_{fx} and C_{fy} enhance with magnetic field parameter M, unsteadiness parameter A, vortex viscosity parameter R_1, and porosity parameter K_p for both nanofluid and hybrid nanofluid.
- Local Nusselt number increases due to hybridity, unsteadiness and vortex viscosity parameter R_1 but declines with intensification in magnetic field, porosity parameter and rotation.
- Rotation parameter ε reduces the x component of skin friction while opposite conduct is witnessed in case of C_{fy} for nanofluid and hybrid nanofluid.

Chapter 5

5. Magnetohydrodynamic flow of micropolar hybrid nanofluid: Entropy generation analysis

5.1 Introduction

This section is committed to examine the aspects of MHD, viscous dissipation as well as thermal radiation upon micropolar hybrid nanofluid flow past an exponentially stretching/shrinking sheet. Numerical results of the governing equations are obtained and in contrary to a stretching sheet we discover that dual solutions occur in case of shrinking sheet. The implication of parameters on velocity, micro-rotation, temperature, surface friction, Nusselt number, entropy generation and Bejan number has been presented graphically. In addition, a comparison of the heat transfer rate due to nanofluid and hybrid nanofluid has also been delineated.

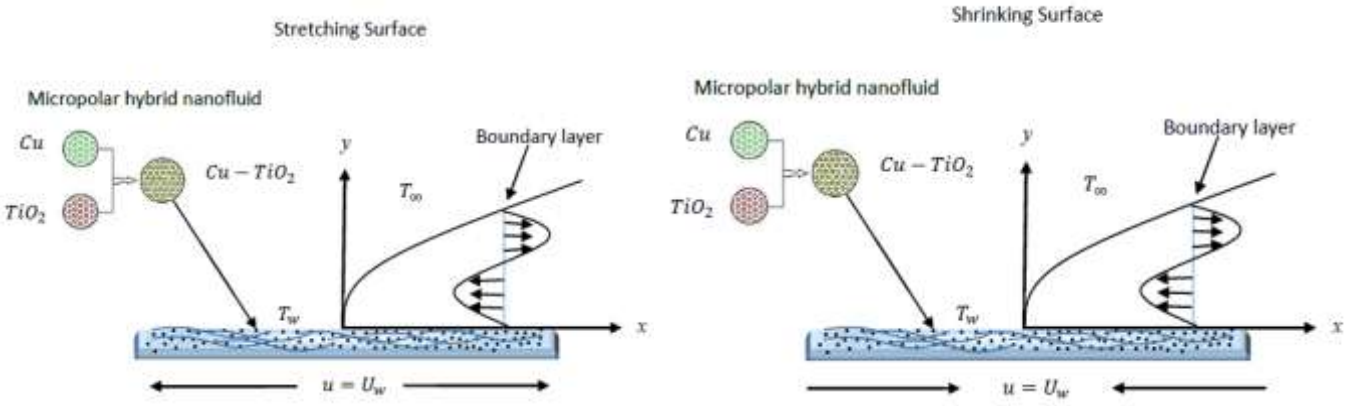

Fig. 5.1. Physical geometry for both stretching and shrinking surface

5.2 Momentum and Temperature description

We have scrutinized two-dimensional magneto-hydrodynamic flow of an incompressible viscous water based hybrid suspension of copper and titanium oxide nanoparticles past an exponentially stretching/shrinking permeable sheet. The stretching/shrinking sheet is assumed to be in the direction of $x-axis$ while $y-axis$ is taken perpendicular to the sheet plus the flow is confined in the region $y>0$ above the sheet as shown in ***Fig. 5.1***. The flow generated is the outcome of stretching or shrinking of the sheet. We have considered Copper Cu and Titanium Oxide TiO_2 nanoparticles dispersed in base fluid water H_2O in this chapter. $Cu/water$ nanofluid is constituted by dispersing nanoparticle volume fraction ϕ_1 in water. Now, to acquire our anticipated results second nanoparticle volume fraction ϕ_2 of TiO_2 nanoparticles is disseminated in $Cu/water$ nanofluid to formulate hybrid nanofluid $Cu-TiO_2/water$. We assume that all the nanoparticles have identical shape and size. Additionally, we also assume that our base fluid plus the nanoparticles happen to be within thermal equilibrium. The thermal and physical characteristics of hybrid nanofluid have been mentioned in ***Table. 3.1***. An external uniform magnetic field having intensity B_0 is assumed in the normal direction of the surface parallel to $y-axis$ and suction S is also perpendicular to the base.

$$\left[\frac{\partial u}{\partial x}+\frac{\partial v}{\partial y}\right]=0, \tag{5.1}$$

$$\left[u\frac{\partial u}{\partial x}+v\frac{\partial u}{\partial y}\right]=\left(\frac{\mu_{hnf}+k}{\rho_{hnf}}\right)\frac{\partial^2 u}{\partial y^2}-\frac{k}{\rho_{hnf}}\left(\frac{\partial N}{\partial y}\right)-\frac{\sigma B_0^2}{\rho_{hnf}}u, \tag{5.2}$$

$$\rho_{hnf}\, j\left[u\frac{\partial N}{\partial x}+v\frac{\partial N}{\partial y}\right]=\chi_{hnf}\frac{\partial^2 N}{\partial y^2}-2kN-k\frac{\partial u}{\partial y}, \tag{5.3}$$

$$u\frac{\partial T}{\partial x}+v\frac{\partial T}{\partial y}=\alpha_{hnf}\left(\frac{\partial^2 T}{\partial y^2}\right)+\left(\frac{\mu_{hnf}+k}{(\rho c_p)_{hnf}}\right)\left(\frac{\partial u}{\partial y}\right)^2-\frac{1}{(\rho c_p)_{hnf}}\frac{\partial q_r}{\partial y}, \tag{5.4}$$

Involving Rosseland's estimation for thermal radiation, the heat flux due to radiation becomes

$$q_r=-\frac{4\sigma^*}{3k^*}\frac{\partial T^4}{\partial y}, \tag{5.5}$$

where σ^* symbolizes the Stefan-Boltzmann constant and k^* represents mean absorption co-efficient. T^4 is a function of temperature defined as

$$T^4=4T_\infty^3 T-3T_\infty^4. \tag{5.6}$$

Using eq. (5.5) in energy equation (5.4) we obtain

$$u\frac{\partial T}{\partial x}+v\frac{\partial T}{\partial y}=\left(\alpha_{hnf}+\frac{1}{(\rho c_p)_{hnf}}\frac{16\sigma^* T_\infty^3}{3k^*}\right)\left(\frac{\partial^2 T}{\partial y^2}\right)+\left(\frac{\mu_{hnf}+k}{(\rho c_p)_{hnf}}\right)\left(\frac{\partial u}{\partial y}\right)^2 \tag{5.7}$$

Boundary Conditions

As seen from ***Fig. 5.1,*** boundary conditions adopt the following form:

$$\left.\begin{aligned} &u=U_w,\ v=V_w,\ T=T_w,\ N=-n\frac{\partial u}{\partial y}, && \text{at} \quad y=0,\\ &u\to 0,\ v\to 0,\ T\to T_\infty,\ N\to 0, && \text{as} \quad y\to\infty. \end{aligned}\right\} \tag{5.8}$$

The surface velocities and temperature are described as follows:

$$U_w = U_0 e^{\frac{x}{L}},\ V_w = -S\sqrt{\frac{V_0 \nu}{2L}} e^{\frac{x}{2L}},\ T_w = T_\infty + T_0 e^{\frac{b_1 x}{2L}}. \tag{5.9}$$

Below are the similarity transformations incorporated in this article:

$$\left.\begin{aligned} &u = U_0 e^{\frac{x}{L}} f'(\eta),\ v = -\left(\frac{\nu U_0}{2L}\right)^{\frac{1}{2}} e^{\frac{x}{2L}} \{ f + \eta f' \}, \\ &N = \sqrt{\frac{U_0^3}{2\nu L}} e^{\left(\frac{3x}{2L}\right)} h(\eta), \\ &T = T_\infty + T_0 e^{\frac{b_1 x}{2L}} \theta(\eta),\ \eta = \left(\frac{U_0}{2\nu L}\right)^{\frac{1}{2}} e^{\frac{x}{2L}} y. \end{aligned}\right\} \tag{5.10}$$

By employing these transformations, momentum, micro-rotational and temperature equations convert to the following equations:

$$\frac{\rho_f}{\rho_{hnf}}\left(\frac{\mu_{hnf}}{\mu_f} + R_1\right) f''' + f f'' - 2 f'^2 + \frac{\rho_f}{\rho_{hnf}} R_1 h' - M f' = 0, \tag{5.11}$$

$$\frac{\rho_f}{\rho_{hnf}}\left(\frac{\mu_{hnf}}{\mu_f} + \frac{R_1}{2}\right) h'' + h' f - 3 h f' - R_1 (2h + f'') = 0, \tag{5.12}$$

$$\left(\frac{k_{hnf}}{k_f} + \frac{4}{3} R\right) \theta'' + \Pr \frac{(\rho c_p)_{hnf}}{(\rho c_p)_f} (f \theta' - b_1 f' \theta) + \Pr Ec (A_2(\phi) + R_1)(f'')^2 = 0. \tag{5.13}$$

Boundary conditions are transformed as follows:

$$\left.\begin{aligned} &f(0)=S,\ f'(0)=\lambda,\\ &\theta(0)=1,\\ &h(0)=-nf''(0), \qquad as\ \eta\to 0,\\ &f'\to 0,\ \theta\to 0,\\ &h\to 0, \qquad as\ \eta\to\infty. \end{aligned}\right\} \tag{5.14}$$

The dimensionless parameters involved in Eq.'s are mathematically represented as:

$$\left.\begin{aligned} &R_1=\frac{k}{\mu},\ M=\frac{2\sigma B_0^2 L}{\rho U_w},\ \Pr=\frac{(\mu c_p)_f}{k_f},\ Ec=\frac{U_0^2 e^{\frac{2x}{L}}}{c_p T_0 e^{\frac{b_1 x}{2L}}},\ \lambda=\frac{U_0}{V_0},\\ &A_2(\phi)=\frac{\mu_{hnf}}{\mu_f}=\frac{1}{(1-\phi_1)^{2.5}(1-\phi_2)^{2.5}}\ \text{and}\ R=\frac{4\sigma^* T_\infty^3}{3k^* k_f}. \end{aligned}\right\} \tag{5.15}$$

The friction co-efficients in addition to the Nusselt number are stated as:

$$C_f=\frac{\tau_{wx}}{\frac{1}{2}\rho_{hnf}U_w^2},\ Nu=\frac{xq_w}{k_f(T_w-T_\infty)}, \tag{5.16}$$

Where τ_{wx}, τ_{wy} represent shear stresses at the boundary and q_w denotes the heat flux, mathematically defined as:

$$\left.\begin{aligned} &\tau_{wx}=(\mu_{hnf}+k)\left(\frac{\partial u}{\partial z}\right)_{y=0}+k(N_2)_{y=0},\\ &q_w=-k_{hnf}\left(\frac{\partial T}{\partial z}\right)_{y=0}. \end{aligned}\right\} \tag{5.17}$$

In non-dimensional form, the skin friction coefficients and Nusselt number are represented as follows:

$$\left.\begin{aligned}\frac{1}{\sqrt{2}}C_f\left(\mathrm{Re}\right)^{\frac{1}{2}} &= \left(\frac{A_2(\phi)+(1-n)R_1}{(1-\phi_2)\left[(1-\phi_1)+\phi_1(\rho_{s_1}/\rho_f)\right]+\phi_2(\rho_{s_2}/\rho_f)}\right)f''(0),\\ \sqrt{2}\,\frac{L}{x}Nu\,\mathrm{Re}^{-\frac{1}{2}} &= -\frac{k_{hnf}}{k_f}\theta'(0).\end{aligned}\right\} \tag{5.18}$$

5.3 Entropy Analysis

This section presents entropy generation analysis for our problem. After employing boundary layer assumptions the dimensional form of volumetric entropy generation is given as

$$E_G = \frac{k_{hnf}}{T_\infty^{\,2}}\left(1+\frac{16\sigma^* T_\infty^{\,3}}{3k^* k_{hnf}}\right)\left(\frac{\partial T}{\partial y}\right)^2 + \left(\frac{\mu_{hnf}+k}{T_\infty}\right)\left(\frac{\partial u}{\partial y}\right)^2 + \left(\frac{\sigma B_0^{\,2}}{T_\infty}\right)u^2, \tag{5.19}$$

Eq. (5.19) signifies the three chief causes of entropy generation. The first expression on the right side represents heat transfer along with effects of radiation. The next term arises owing to fluid friction irreversibility and the third expression appears because of fluid friction owing to magnetic field. The characteristic entropy generation can be expressed as

$$E_0 = \frac{k_{hnf}\left(T-T_\infty\right)}{T_\infty^{\,2}\left(\frac{y}{\eta}\right)^2}, \tag{5.20}$$

So, the dimensionless entropy is given as

$$N_G = \frac{E_G}{E_0} \tag{5.21}$$

After utilizing the similarity transformations we obtain the following form

$$N_G = \left(\frac{k_{hnf}}{k_f} + \frac{4}{3} R \right) \theta'^2 + \frac{Br}{\delta} \left(\frac{\mu_{hnf}}{\mu_f} + R_1 \right) (f'')^2 + 2 \frac{Br}{\delta} M \lambda (f')^2 \tag{5.22}$$

Entropy generation number N_G can be expressed as a sum of the entropy generation caused by thermal irreversibility N_R plus the entropy generation attributed to viscous dissipation N_S and entropy generation due to fluid friction with magnetic field N_M.

$$N_R = \left(\frac{k_{hnf}}{k_f} + \frac{4}{3} R \right) (\theta')^2, \quad N_S = \frac{Br}{\delta} \left(\frac{\mu_{hnf}}{\mu_f} + R_1 \right) (f'')^2, \quad N_M = 2 \frac{Br}{\delta} M \lambda (f')^2. \tag{5.23}$$

Where

$$Br = \Pr Ec, \qquad \delta = \frac{T - T_\infty}{T_\infty} \tag{5.24}$$

For several engineering applications we need the relation of entropy generation because of heat transfer with the overall entropy generation, so to determine this Bejan [52,53] introduced the Bejan number *Be* which describes this ratio

$$Be = \frac{N_R}{N_G} = \frac{\text{The entropy generation due to thermal irreversitbilty}}{\text{Total entropy generation}} \tag{5.25}$$

5.4 Numerical Solution

For solving our problem we used built-in MATLAB programme bvp-4c. We found that dual solutions exist for $f''(0)$ and $\theta'(0)$, which were acquired by choosing altered initial presumptions for $f''(0)$ and $\theta'(0)$ where the boundary conditions were satisfied. To approach the boundary conditions given in equation (5.14) asymptotically we have chosen $\eta_{max} = \eta_\infty = 6$ and a convergence criterion of 10^{-4} is chosen.

5.5 Results and Discussion

To achieve a well-defined physical picture of our analysis, we have illustrated the outcome of significant quantifiable parameters upon skin friction/surface drag force, micro-rotation, Nusselt number, velocity, temperature, entropy generation rate plus the Bejan number. For surface drag and Nusselt number dual solutions appear up to a particular span of λ and S. Such solutions are achieved in hit and trial way, assuming initial presumptions for $f''(0)$ and $\theta'(0)$. We set λ_c and S_c as critical values of λ and S and so when $\lambda = \lambda_c$ and $S = S_c$ a unique solution exists, for $\lambda > \lambda_c$ and $S > S_c$ dual solutions arise while there exists no solution for $\lambda < \lambda_c$ and $S < S_c$. We perceive that only first solution obtained is stable and hence physically applicable(see refs. [68-70]).

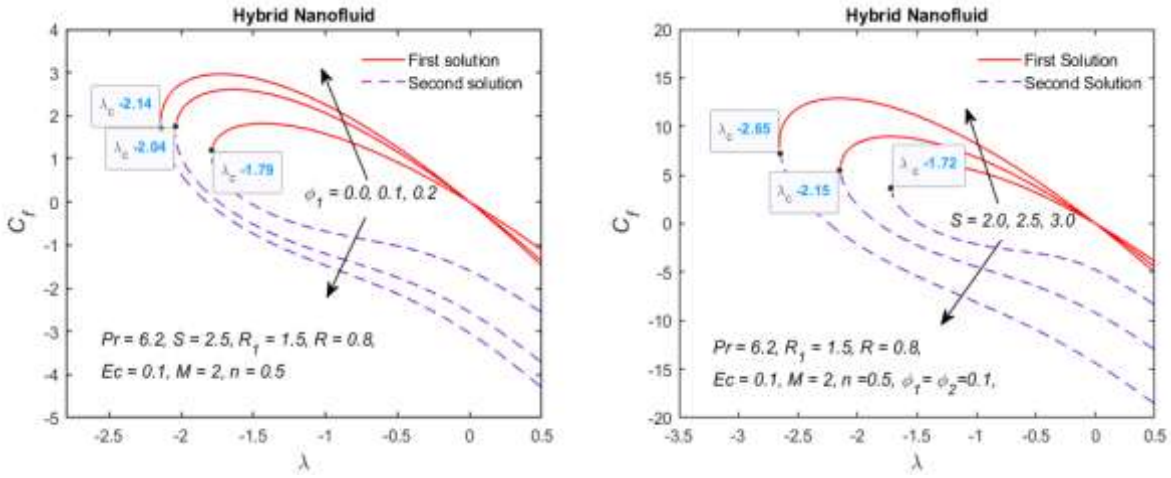

(a) **(b)**

Fig. 5.2. Impact of **(a)** ϕ_1 and **(b)** S on skin friction co-efficient against λ.

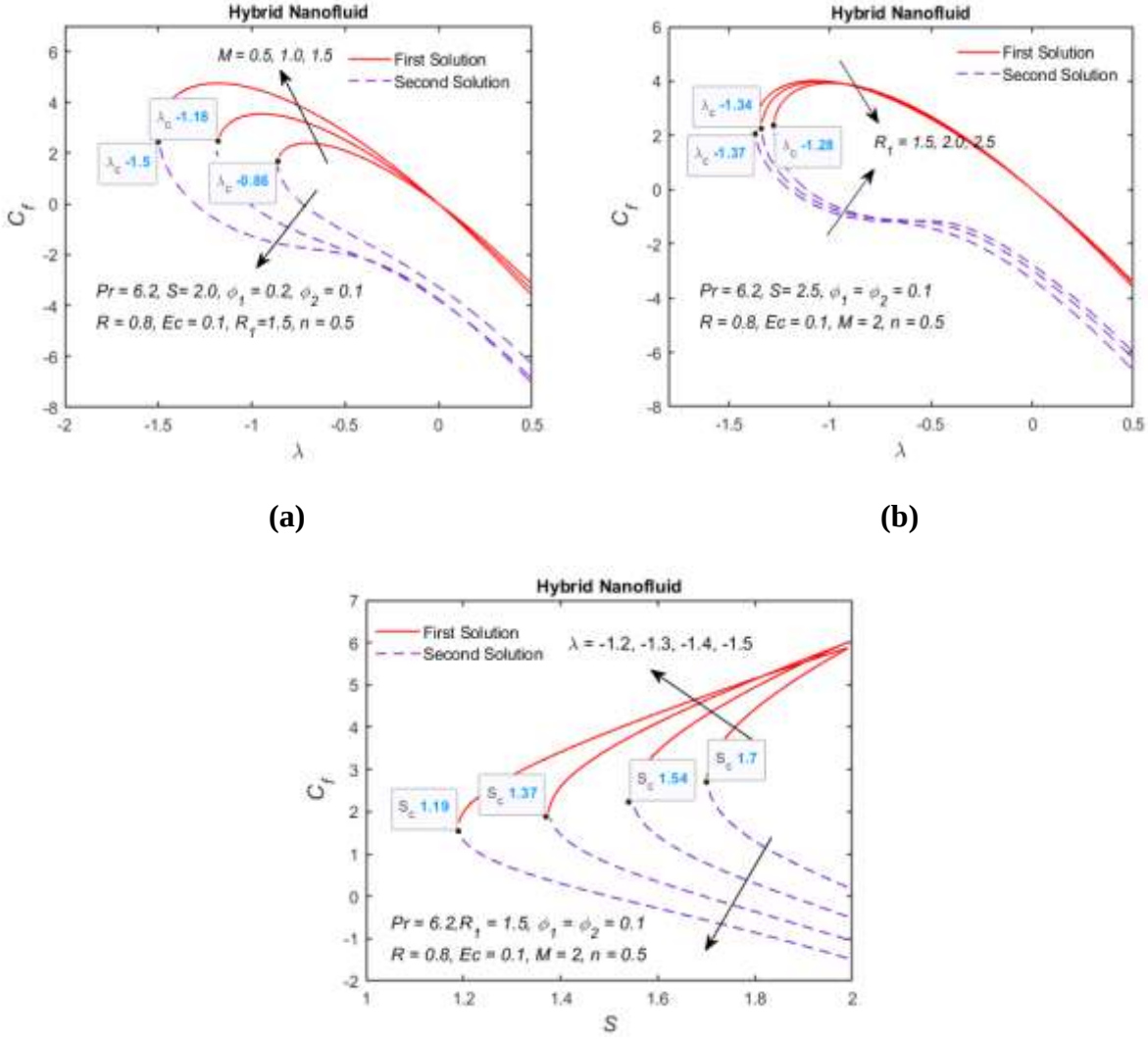

Fig. 5.3. Impact of **(a)** M, **(b)** R_1 on skin friction against λ and influence of **(c)** λ on C_f against S.

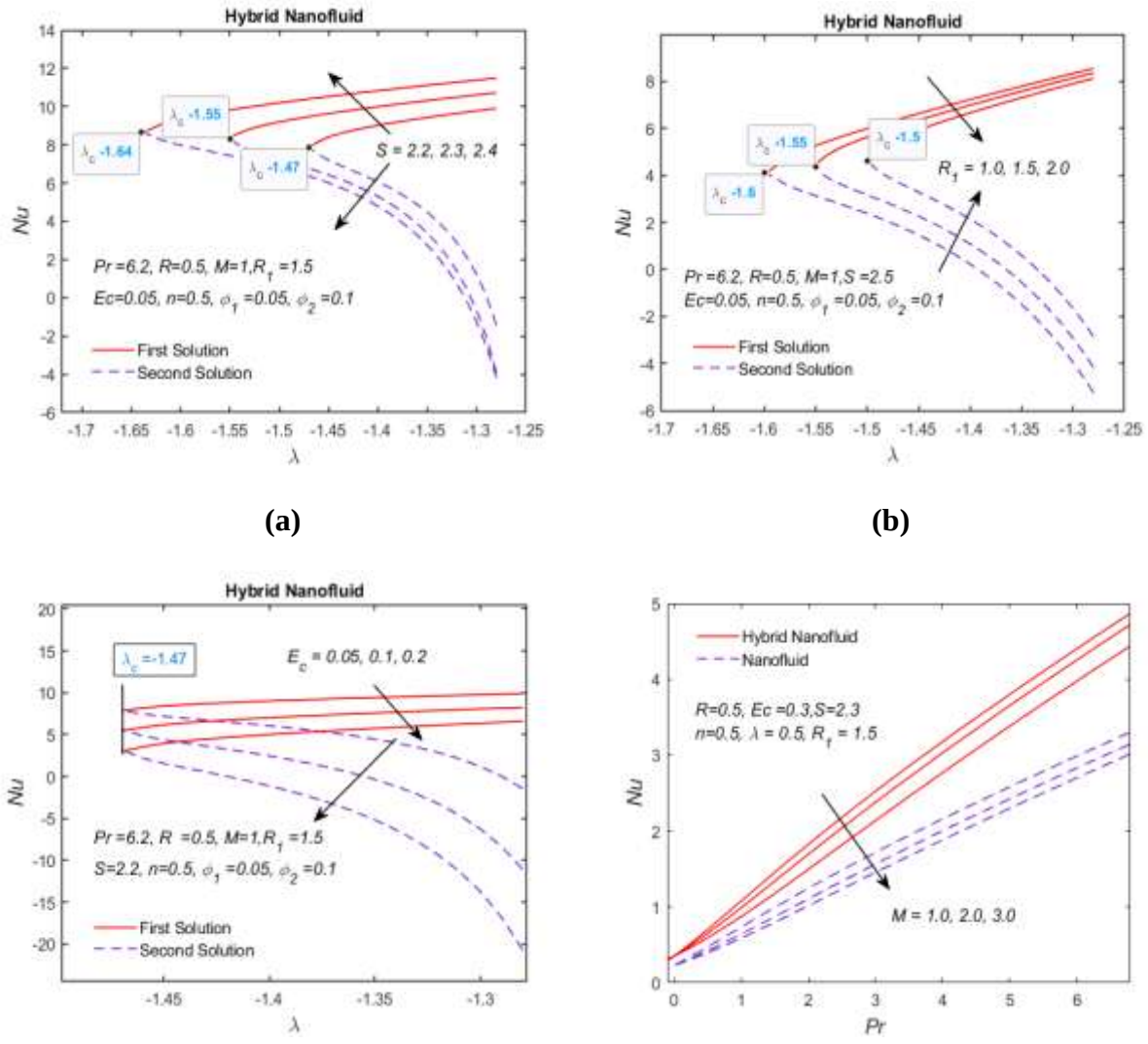

Fig. 5.4. Results of modifications in **(a)** S, **(b)** R_1, **(c)** Ec on Nusselt number against λ and **(d)** impact of M on Nu against Pr for both hybrid and mono nanofluid.

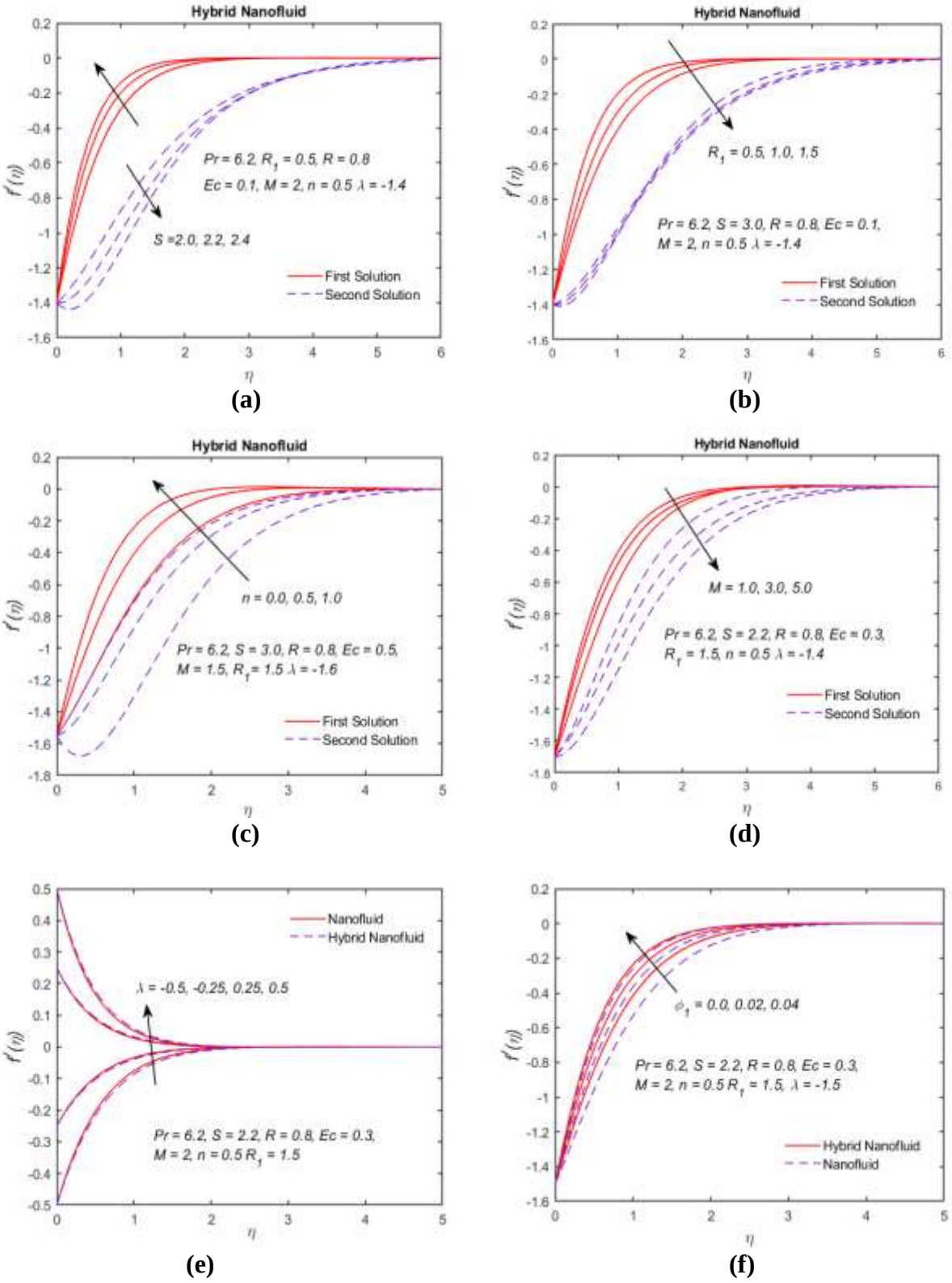

Fig. 5.5. Influence of **(a)** S, **(b)** R_1, **(c)** n and **(d)** $\boldsymbol{M}$ on velocity while **(e)** and **(f)** portray the impact of λ and ϕ_1 on $f'(\eta)$

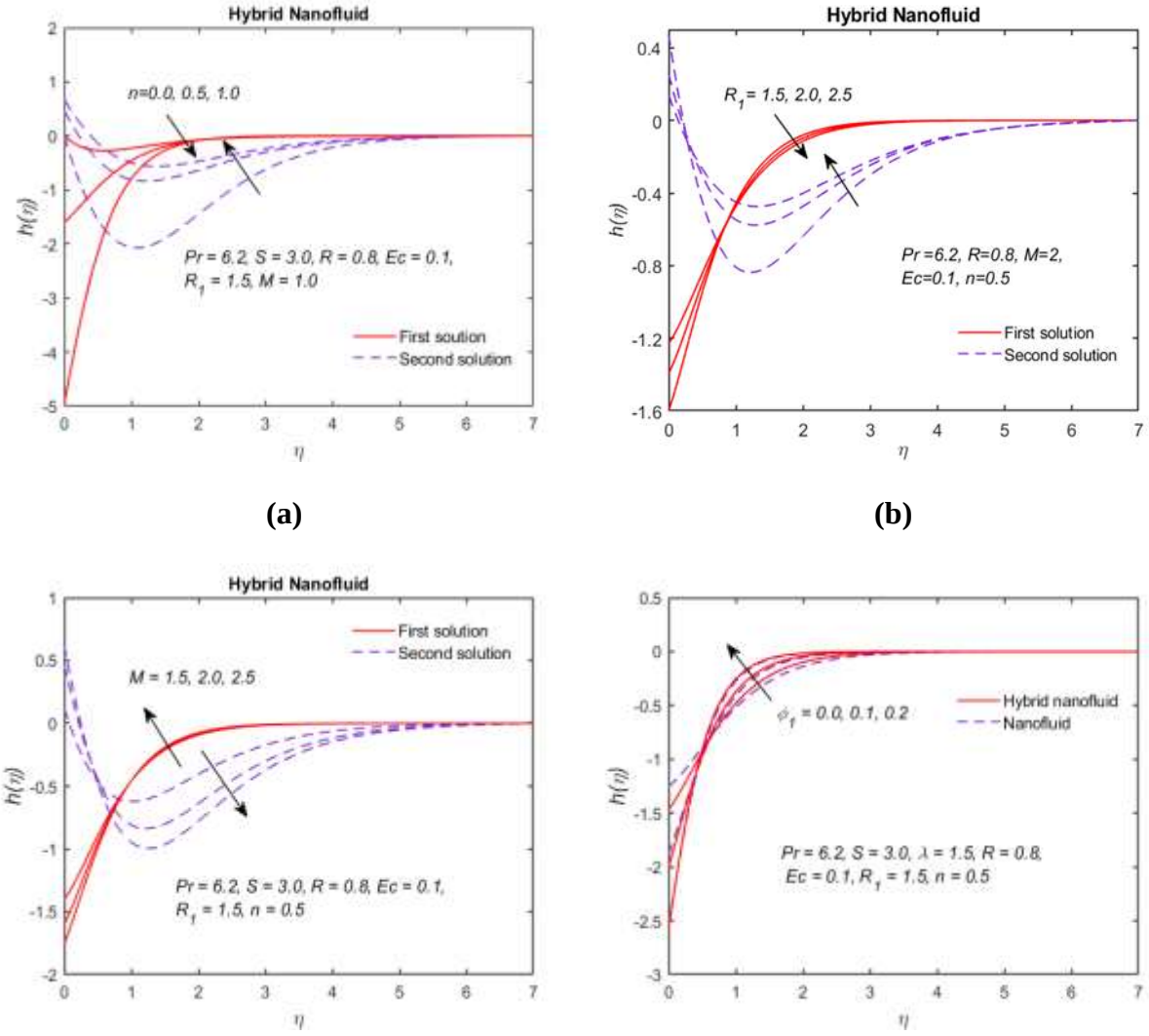

Fig. 5.6. Impact of **(a)** n , **(b)** R_1 , **(c)** M and **(d)** ϕ_1 on micro-rotation profile.

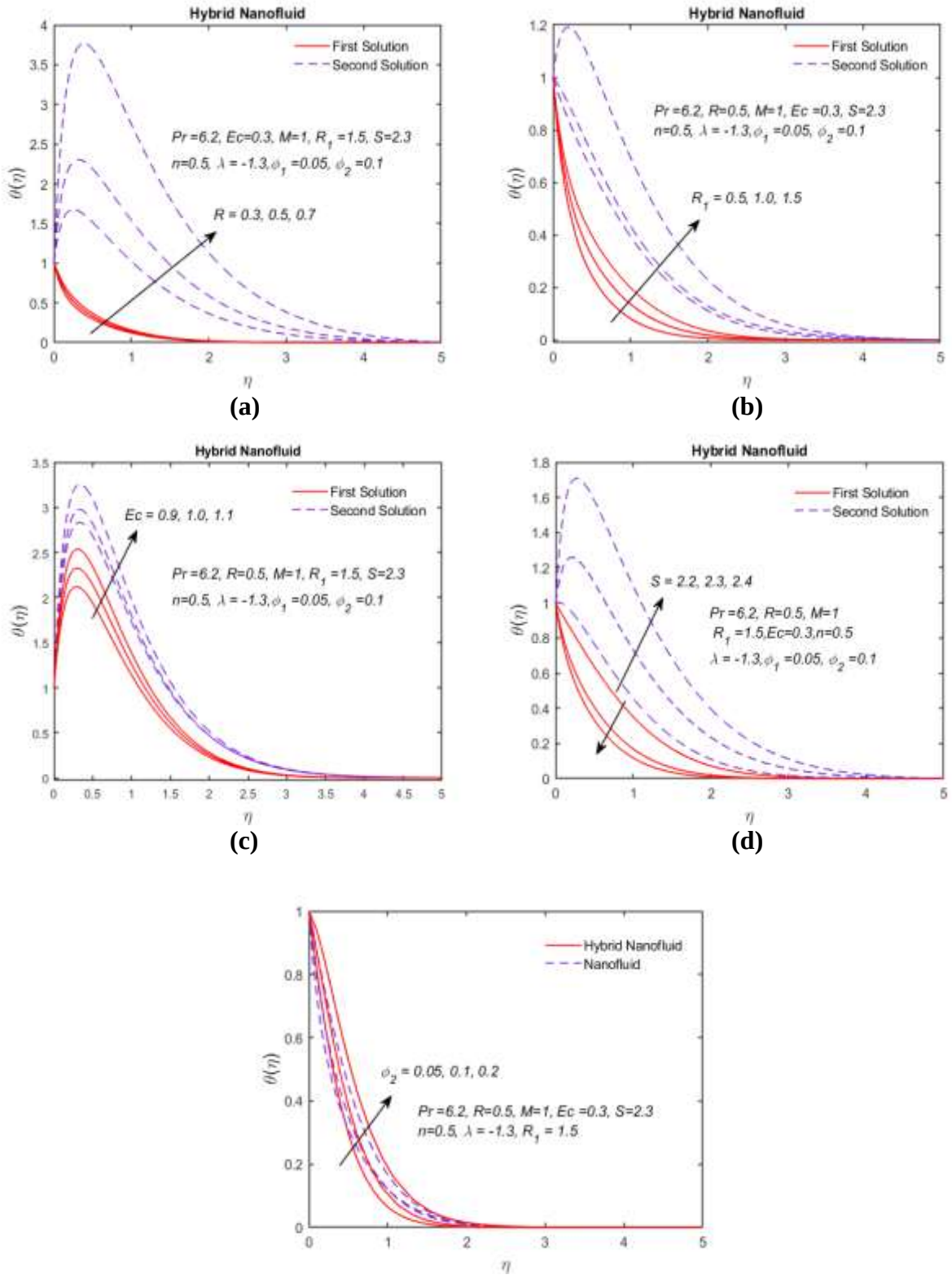

Fig. 5.7. Variations in thermal field due to **(a)** R , **(b)** R_1 , **(c)** Ec, **(d)** S and **(e)** ϕ_2 for the case of hybrid and simple nanofluid.

Results of Entropy analysis:

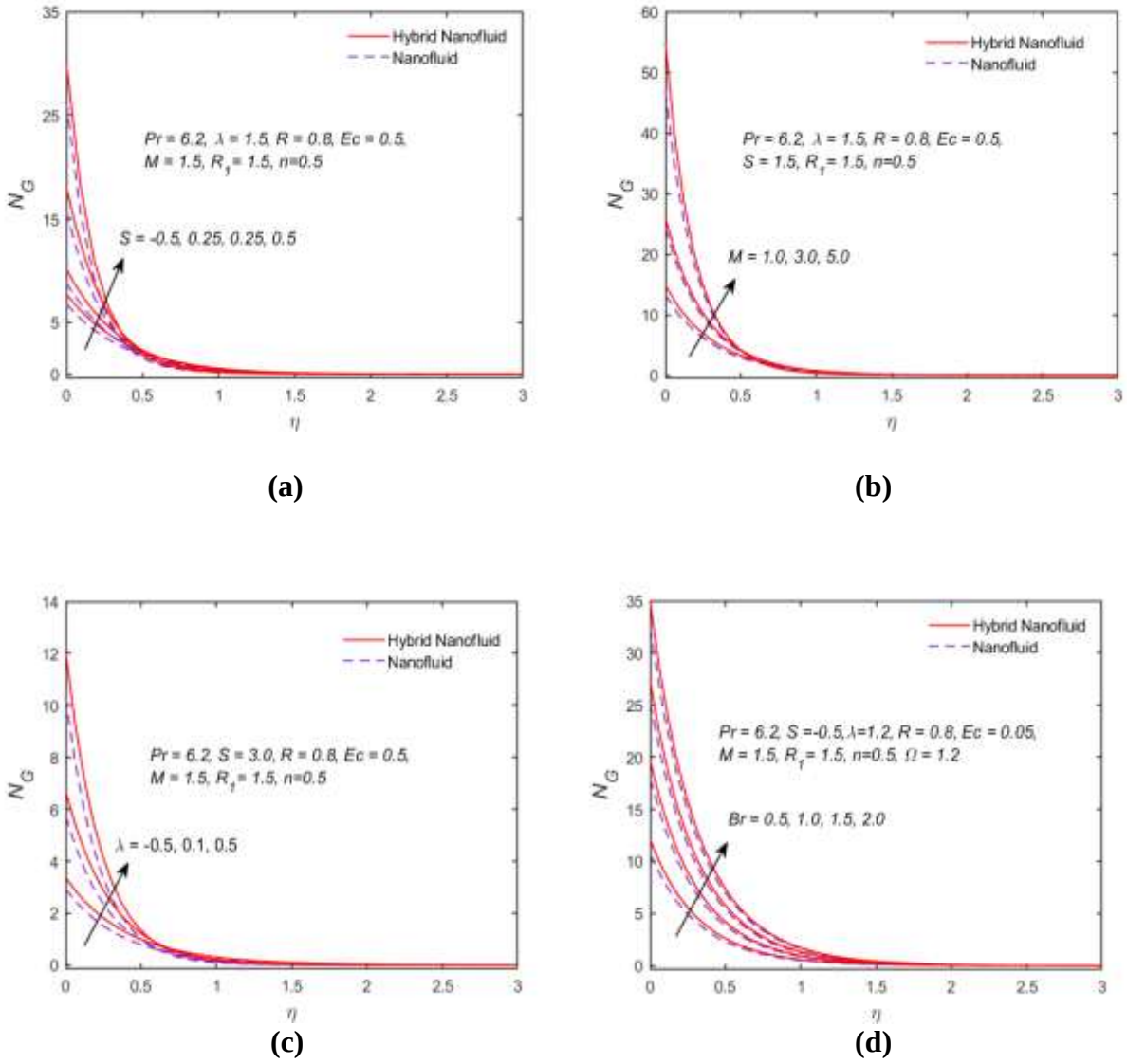

Fig. 5.8. Impact of **(a)** S , **(b)** M , **(c)** λ and **(d)** Br on total entropy generation for both the hybrid and simple nanofluid case.

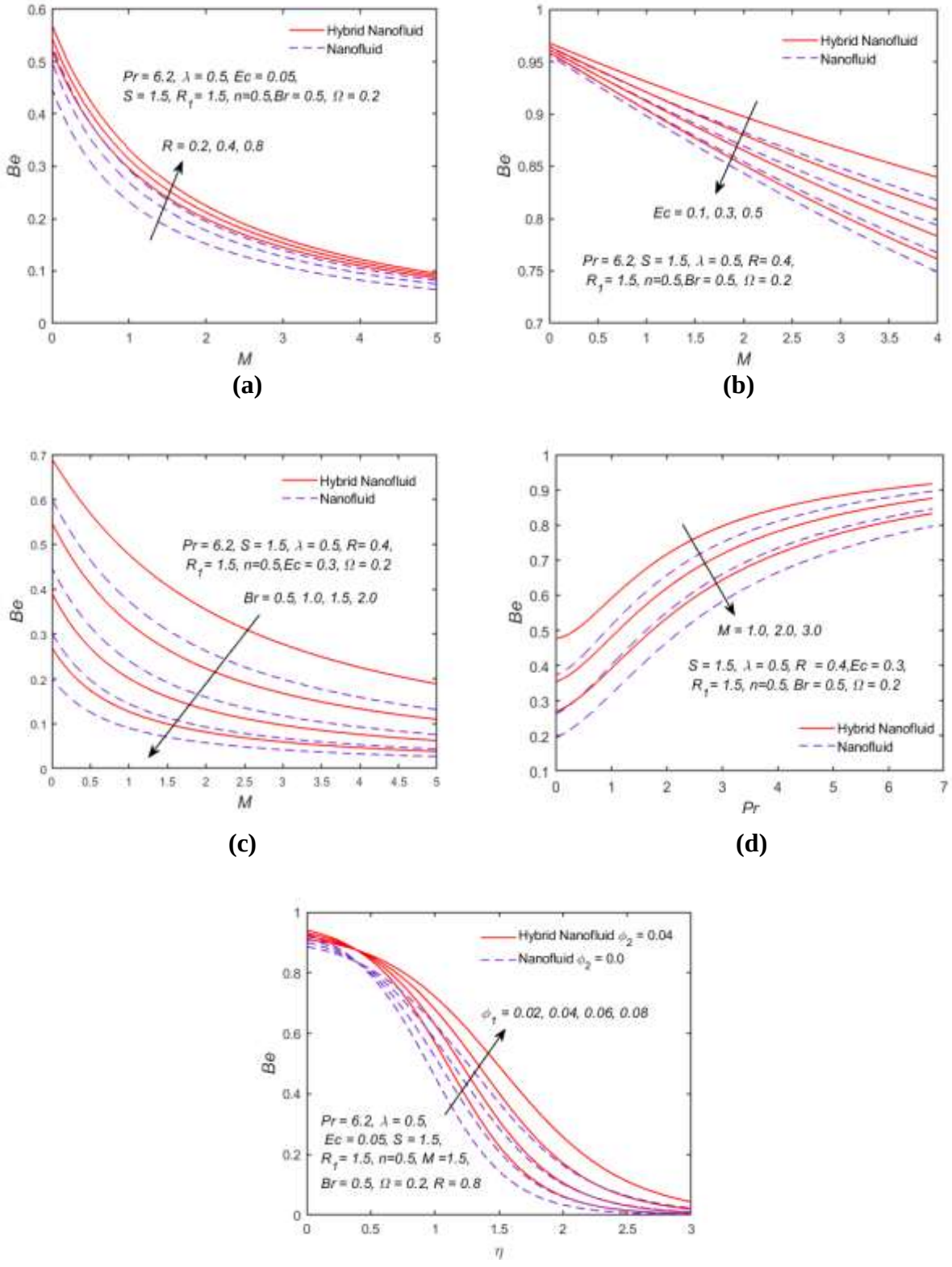

Fig. 5.9. Impact of **(a)** R , **(b)** Ec, **(c)** Br on Bejan number against M and influence of **(d)** M , versus Pr and **(e)** ϕ_1 for the case of hybrid and simple nanofluid.

Fig. 5.2 displays the deviation in skin friction number with variation of S and nanoparticle's volume ϕ_1 against the stretching ratio parameter λ and when $\mathrm{Pr} = 6.2, \mathrm{R} = 0.8, R_1 = 5$. ***Fig. 5.2(a)*** depicts behavior of C_f against ϕ_1 where dual solutions exist for $\lambda_c < \lambda < 0.5$, where the critical values of λ are $\lambda_c = -1.79, -2.04, -2.14$. From ***Fig. 5.2(a)*** we can clearly observe that both the segments of solution present enhancing behavior for increasing values of ϕ_1. Similarly, ***Fig. 5.2(b)*** shows the same behavior. As we upsurge the values of suction parameter S the critical values are observed at $\lambda_c = -1.72, -2.15, -2.65$ with increasing behavior of both solutions.

In ***Fig. 5.3(a)***, two solutions are being formulated for surface friction number corresponding to greater values of M. Furthermore, the critical values of λ, when the solution is being distributed into two segments (first and second solution), are $\lambda_c = -0.86, -1.18, -1.5$. It is revealed from ***Fig. 5.3(a)***, for rising values of M, the skin friction number also rises for both segments whereas all the other parameters remain constant. ***Fig. 5.3(b)*** is sketched to see the impact of R_1 on skin friction number against differing values of R_1. It is witnessed that by increasing values of R_1, the skin friction number decreases. Critical values of λ in ***Fig. 5.3(b)*** are $\lambda_c = -1.28, -1.34, -1.37$ when $n = 0.5, M = 2, S = 2.5$. ***Fig. 5.3(c)*** is drawn to see the variation in surface drag force or skin friction number with varying values of λ against S .From ***Fig .5.3(c)*** it is viewed that escalating values of λ boosts the skin friction factor for both first and second solutions. Critical values of S in ***Fig. 5.3(c)*** are $S_c = 1.7, 1.54, 1.37, 1.19$. Here solution exists for $S_c > S$.

Fig. 5.4(a) exhibits the impact of S upon Nusselt number. For the primary and secondary solution, it is understandable from graphs that the Nusselt number enhances as S increases. Dual solutions exist for $\lambda = \lambda_c = -1.47, -1.55, -1.64$. It can be observed that for growing values of S, critical values decrease. ***Fig. 5.4(b)*** demonstrates reverse behavior as compared to ***Fig. 5.4(a)***. By intensifying the values of R_1, Nusselt number reduces. Here critical values of λ occur at $\lambda_c = -1.5, -1.55, -1.6$. ***Fig. 5.4(c)*** is designed to see the influence of Ec on Nusselt number. Enhancing values of Ec subsides the Nusselt number and the critical value of $\lambda = \lambda_c = -1.47$ is same for all the values of Ec. Similar pattern is observed from ***Fig. 5.4(d)***. By amplifying values of M, the Nusselt number decreases.

In ***Fig. 5.5(a)*** dual velocity distributions are displayed for S. As a result, it is noted that with increased suction, there occurs more distance between these two solutions. This plot expresses that

uplift in fluid velocity is signified with higher values of S in the matter of primary solution, while there is decrease in fluid velocity decreases due to enhancement of suction parameter for the secondary solution. In addition, a close observation of ***Fig. 5.5(a)*** indicates that enhancement of S thickens the boundary layer as well. The influence of R_1 on velocity profile is exhibited in ***Fig. 5.5(b).*** To trace the influence of R_1 upon the boundary layer flow, the values of other parameters are kept constant and the value of R_1 is varied, also keeping into consideration both primary and secondary solutions. We learnt from this figure that intensifying the values of the R_1 decelerates the velocity profile for both the first and second solution and also the boundary later thickness decreases. For a comprehensive analysis we have also incorporated graphs of the velocity field for changing values of the boundary parameter n inspecting both the solutions. From ***Fig. 5.5(c)***, we see that by amplifying the values of n a rise in velocity profile occurs. ***Fig. 5.5(d)*** is designed to depict the impact of M on velocity, it is adequate to notice that velocity has a reverse trend with elevating M when compared with n. ***Fig. 5.5(e)*** and ***5.5(f)*** are plotted to observe the behavior of λ and ϕ_1 on velocity profile. Increasing values of λ and ϕ_1 increases the velocity profile and diminishes the boundary layer thickness.

Fig. 5.6(a) displays the influence of the boundary parameter n on micro-rotation profile. When we enhance the values of n a decrease in $h(\eta)$ is viewed for first solution while second solution increases. Similar behavior is seen in ***Fig. 5.6(b)***, where impact of R_1 is scrutinized over $h(\eta)$, while a contradictory behavior can be perceived from ***Fig. 5.6(c)***, where effect of M on $h(\eta)$ is analyzed. Through ***Fig. 5.6(d)*** the impact of ϕ_1 upon micro-rotation profile can be depicted. Increasing values of ϕ_1 increases the micro-rotation profile for both hybrid nanofluid and mono nanofluid. Whereas a fluctuating behavior is observed for $\eta < 1$ as some other physical parameter becomes dominant closer to the surface.

Fig. 5.7(a) and ***5.7(b)*** show detailed features of thermal boundary layer for varying the values of R and R_1. The fact disclosed is that by uprising values of R and R_1 results in higher degree of temperature. The thickness of boundary layer upsurges close to the wall and reduces far away from the wall. ***Fig. 5.7(c)*** and ***5.7(d)*** are drawn to see the behavior of Ec and S on temperature distribution. Increasing values of Ec increases both the first and second solution. On the other hand increasing values of S increases the first solution but decreases the second solution. In ***Fig. 5.7(e)*** temperature profiles are shown for mono nanofluid and hybrid nanofluid along with varying values of ϕ_2. Consequently, we observed that in case of high values of ϕ_2, temperature profile for fluids

present the same increasing behavior where the hybrid nanofluid gives a better temperature profile as compared to simple nanofluid.

Influence of various parameters on total entropy generation N_G and Bejan number Be are illustrated graphically through ***Figs. 5.8-5.9. Fig. 5.8(a)*** and ***5.8(b)*** are plotted to see the impact of S and M on total entropy generation respectively. While ***Fig. 5.8(c)*** and ***5.8(d)*** are sketched to study the effect of stretching ratio parameter and Brinkman number upon N_G. The total entropy generation increases for increase in S, M, λ and Br. It is observed that higher values of all these parameters produce higher entropy generation near the surface.

In ***Fig. 5.9(a)*** the impact of radiation parameter on the Bejan number is exhibited. For greater values of R the Bejan number increases since physically for higher values of R more energy to the system is supplied hence causing greater entropy generation due to heat transfer. ***Fig. 5.9(b)*** and ***5.9(c)*** illustrate the behavior of Bejan number for changing values of Ec and Br against magnetic parameter M. Similar behavior is witnessed in both figures the Bejan number decreases for increase in both parameters. ***Fig. 5.9(d)*** is drawn to scrutinize Be for magnetic parameter against Prandtl number. Be decreases as we increase values of M since by increasing M the entropy due to friction of fluid increases, increasing the overall entropy in comparison with the entropy caused by heat transfer. ***Fig. 5.9(e)*** displays the influence of ϕ_1 on Be for simple nanofluid plus hybrid nanofluid. As we increase the nanoparticle concentration, the entropy caused by heat transfer buildsup and consequentially the Bejan number.

5.6 Concluding Remarks

We employed a computational simulation to inspect the flow behavior of the micropolar hybrid nanofluid flowing due to exponential stretching/shrinking of surface. Impact of magnetic field, viscous dissipation and thermal radiation were also examined. The results were developed for dual solutions. And we reached upon the following conclusions from the current chapter.

- The surface friction co-efficient increases with uplifting the nanoparticle volume portion, suction and magnetic parameter.
- Nusselt number shows a boost due to suction parameter while declines with enhancement in micro-rotation and magnetic parameter and Eckert number.
- The appearance of micro-rotation increases the velocity, temperature and entropy generation.
- As magnetic field strength increases velocity, micro-rotation of the particles decreases and temperature, entropy generation increases.
- Entropy generation and Bejan number enhance in the presence of Br.

Chapter 6

6. Unsteady heat and mass transfer analysis of MHD micropolar dusty nanofluid flow

6.1 Introduction

In this segment we have represented the analytical solution of the unsteady boundary layer flow and heat transfer of nanofluid with dust particles suspended in it. The magnetic field is transverse to the plate. Considering the influence of heat generation/absorption, viscous dissipation and thermal radiation, PDE's are modelled. Then they are changed to ODE's by employing similarity transformations for the following two cases of boundary conditions (i) VEST (Variable exponential order surface temperature) (ii) VEHF (Variable exponential order heat flux) and then the series solutions are calculated using OHAM. At the end, the influence on the velocity, temperature and concentration profiles of various important physical parameters are explored in detail with graphical illustrations and tables.

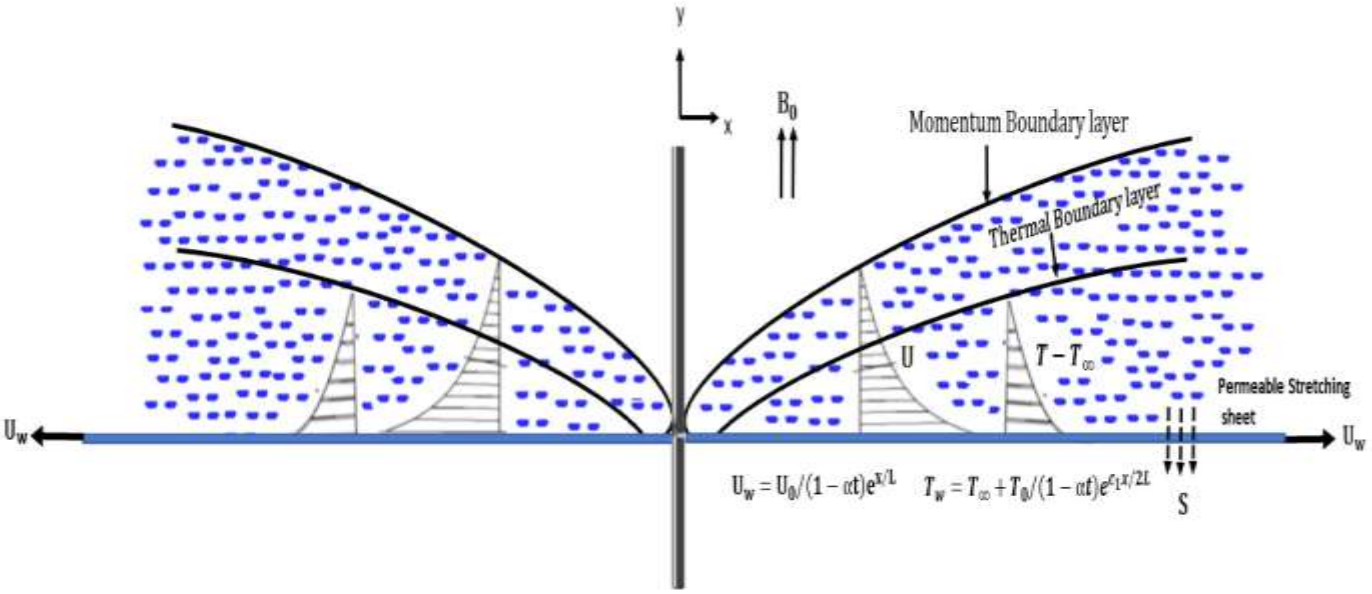

Fig. 6.1. Physical geometry.

6.2 Problem description

The flow field regime, heat transfer in addition to mass transfer analysis for the two-dimensional unsteady boundary layer flow of dusty micropolar nanofluid induced by an exponentially stretched surface in the existence of viscous dissipation, magnetic field, heat generation/absorption and thermal radiation are considered. Coordinate system is adopted such that the stretching sheet is assumed to be along $x-$ axis while $y-$ axis is normal to the sheet and the flow is restrained in region $y>0$ above the sheet as displayed in ***Fig. 6.1.*** Two equivalent but opposite forces are simultaneously employed along $x-$ axis to stretch the sheet exponentially with the velocity $U_w(x,t)=\frac{U_o}{(1-\alpha t)}e^{\frac{x}{L}}$ also prompting the flow of fluid. An external uniform magnetic field having intensity B_0 is directed normal to surface parallel to y$-$ axis and suction S is also normal to sheet.

Under the aforementioned assumptions and utilizing the standard boundary-layer hypothesis, the governing mathematical equations for conservation of mass, momentum and angular momentum for fluid phase and particles phase can be inscribed as

$$\frac{\partial u}{\partial x}+\frac{\partial v}{\partial y}=0, \tag{6.1}$$

$$\frac{\partial u}{\partial t}+u\frac{\partial u}{\partial x}+v\frac{\partial u}{\partial y}=\left(\nu+\frac{k}{\rho}\right)\frac{\partial^2 u}{\partial y^2}-\frac{\sigma}{\rho}B_0^2u+KN^*\left(u_p-u\right)+\frac{k}{\rho}\frac{\partial N_1}{\partial y}, \tag{6.2}$$

$$\frac{\partial N_1}{\partial t}+u\frac{\partial N_1}{\partial x}+v\frac{\partial N_1}{\partial y}=\frac{\chi}{\rho j}\frac{\partial^2 N_1}{\partial y^2}-\frac{k}{\rho j}\left(2N_1+\frac{\partial u}{\partial y}\right) \tag{6.3}$$

$$\frac{\partial u_p}{\partial x} + \frac{\partial v_p}{\partial y} = 0, \tag{6.4}$$

$$\frac{\partial u_p}{\partial t} + u_p \frac{\partial u_p}{\partial x} + v_p \frac{\partial u_p}{\partial y} = \frac{K}{m}\left(u - u_p\right). \tag{6.5}$$

The boundary conditions are

$$\left.\begin{aligned} &u = U_w(x,t),\ v = -V_w(x,t),\ N_1 = -n\frac{\partial u}{\partial y} \text{ at } y = 0,\\ &u \to 0,\ u_p \to 0,\ v_p \to v,\ N_1 \to 0 \text{ as } y \to \infty. \end{aligned}\right\} \tag{6.6}$$

where $U_w(x,t) = \frac{U_o}{(1-\alpha t)} e^{\frac{x}{L}}$ is the velocity of the sheet and $V_w(x,t) = -S\sqrt{\frac{U_o \nu}{2L(1-\alpha t)}}\, e^{\frac{x}{2L}}$ is the suction velocity.

Similarity transformations are defined as

$$\left.\begin{aligned} &u = \frac{U_o}{(1-\alpha t)} e^{\frac{x}{L}} f'(\eta),\ v = -\sqrt{\frac{U_o \nu}{2L(1-\alpha t)}}\, e^{\frac{x}{2L}}\left[f(\eta) + \eta f'(\eta)\right],\\ &u_p = \frac{U_o}{(1-\alpha t)} e^{\frac{x}{L}} F'(\eta),\ v_p = -\sqrt{\frac{U_o \nu}{2L(1-\alpha t)}}\, e^{\frac{x}{2L}}\left[F(\eta) + \eta F'(\eta)\right],\\ &N_1 = \sqrt{\frac{(U_o)^3}{2\nu L(1-\alpha t)^3}}\, e^{\frac{x}{2L}} h_1(\eta),\ \eta = \sqrt{\frac{U_o}{2\nu L(1-\alpha t)}}\, e^{\frac{x}{2L}} y. \end{aligned}\right\} \tag{6.7}$$

By use of eq. (6.7), equations of continuity (6.1 and 6.4) are equivalently satisfied while eqs. (6.2, 6.3 and 6.5) take the following form

$$\begin{aligned}(1+R_1)\,f'''(\eta)+f(\eta)\,f''(\eta)-2\left(f'(\eta)\right)^2+R_1 h_1'(\eta)+2l\beta\left[F'(\eta)-f'(\eta)\right]\\ -A\left[2f'(\eta)+\eta f''(\eta)\right]-M\ f'=0,\end{aligned} \tag{6.8}$$

$$\begin{aligned}\left(1+\frac{R_1}{2}\right)h_1''(\eta)-R_1\left[2h_1(\eta)+f''(\eta)\right]-3h_1(\eta)\,f'(\eta)+h_1'(\eta)\,f(\eta)\\ -A\left[3h_1(\eta)+\eta h_1'(\eta)\right]=0,\end{aligned} \tag{6.9}$$

$$F(\eta)F''(\eta)-2\left(F'(\eta)\right)^2+2\beta\left[f'(\eta)-F'(\eta)\right]-A\left[\eta F''(\eta)+2F'(\eta)\right]=0, \tag{6.10}$$

Employing similarity transformations on boundary conditions presented in eq.(6.6), we acquire

$$\left.\begin{aligned}&f'(\eta)=1,\ f(\eta)=S,\ h(\eta)=-nf''(\eta), && as\ \eta\to 0,\\ &f'(\eta)=0,\ F'(\eta)=0,\ F(\eta)=f(\eta)+\eta f'(\eta)-\eta F'(\eta),\ h(\eta)=0, && as\ \eta\to\infty.\end{aligned}\right\} \tag{6.11}$$

The expression for the skin friction coefficient is

$$C_f=\frac{\tau_w}{\rho U_w^2}, \tag{6.12}$$

where the surface friction τ_w is given by,

$$\tau_w=(\mu+k)\left[\frac{\partial u}{\partial y}+kN\right]_{y=0}, \tag{6.13}$$

Involving the non-dimensional factors we have,

$$\frac{1}{\sqrt{2}}(\mathrm{Re})^{\frac{1}{2}} C_f = \left[1 + (1-n) R_1\right] f''(0). \tag{6.14}$$

6.3 Heat and Mass Transfer Analysis for Nanofluid

Energy equations for fluid phase and dust particles are

$$\rho c_p \left(\frac{\partial T}{\partial t} + u \frac{\partial T}{\partial x} + v \frac{\partial T}{\partial y} \right) = k_f \frac{\partial^2 T}{\partial y^2} + \frac{N^* c_p}{\tau_T}(T_p - T) + \frac{N^*}{\tau_v}(u_p - u)^2 +$$
$$(\mu + k)\left(\frac{\partial u}{\partial y} \right)^2 - \frac{\partial q_r}{\partial y} + Q(T - T_\infty) + (\rho c_p)_p \left(D_B \frac{\partial C}{\partial y}\frac{\partial T}{\partial y} + \frac{D_T}{T_\infty}\left(\frac{\partial T}{\partial y} \right)^2 \right), \tag{6.15}$$

$$N^* c_m \left(\frac{\partial T_p}{\partial t} + u_p \frac{\partial T_p}{\partial x} + v_p \frac{\partial T_p}{\partial y} \right) = -\frac{N^* c_p}{\tau_T}(T_p - T). \tag{6.16}$$

Involving Rosseland's estimation as in chapter 5 we have

$$q_r = -\frac{4\sigma^*}{3k^*}\frac{\partial T^4}{\partial y}, \tag{6.17}$$

where

$$T^4 = 4T_\infty^3 T - 3T_\infty^4. \tag{6.18}$$

Using eq.(6.17) in energy equation (6.15), we obtain

$$\rho c_p \left(\frac{\partial T}{\partial t} + u \frac{\partial T}{\partial x} + v \frac{\partial T}{\partial y} \right) = \left(k_f + \frac{16\sigma^* T_\infty^3}{3k^*} \right) \frac{\partial^2 T}{\partial y^2} + \frac{N^* c_p}{\tau_T}(T_p - T) + \frac{N^*}{\tau_v}(u_p - u)^2$$
$$+ (\mu + k)\left(\frac{\partial u}{\partial y} \right)^2 + Q(T - T_\infty) + (\rho c_p)_p \left(D_B \frac{\partial C}{\partial y}\frac{\partial T}{\partial y} + \frac{D_T}{T_\infty}\left(\frac{\partial T}{\partial y} \right)^2 \right), \tag{6.19}$$

Concentration equations of fluid phase and dust particles are

$$\frac{\partial C}{\partial t} + u\frac{\partial C}{\partial x} + v\frac{\partial C}{\partial y} = D_B\frac{\partial^2 C}{\partial y^2} + \frac{D_T}{T_\infty}\left(\frac{\partial^2 T}{\partial y^2}\right), \tag{6.20}$$

$$\frac{\partial C_p}{\partial t} + u_p\frac{\partial C_p}{\partial x} + v_p\frac{\partial C_p}{\partial y} = D\frac{\partial^2 C_p}{\partial y^2}, \tag{6.21}$$

where D signifies the co-efficient of mass diffusivity C is the concentration of fluid and C_p denotes concentration of dust particles.

We have discussed the heat and mass transport phenomenon for two different heating procedures, i.e.,

1. VEST (Variable exponential order surface temperature and surface concentration).

2. VEHF (Variable exponential order heat and mass flux).

6.3.1 Case 1: VEST (Variable exponential order surface temperature and concentration):

In this case the boundary conditions employed, are defined as

$$\begin{aligned} &T = T_w(x,t) \text{ at } y = 0,\\ &T \to T_\infty,\ T_p \to T_\infty \text{ as } y \to \infty,\\ &C = C_w(x,t) \text{ at } y = 0,\\ &C \to C_\infty,\ C_p \to C_\infty \text{ as } y \to \infty, \end{aligned} \tag{6.22}$$

Where $T_w = T_\infty + \frac{T_0}{(1-\alpha t)^2} e^{\frac{b_1 x}{2L}}$ and $C_w = C_\infty + \frac{C_0}{(1-\alpha t)^2} e^{\frac{c_1 x}{2L}}$ are the temperature distribution and concentration distribution respectively in the stretching surface. The dimensionless factors for the fluid temperature $\theta(\eta)$ and concentration $\phi(\eta)$ and dust particles temperature $\theta_p(\eta)$ and concentration $\phi_p(\eta)$ are defined as

$$\begin{aligned} \theta(\eta) &= \frac{T - T_\infty}{T_w - T_\infty}, \quad \theta_p(\eta) = \frac{T_p - T_\infty}{T_w - T_\infty}, \\ \phi(\eta) &= \frac{C - C_\infty}{C_w - C_\infty}, \quad \phi_p(\eta) = \frac{C_p - C_\infty}{C_w - C_\infty}, \end{aligned} \tag{6.23}$$

where $T - T_\infty = \frac{T_0}{(1-\alpha t)^2} e^{\frac{b_1 x}{2L}} \theta(\eta)$ and $C - C_\infty = \frac{C_0}{(1-\alpha t)^2} e^{\frac{c_1 x}{2L}} \phi(\eta)$. Using the eq. (6.23) into eq.'s (6.16, 6.19, 6.20, 6.21 and 6.22) one can achieve below mentioned equations

$$\begin{aligned} &\left(1 + \frac{4R}{3}\right)\theta''(\eta) + \Pr\left[f(\eta)\theta'(\eta) - b_1 f'(\eta)\theta(\eta)\right] + 2\frac{N^*}{\rho}\beta_T \Pr\left[\theta_p(\eta) - \theta(\eta)\right] \\ &+ \Pr Ec(1+R_1)\left[f'(\eta)\right]^2 - A\Pr\left[\eta\theta'(\eta) + 4\theta(\eta)\right] + 2\frac{N^*}{\rho}\beta \Pr Ec\left[F'(\eta) - f'(\eta)\right]^2 \\ &+ 2\lambda^* \Pr\theta(\eta) + \Pr\left[N_t\theta'^2 + N_b\phi'\theta'\right] = 0, \end{aligned} \tag{6.24}$$

$$b_1 F'(\eta)\theta_p(\eta) - F(\eta)\theta_p'(\eta) + 2\gamma\beta_T\left[\theta_p(\eta) - \theta(\eta)\right] + A\left[\eta\theta_p'(\eta) + 4\theta_p(\eta)\right] = 0, \tag{6.25}$$

$$\phi'' + \frac{N_t}{N_b}\theta'' + Sc\left[f\phi' - c_1 f'\phi\right] - ASc\left[4\phi + \eta\phi'\right] = 0 \tag{6.26}$$

$$\phi_p'' + Sc\left[F\phi_p' - c_1 F'\phi_p\right] - ASc\left[4\phi_p + \eta\phi_p'\right] = 0 \tag{6.27}$$

Subsequent thermal and concentration boundary conditions become

$$\begin{aligned} &\theta(\eta) = 1 \text{ at } \eta = 0, \\ &\theta(\eta) \to 0,\ \theta_p(\eta) \to 0 \text{ as } \eta \to \infty, \\ &\phi(\eta) = 1 \text{ at } \eta = 0, \\ &\phi(\eta) \to 0,\ \phi_p(\eta) \to 0 \text{ as } \eta \to \infty. \end{aligned} \tag{6.28}$$

Where $\Pr = \frac{\mu c_p}{k}$, $R = \frac{4\sigma^* T_\infty^3}{kk^*}$, $\gamma = \frac{c_p}{c_m}$, $Ec = \frac{U_0^2 e^{\frac{2x}{L}}}{c_p T_0 e^{\frac{c_1 x}{2L}}}$, $A = \frac{\alpha L}{U_0 e^{\frac{x}{L}}}$, $\beta = \frac{L}{\tau_v U_0 e^{\frac{x}{L}}}(1-\alpha t)$, $\beta_T = \frac{L}{\tau_T U_0 e^{\frac{x}{L}}}(1-\alpha t)$, $\lambda^* = \frac{QL^2}{\mu c_p Re}$, $Re = \frac{U_0 L e^{\frac{x}{L}}}{\nu(1-\alpha t)}$, $N_t = \frac{(\rho c_p)_p D_T (T_w - T_\infty)}{\rho c_p \nu T_\infty}$, $N_b = \frac{(\rho c_p)_p D_B (C_w - C_\infty)}{\rho c_p \nu}$ and $Sc = \frac{\nu}{D_B}$.

6.3.2 Case 2: VEHF (Variable exponential order heat and mass flux):

For this heat and mass transfer procedure, consider the following boundary conditions

$$\begin{aligned} &\frac{\partial T}{\partial y} = -\frac{q_w(x,t)}{k_f} \text{ at } y = 0, \\ &T \to T_\infty,\ T_p \to T_\infty \text{ as } y \to \infty, \\ &\frac{\partial C}{\partial y} = -\frac{q_m(x,t)}{D_B} \text{ at } y = 0, \\ &C \to C_\infty,\ C_p \to C_\infty \text{ as } y \to \infty, \end{aligned} \tag{6.29}$$

where $q_w = \frac{T_1}{(1-\alpha t)^{5/2}} e^{\frac{(b_1+1)x}{2L}}$, $q_m = \frac{C_1}{(1-\alpha t)^{5/2}} e^{\frac{(c_1+1)x}{2L}}$ are heat and mass fluxes. Now by again using eq.(6.23) into eqs.(6.16, 6.19, 6.20, 6.21 and 6.22), we get the same system of equations, with Eckert number as $Ec = \frac{k_c U_o^2}{c_p T_1}\sqrt{\frac{U_0}{2\nu L}}$, which only is dissimilar from the first case, all the other quantities are similar to VEST.

Boundary conditions for above case transform to

$$\begin{aligned}
&\theta'(\eta) = -1 \text{ at } \eta = 0, \\
&\theta(\eta) \to 0,\ \theta_p(\eta) \to 0 \text{ as } \eta \to \infty, \\
&\phi'(\eta) = -1 \text{ at } \eta = 0, \\
&\phi(\eta) \to 0,\ \phi_p(\eta) \to 0 \text{ as } \eta \to \infty.
\end{aligned} \tag{6.30}$$

The Nusselt and Sherwood number are defined as,

$$Nu_x = \frac{xq_w}{k_f\left(T - T_\infty\right)}, \tag{6.31}$$

$$Sh_x = \frac{xq_m}{D_B\left(C - C_\infty\right)}, \tag{6.32}$$

where q_w and q_m are the heat and mass transfer from the sheet respectively, which are presumed as,

$$q_w = -k_c\left(\frac{\partial T}{\partial y}\right)_{y=0}, \tag{6.33}$$

$$q_m = -D_B\left(\frac{\partial C}{\partial y}\right)_{y=0}. \tag{6.34}$$

Making use of non-dimensional factors we have,

$$\frac{Nu_x}{\sqrt{2Re}} = -\frac{x}{2L}\theta'(0),\ \frac{Sh_x}{\sqrt{2Re}} = -\frac{x}{2L}\phi'(0)\left(\text{VESTCase}\right), \tag{6.35}$$

$$\frac{Nu_x}{\sqrt{2Re}} = \frac{x}{2L}\frac{1}{\theta(0)}, \quad \frac{Sh_x}{\sqrt{2Re}} = \frac{x}{2L}\frac{1}{\phi(0)} \quad (\text{VEHFCase}). \tag{6.36}$$

6.4 Solution procedure:

6.4.1 Optimal Homotopy Analysis Method:

The nonlinear coupled ODE's for VEST and VEHF case are analytically resolved by Optimal Homotopy Analysis Method (OHAM). The series solution for the present problem is deliberated via optimal HAM. The mechanism is utilized to demonstrate solutions for non-linear equations. The entire interpretation can be found in [96, 97]. In the evaluation of the problem one needs the linear operators and initial guesses which are given below for the under discussion problem

Utilizing the rule of solution expression and the given boundary conditions, the initial guesses $f_0, F_0, \theta_0, \theta_{p_0}, \phi_0, \phi_{p_0}$ can be chosen as:

$$\begin{aligned} &f_0(\eta) = (1+s) - \exp(-\eta), \; F_0(\eta) = (1+s) - \exp(-\eta), \; \theta_0(\eta) = \exp(-\eta), \\ &\theta_{p_0}(\eta) = \exp(-\eta), \; \phi_0(\eta) = \exp(-\eta), \; \phi_{p_0}(\eta) = \exp(-\eta). \end{aligned} \tag{6.37}$$

The auxiliary linear operators are selected as follows:

$$\begin{aligned} &\mathcal{L}_f = \frac{d^3}{d\eta^3} - \frac{d}{d\eta}, \; \mathcal{L}_F = \frac{d^2}{d\eta^2} - \frac{d}{d\eta}, \; \mathcal{L}_\theta = \frac{d^2}{d\eta^2} - 1, \\ &\mathcal{L}_{\theta_p} = \frac{d}{d\eta} - 1, \; \mathcal{L}_\phi = \frac{d^2}{d\eta^2} - 1, \; \mathcal{L}_{\phi_p} = \frac{d^2}{d\eta^2} - \frac{d}{d\eta}, \end{aligned} \tag{6.38}$$

6.4.2 Optimal convergence-control parameters

Homotopy analysis solutions consists of the non-zero auxiliary parameters c_0^f, c_0^F, c_0^θ, $c_0^{\theta_p}$, c_0^ϕ and $c_0^{\phi_p}$ which act as helping tool in determining the area of convergence and rate of the homotopy series solution. By finding the so-called average residual errors [72] we get the optimal values of c_0^f, c_0^F, c_0^θ, $c_0^{\theta_p}$, c_0^ϕ and $c_0^{\phi_p}$. ***Tables*** $\mathbf{6.1}$ and $\mathbf{6.2}$ present the values for several optimal convergence control parameters and reveals the fact that the total squared average residual errors diminish when the rank of estimation increases, this proves that the solution obtained is convergent at higher order estimations. Hence, OHAM delivers a proper way to select any value of local optimal convergence control parameters to attain the convergent solutions.

values / m	c_0^f	c_0^F	c_0^θ	$c_0^{\theta_p}$	c_0^ϕ	$c_0^{\phi_p}$	δ_m	CPU time
2	−0.558	−0.490	−0.467	0.468	−0.916	0.791	2.537×10^{-2}	10.81
4	−0.560	−0.589	−0.705	0.470	−0.635	.732	1.352×10^{-3}	139.96
6	−0.556	−0.627	−0.768	0.499	−0.565	0.644	2.072×10^{-4}	1177.21
8	−0.567	−0.542	−0.894	0.512	−0.630	0.504	1.365×10^{-4}	10637.1

Table 6.1. Total squared average residual errors. (VEST Case)

$\frac{values}{m}$	c_0^f	c_0^F	$c_0^{\bullet}$	$c_0^{\bullet_p}$	c_0^{Ω}	$c_0^{\Omega_p}$	ε_m	CPU time
2	0.561	0.494	0.594	0.399	0.639	0.790	2.31×10^{-2}	11.55
4	0.570	0.570	0.670	0.486	0.674	0.723	1.835×10^{-3}	139.83
6	0.565	0.560	0.793	0.504	0.470	0.630	3.836×10^{-4}	2020.91
8	0.576	0.537	0.852	0.503	0.455	0.501	1.869×10^{-4}	10032.7

Table 6.2. Total squared average residual errors. (VEHF Case)

where ε_m is the total squared residual error.

Table 6.3 and ***Fig. 6.2*** depict that the individual averaged squared residual errors also diminish as the rank of approximation increases, proving that the answer is convergent

m	ε_m^f	ε_m^F	$\varepsilon_m^{\bullet}$	$\varepsilon_m^{\bullet_p}$	ε_m^{Ω}	$\varepsilon_m^{\Omega_p}$	CPU time
4	3.416×10^{-4}	3.02×10^{-4}	2.180×10^{-4}	1.610×10^{-4}	8.69×10^{-4}	6.236×10^{-4}	9.99
8	1.029×10^{-6}	1.466×10^{-5}	2.809×10^{-5}	2.901×10^{-5}	1.955×10^{-4}	2.863×10^{-4}	73.37
12	7.872×10^{-9}	1.015×10^{-6}	5.949×10^{-6}	6.274×10^{-6}	7.705×10^{-5}	3.260×10^{-5}	262.09
16	2.772×10^{-10}	8.601×10^{-8}	1.578×10^{-6}	1.577×10^{-6}	3.447×10^{-5}	2.701×10^{-6}	669.55

Table 6.3. Individual squared average residual errors at m = 2 (VEST Case).

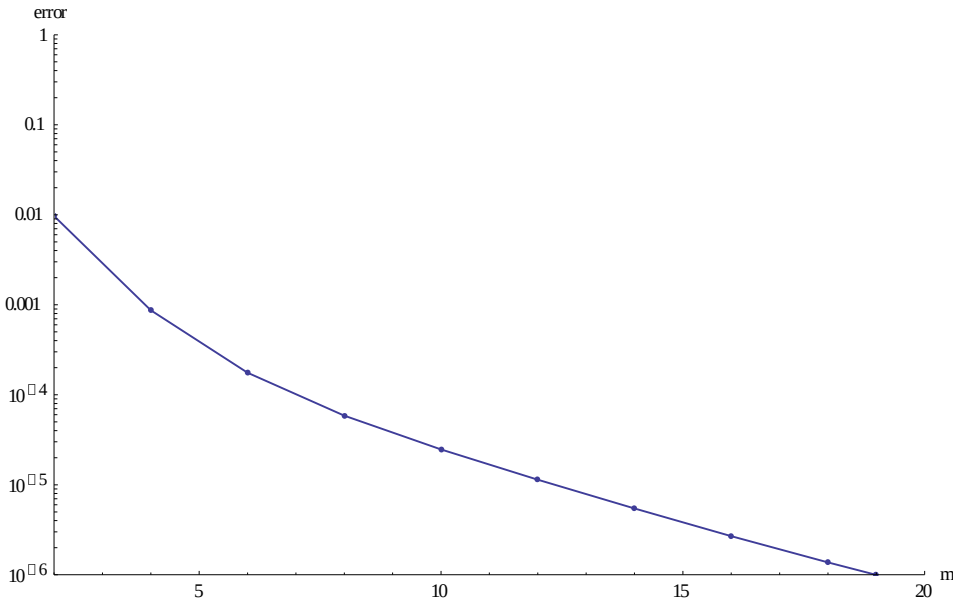

Fig. 6.2. Individual squared residual error when m = 2.

6.5 Results and Discussion:

The non-linear ODE's $(6.8-6.10 \text{ and } 6.24-6.27)$ along with the boundary conditions (6.11), (6.28) and (6.30) have been solved analytically by using the OHAM. The influence of many considerations on the temperature and concentration profiles is presented graphically in ***Figs.6.3-6.28.*** Different properties of fluid at the surface are investigated for skin friction coefficient, temperature gradient $\theta'(0)$ and concentration gradient $\phi'(0)$ in case of VEST and temperature $\theta(0)$ and concentration $\phi(0)$ in VEHF case. The values of $\beta_T = 0.6,\ c_1 = 1, \rho = 1, \gamma = 1.4$ and $l = 0.1$ are used in our calculations.

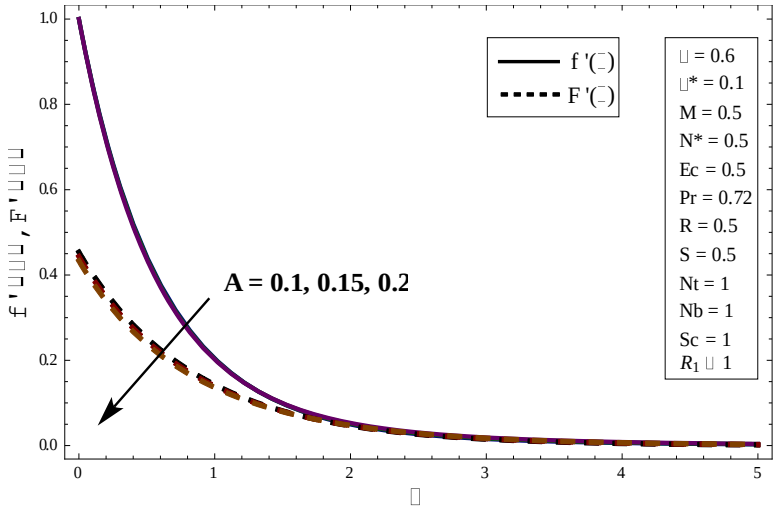

Fig. 6.3. Influence of *A* upon velocity.

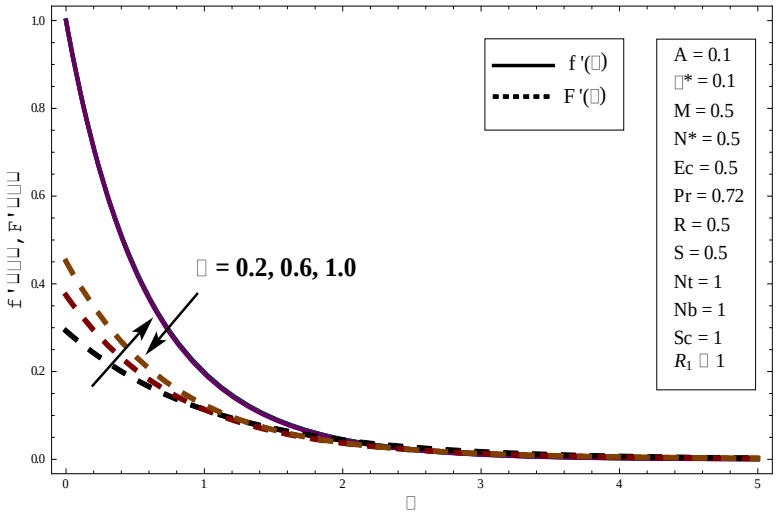

Fig. 6.4. Influence of β upon velocity.

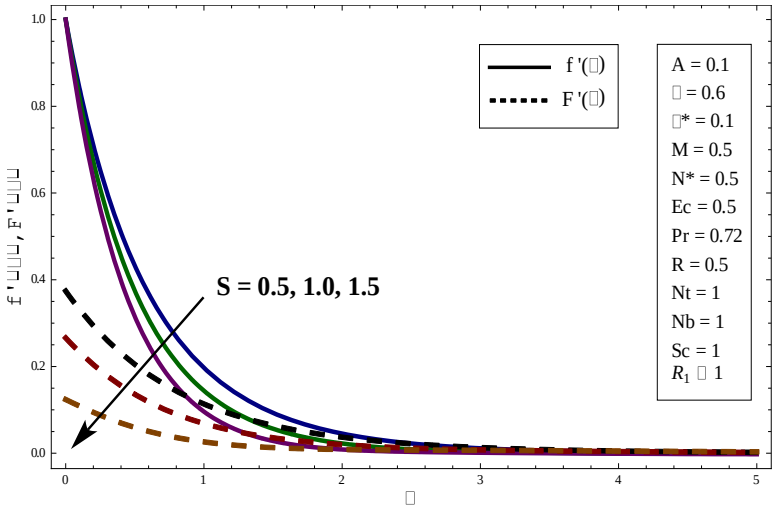

Fig. 6.5. Influence of *S* upon velocity

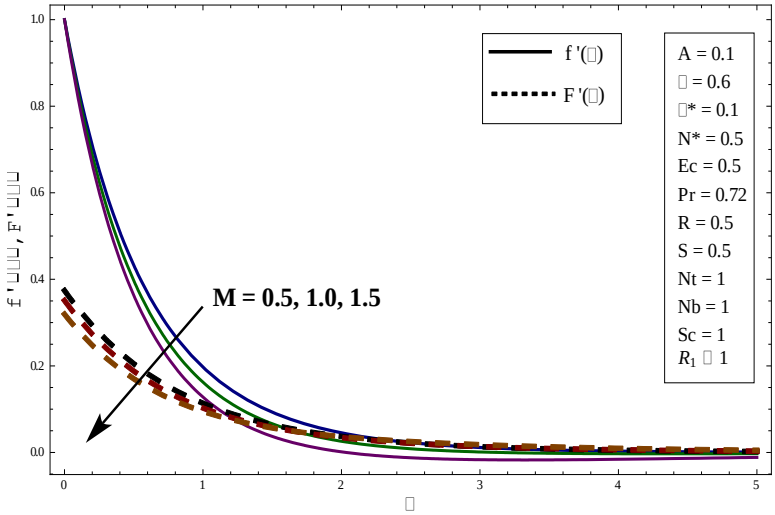

Fig. 6.6. Influence of *M* upon velocity.

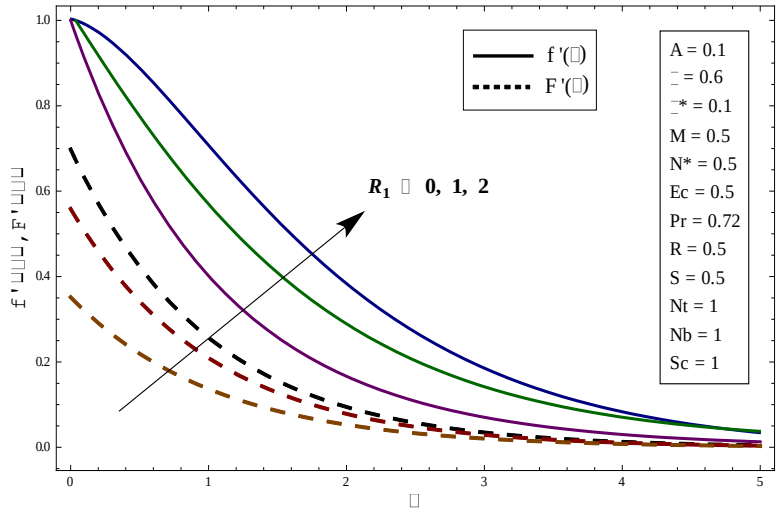

Fig. 6.7. Influence of R_1 upon velocity.

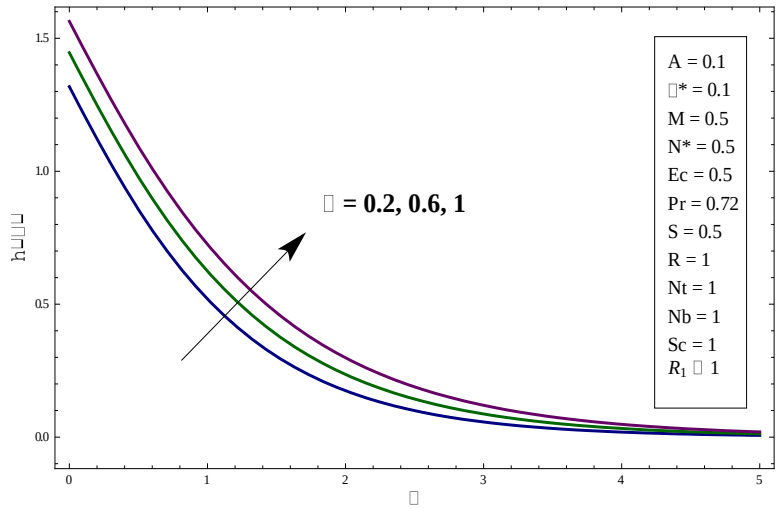

Fig. 6.8. Influence of β on micro-rotation profile.

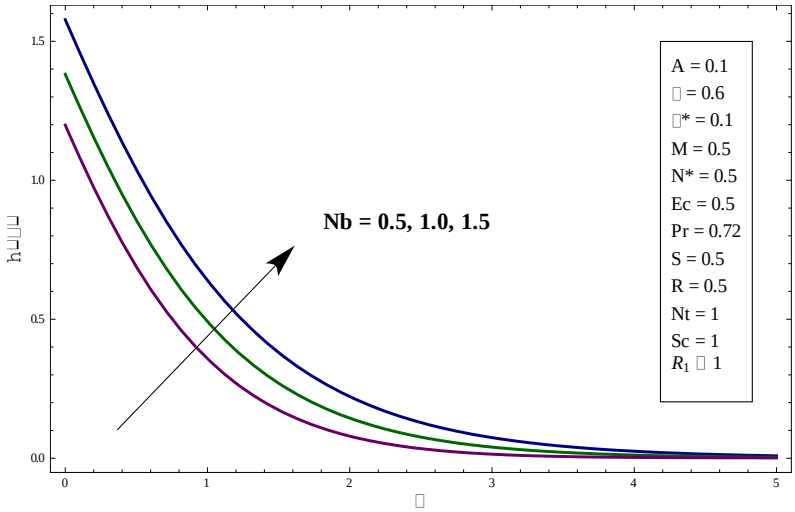

Fig. 6.9. Influence of Nb on micro-rotation profile.

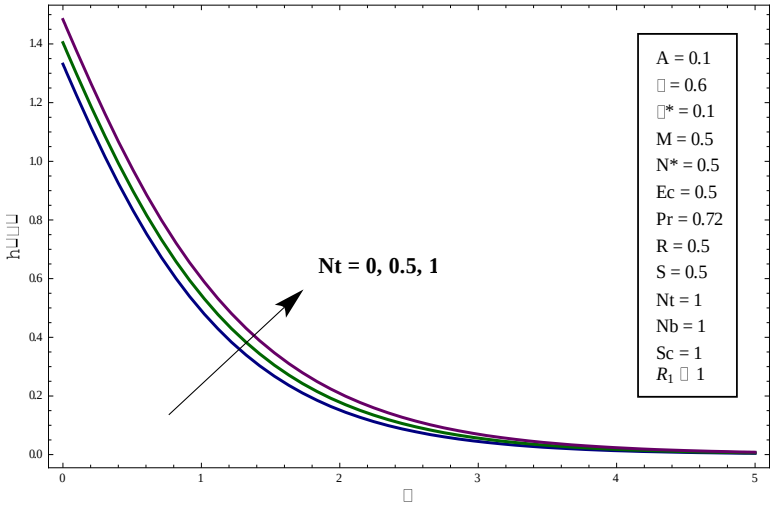

Fig. 6.10. Influence of Nt on micro-rotation profile.

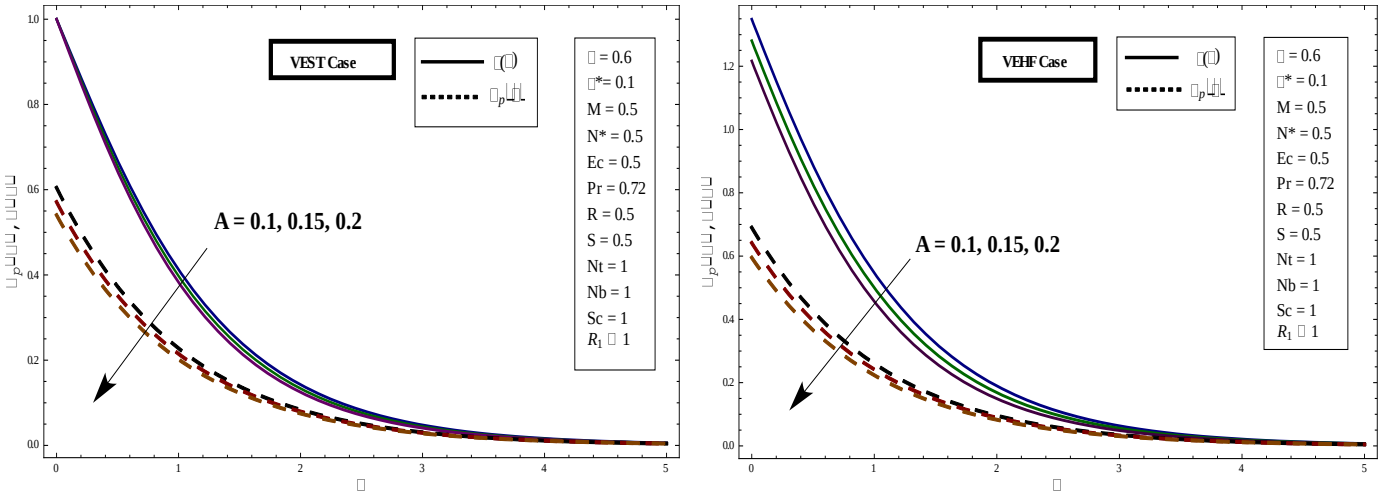

Fig. 6.11. Influence of *A* upon temperature distribution for (i) VEST (ii) VEHF case.

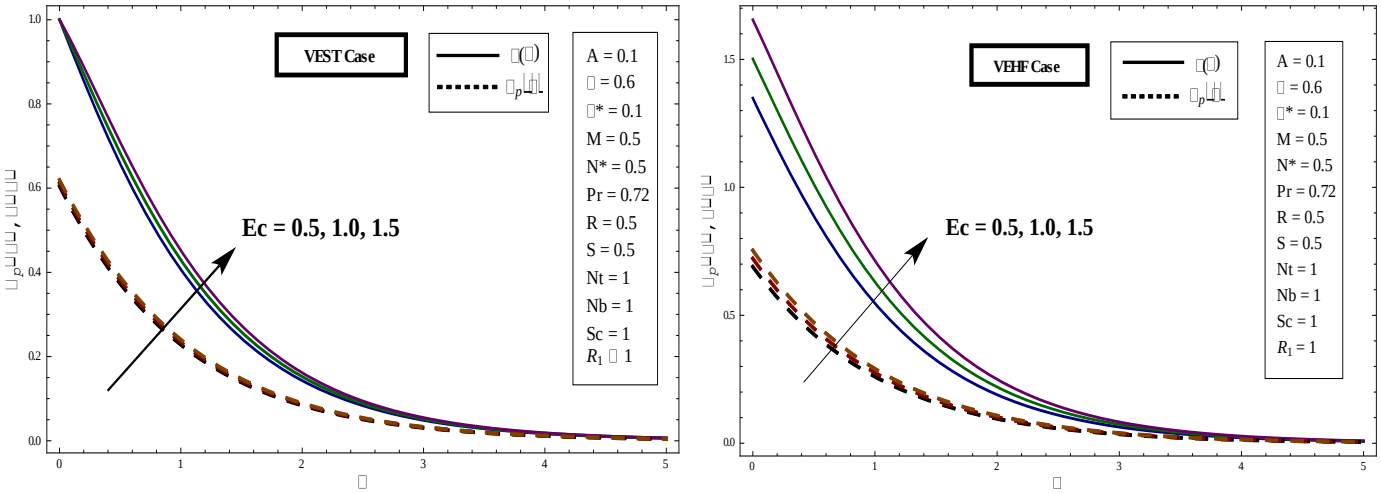

Fig. 6.12. Influence of *Ec* upon temperature distribution for (i) VEST (ii) VEHF case.

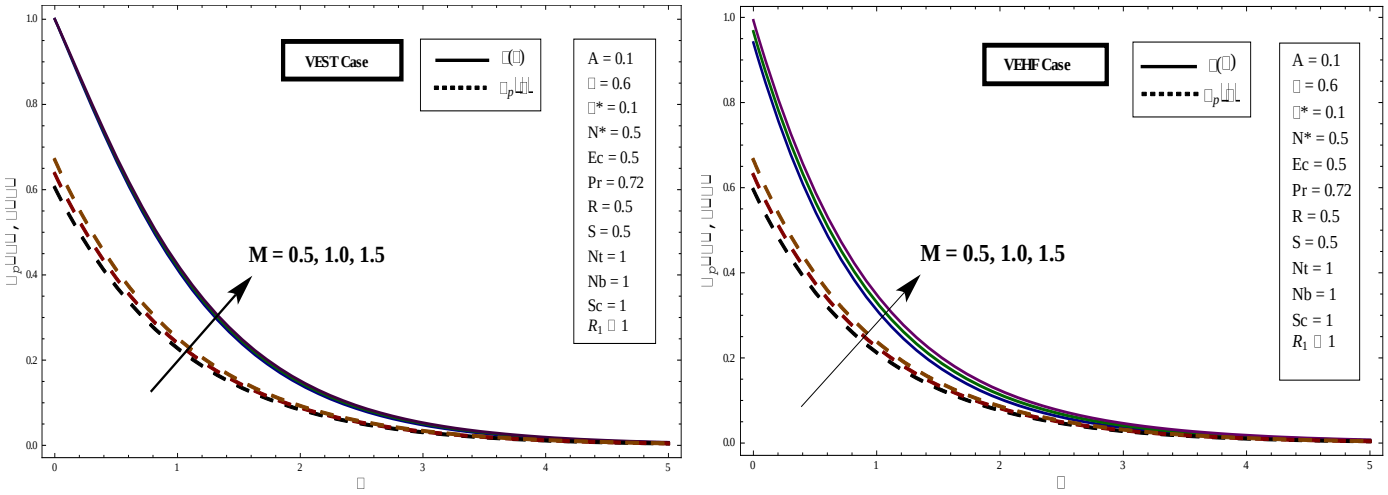

Fig. 6.13. Influence of *M* upon temperature distribution for (i) VEST (ii) VEHF case.

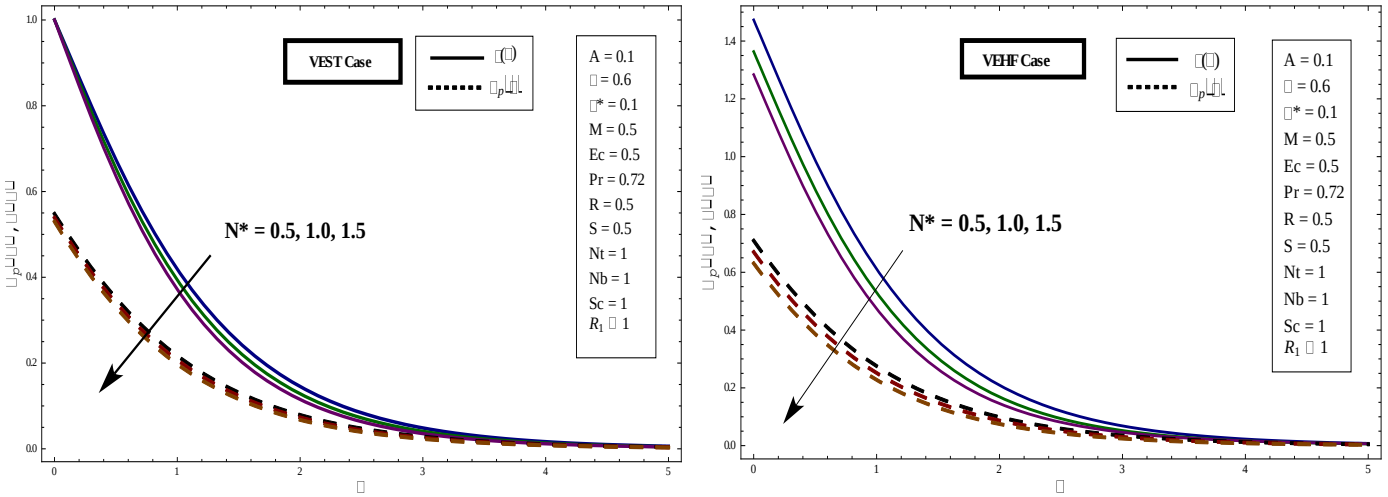

Fig. 6.14. Influence of *N** upon temperature distribution for (i) VEST (ii) VEHF case.

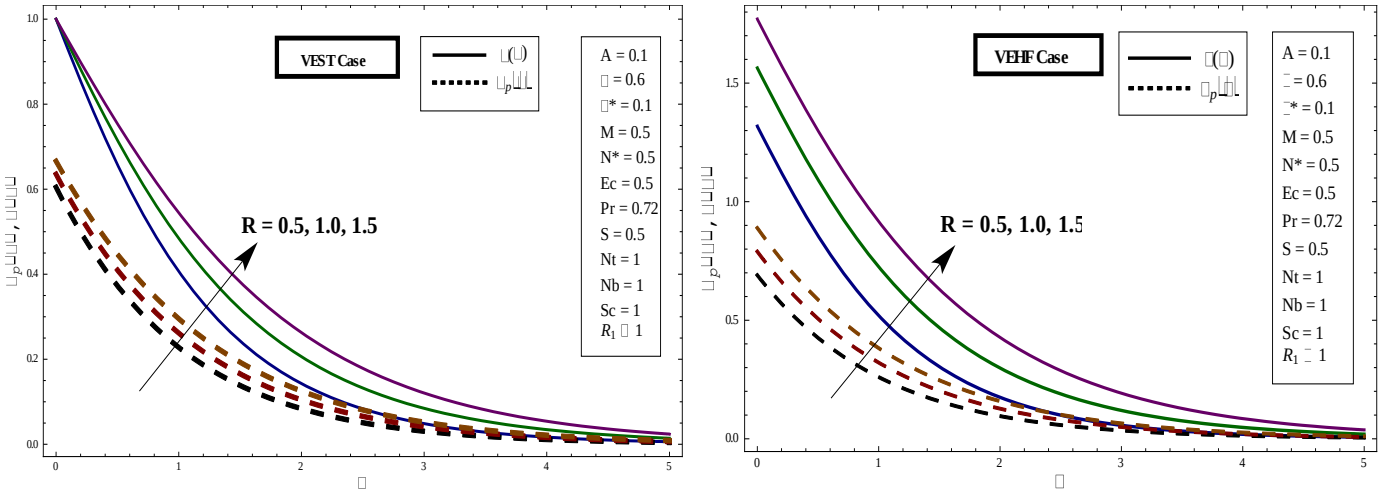

Fig. 6.15. Influence of *R* upon temperature distribution for (i) VEST (ii) VEHF case.

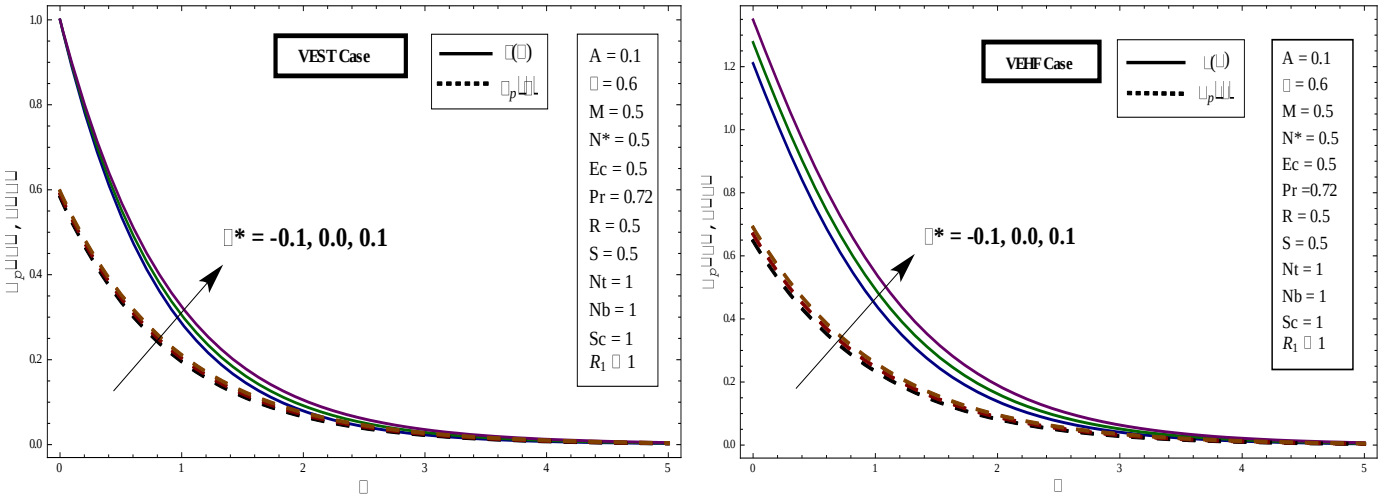

Fig. 6.16. Influence of λ^* upon temperature distribution for (i) VEST (ii) VEHF case.

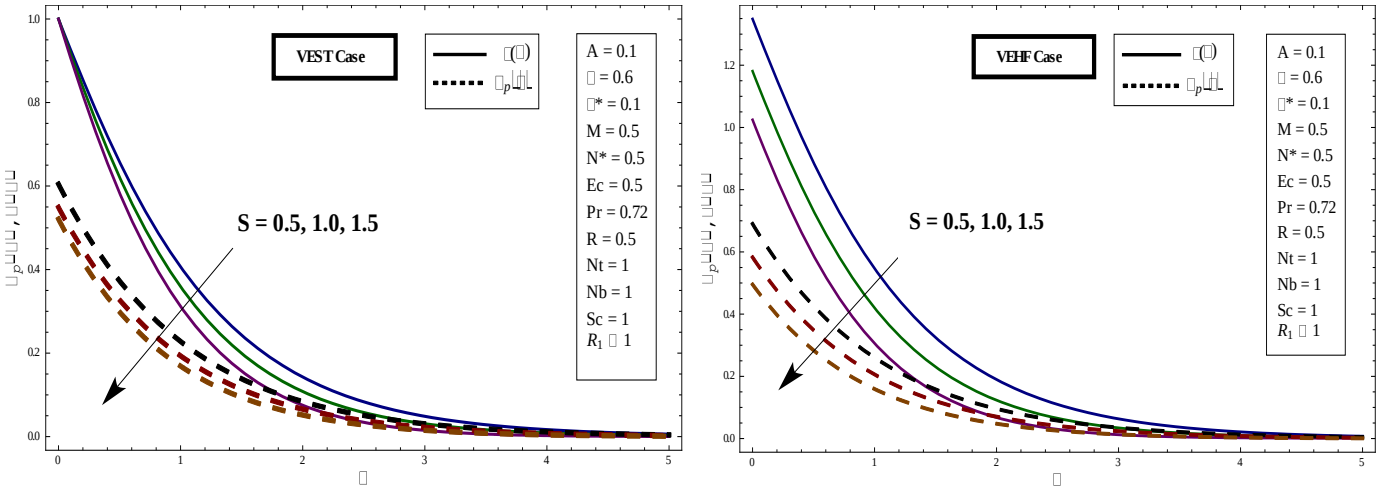

Fig. 6.17. Influence of *S* upon temperature distribution for (i) VEST (ii) VEHF case.

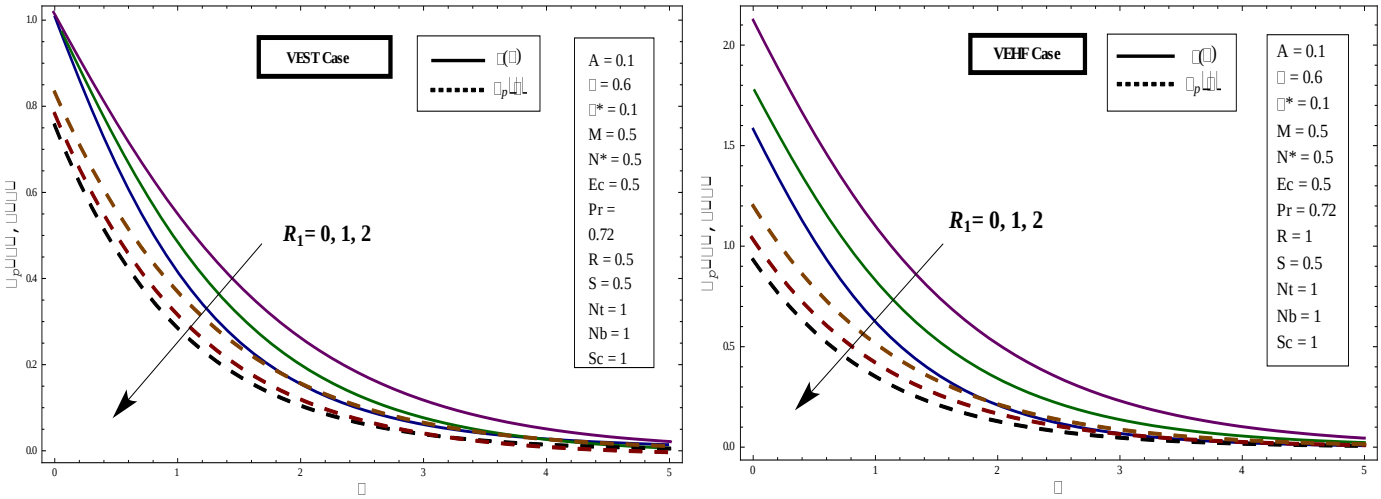

Fig. 6.18. Influence of R_1 upon temperature profiles for (i) VEST (ii) VEHF case.

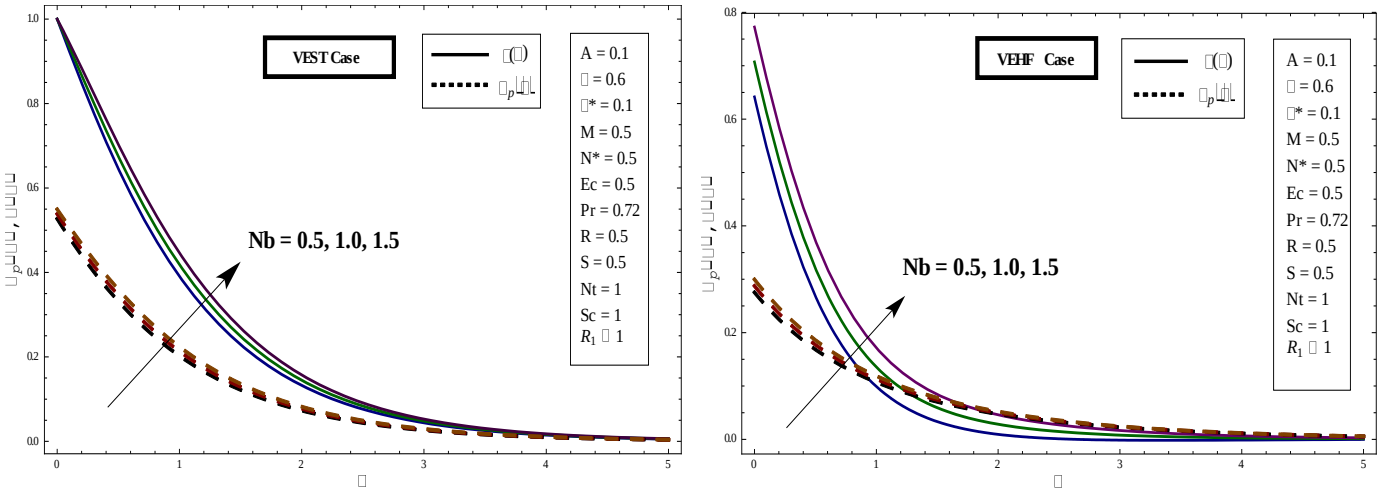

Fig. 6.19. Influence of Nb upon temperature distribution for (i) VEST (ii) VEHF case.

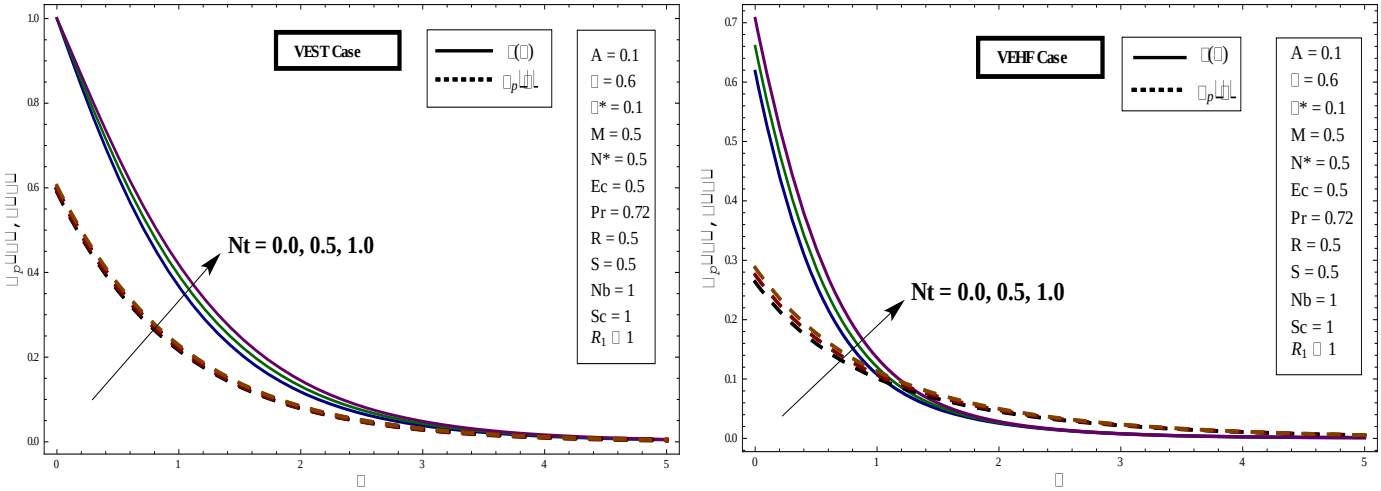

Fig. 6.20. Influence of Nt upon temperature distribution for (i) VEST (ii) VEHF case.

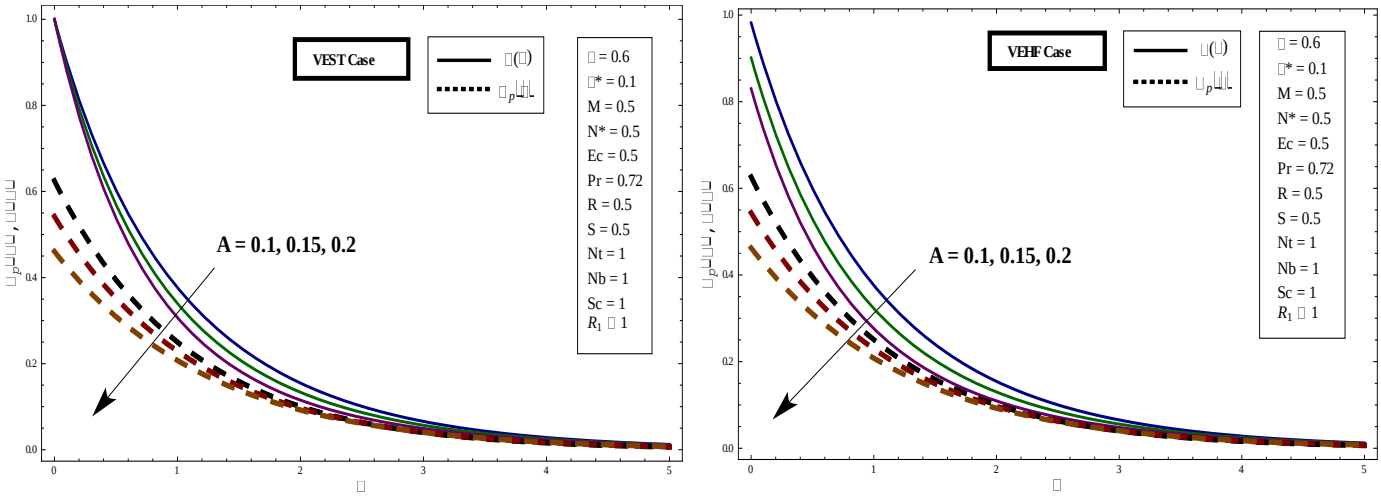

Fig. 6.21. Influence of *A* on concentration profiles for (i) VEST (ii) VEHF case.

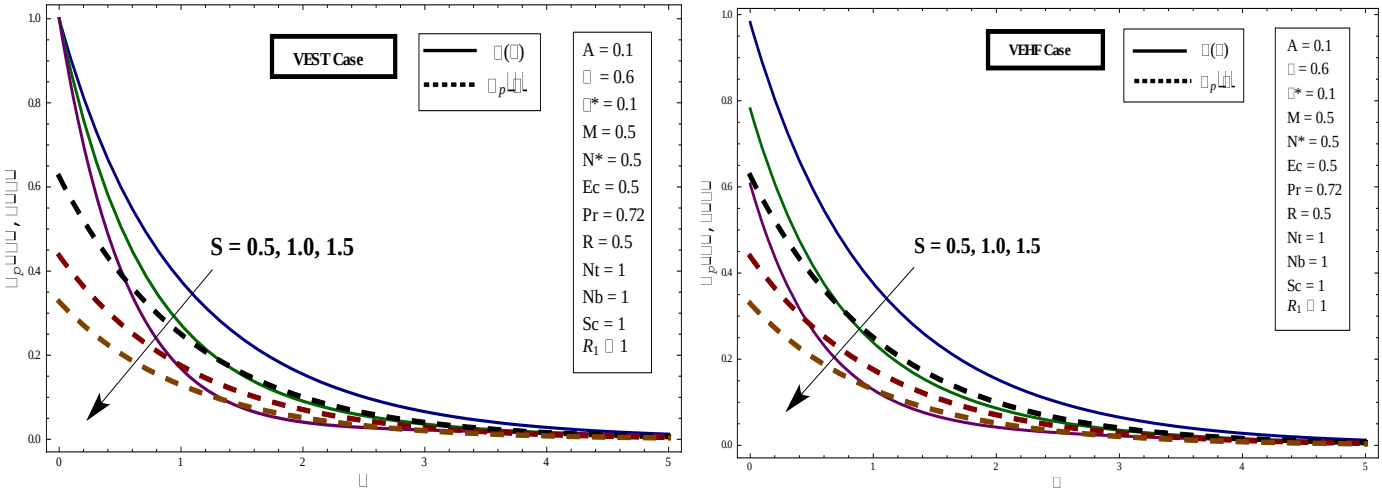

Fig. 6.22. Influence of *S* upon concentration profiles for (i) VEST (ii) VEHF case.

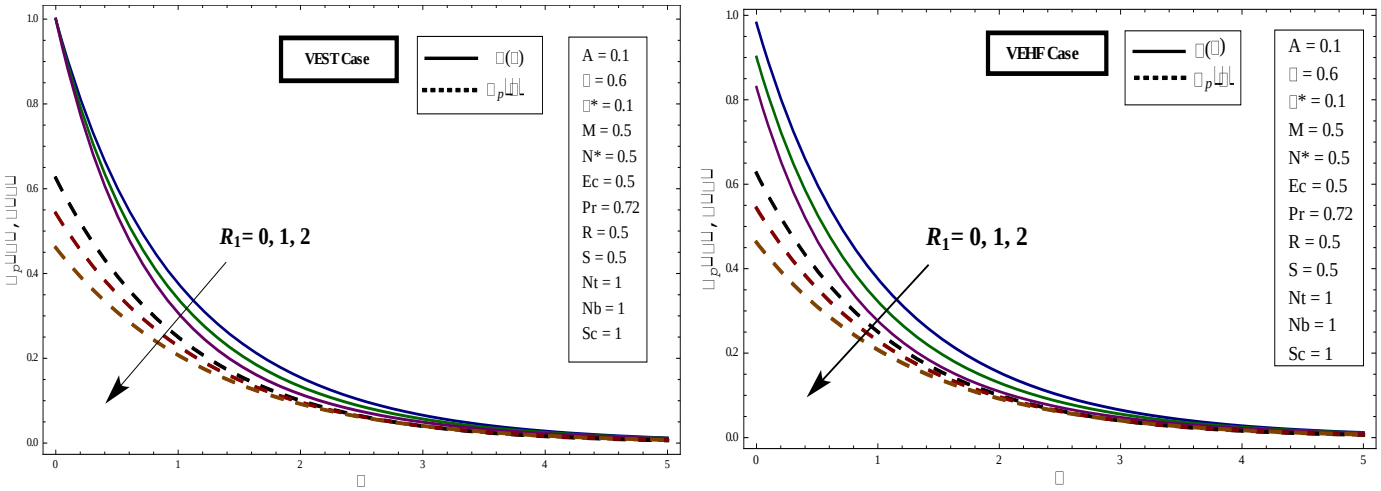

Fig. 6.23. Influence of R_1 upon concentration profiles for (i) VEST (ii) VEHF case.

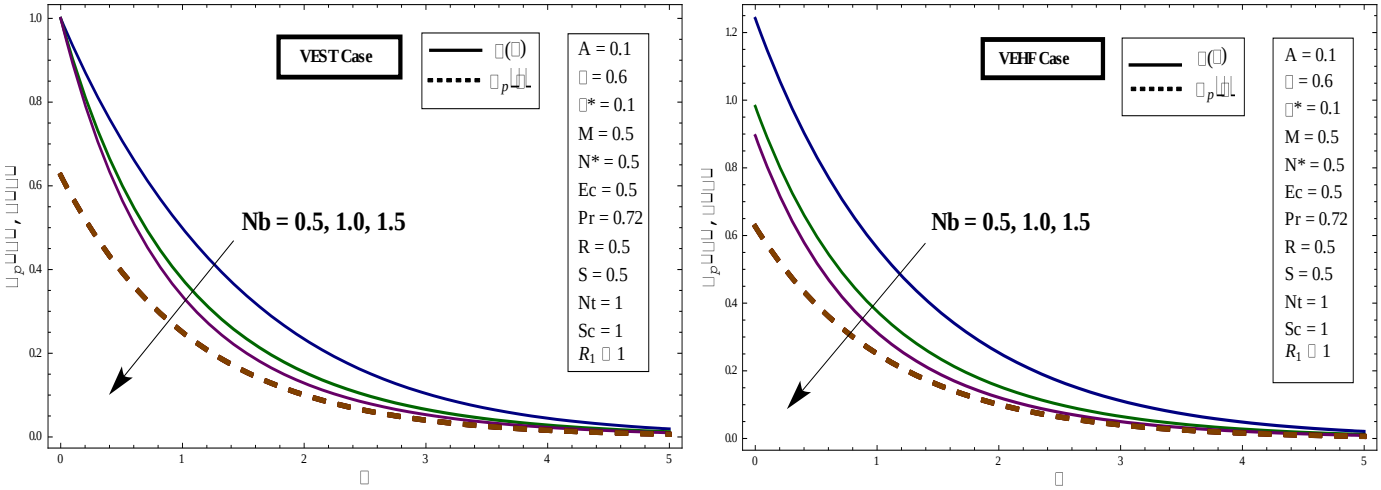

Fig. 6.24. Influence of N_b upon concentration profiles for (i) VEST (ii) VEHF case.

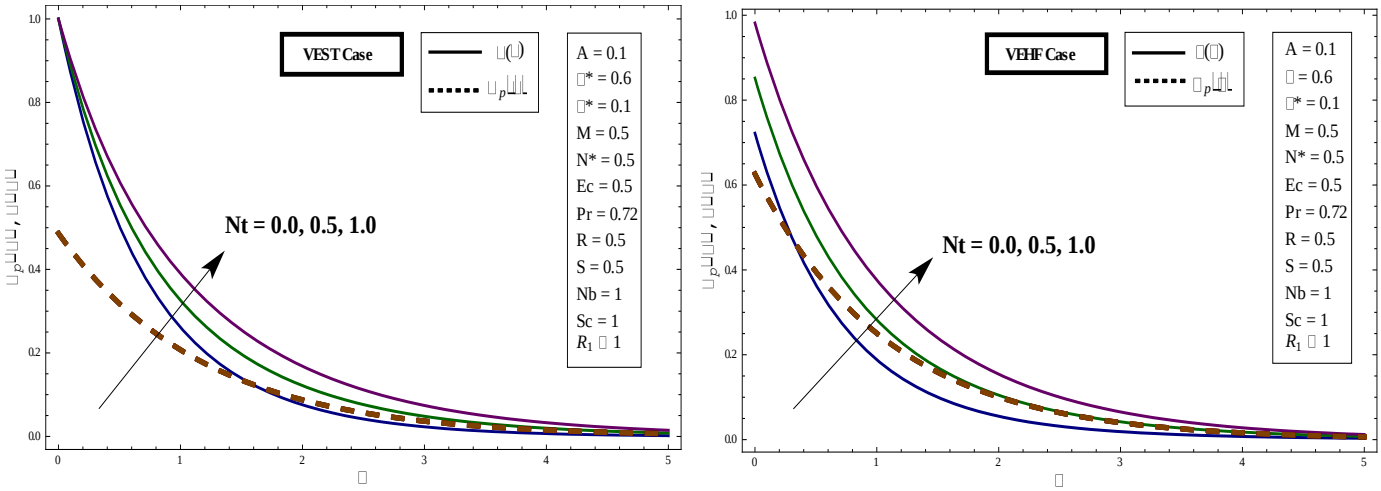

Fig. 6.25. Influence of N_t upon concentration profiles for (i) VEST (ii) VEHF case.

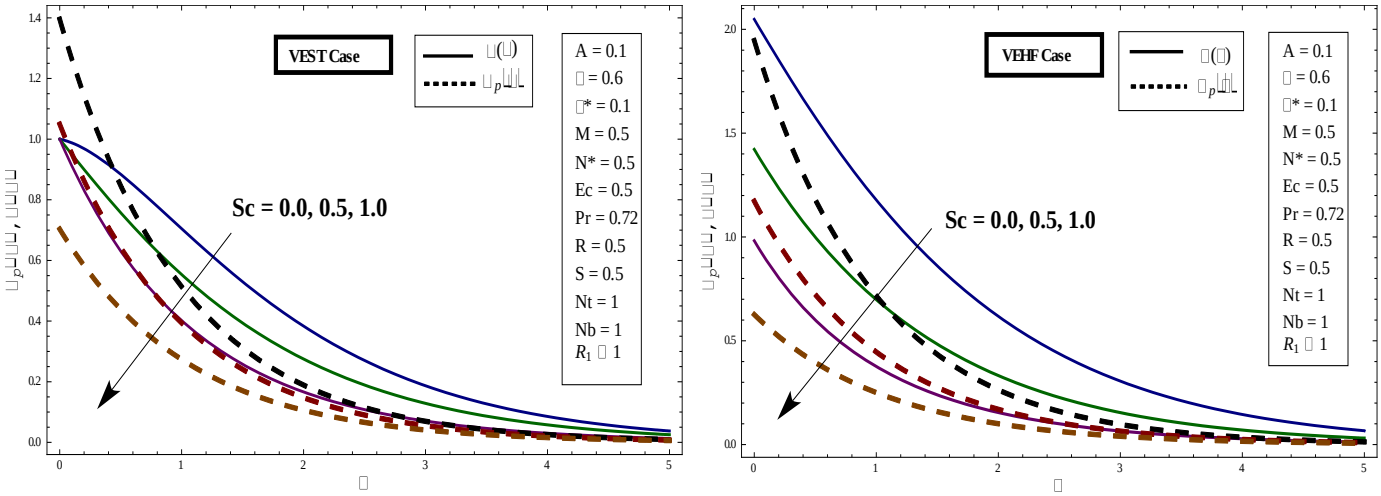

Fig. 6.26. Influence of *Sc* upon concentration profiles for (i) VEST (ii) VEHF case.

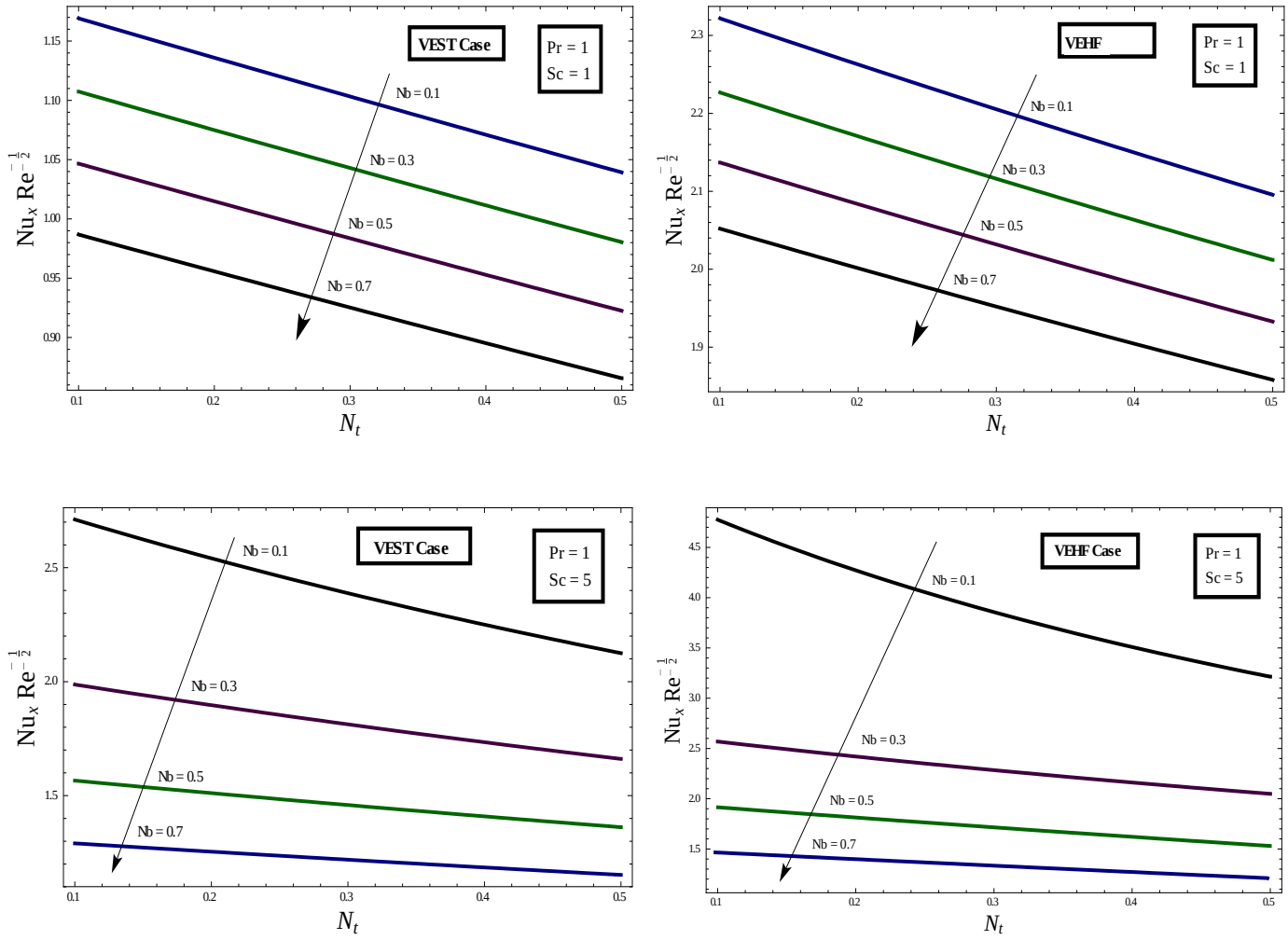

Fig. 6.27. Result of varying N_b and N_t upon heat transfer rate for (i) VEST (ii) VEHF case.

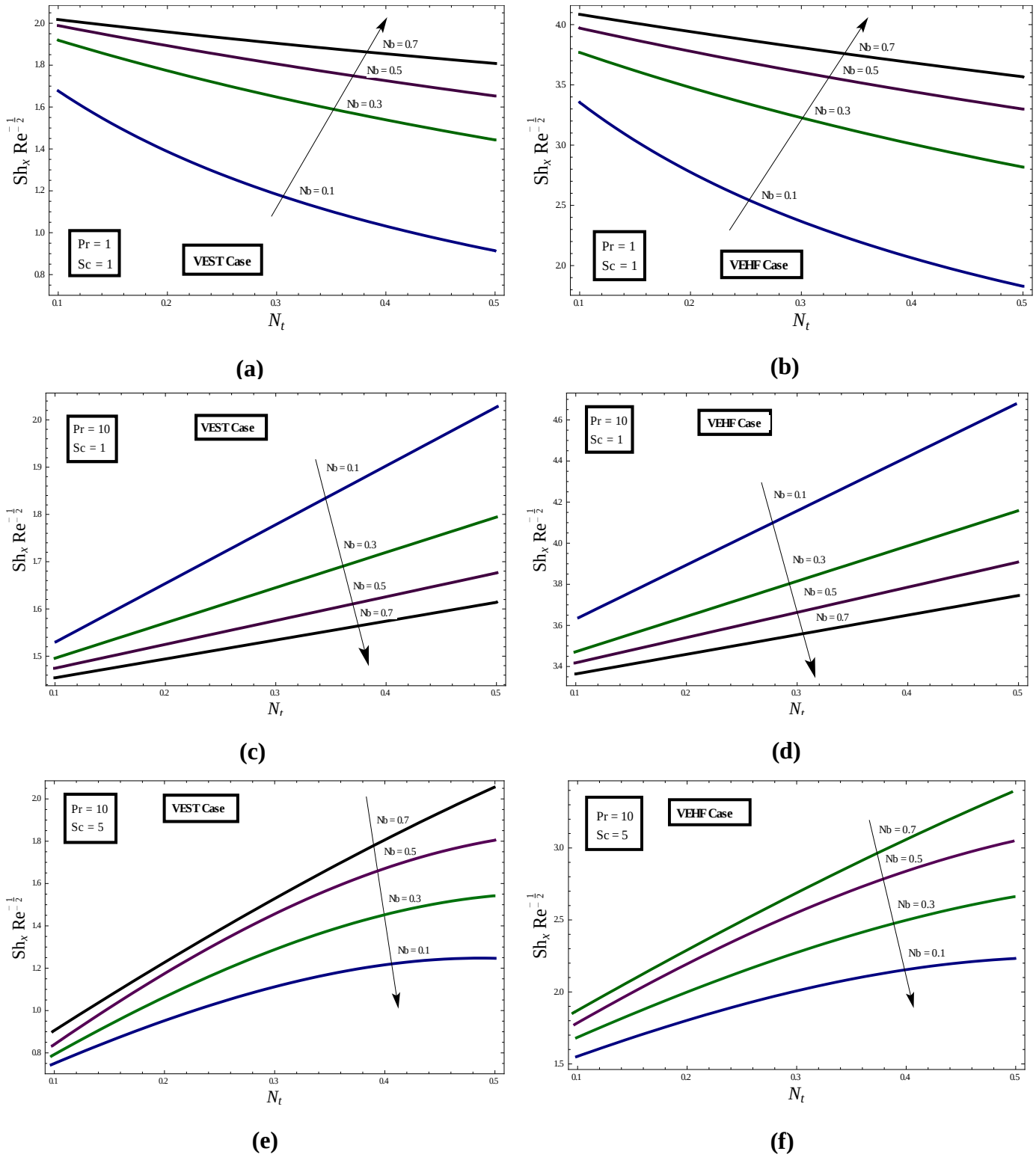

Fig. 6.28. Result of varying N_b and N_t upon dimensionless mass transfer rate for (i) VEST (ii) VEHF case.

In order to scrutinize results of the present research an analytical analysis is performed for unsteady micropolar dusty fluid flow with MHD. ***Fig. 6.3*** represents a considerable variation in the velocity fields $f'(\eta)$ and $F'(\eta)$ for enhancing the values of unsteadiness parameter. It is witnessed that both fluid as well as dust phase velocities decrease when we increase the unsteady parameter. Similarly boundary layer width decreases with augmenting values of A. ***Fig. 6.4*** is plotted to inspect the impact of fluid particle interaction parameter β on velocity profiles. It is perceived that the fluid phase velocity profile decreases with increasing β while the dust phase velocity profile enhances with amplifying values of β.

Fig. 6.5. describes the influence of S, the suction parameter, upon velocity profiles. By enhancing values of S both the velocity profiles decrease significantly and with this reduction in velocity profiles boundary layer thickness also decreases. From ***Fig.6.6.*** it is realized that increasing values of M decreases the velocity profile. Physically M is the fraction between electromagnetic forces and viscous forces thus higher values of M represents the increase in the Lorentz force. This is drag-like force that creates more resistance to transport phenomenon and fluid velocity also the boundary layer thickness diminishes. ***Fig.6.7.*** is sketched to understand the influence of R_1 upon velocity fields. $R_1 = {}^{k}/_{\mu}$ provides the ratio of two viscosities, the vortex viscosity and the dynamic viscosity so as the R_1 increases the velocity escalates since the fluid particles are accelerated due to vortex viscosity and the dynamic viscosity decreases hence offering less resistance to the flow. ***Fig.6.8-6.10*** are plotted to see the variation of β, Nb and Nt on micro rotation profile $h(\eta)$. Increasing values of β increases $h(\eta)$ since as the particle interaction increases so micro-rotations of particles also increases. ***Fig.6.9.*** illustrates that with increasing variation in values of Nb the micro-rotations also increase and similar is the case with Nt.

Figs.6.11.-6.20. represent the effects of a number of parameters on temperature of fluid segment and dust segment for VEST and VEHF cases. ***Fig.6.11.*** shows us the effect of unsteadiness parameter A upon temperature profiles $\theta(0)$ and $\theta_p(0)$. As A increases there is a decrease in both temperature profiles because when we increase the unsteadiness parameter the surface temperature gradient also increases resulting in higher level of heat transfer. Thus for larger values of A the rate of cooling is very fast.

In ***Fig.6.12.*** we analyze the impact on temperature distributions of Eckert number Ec which embodies viscous dissipation changes. The temperature increases when we increase Ec, as viscous dissipation plays the role of energy source because there is stored heat energy in fluid owing to frictional heating. ***Fig.6.13.*** illustrates the effect on temperature profiles due to the variation in magnetic parameter M. In both VEST and VEHF case the temperature profiles enhance with rise in values of M. It is also noted that the plots for fluid's and dust particle's temperature profiles stay parallel to each other. Effect on temperature distributions for variation in number density N^* is illustrated in ***Fig.6.14.*** When we increase N^* we notice a decrease in temperature profiles of both VEST and VEHF cases.

Now we discuss the effects of parameter of radiation R on temperature distributions of fluid and dust particles as shown in ***Fig.6.15.*** In both VEST and VEHF cases when we increase R there is amplification in temperature as well as the thermal boundary layer thickness.

Fig.6.16. displays the temperature distributions with varying heat source/sink parameter λ^*. We conclude from this graphical representation that with an upsurge in λ^* temperature increases because energy is released at thermal boundary layer in case of heat source while the case is opposite for heat sink. ***Fig.6.17.*** represents the impact of suction parameter S on temperature profiles. From here we can observe that when S rises the temperature profiles decrease and boundary layer becomes thin.

The impact of vortex viscosity parameter R_1 upon temperature fields can be seen in ***Fig.6.18.*** As we increase R_1 there a reduction in temperature profiles can be observed. ***Figs.6.19.-6.20.*** are designed to examine the behavior of temperature profiles against the brownian motion parameter Nb and the thermophoresis parameter Nt for both VEST and VEHF cases. It is detected that rise in Nb and Nt intensifies the temperature distribution of fluid and dust phase as they both increase the surface temperature. In ***Figs.6.21.-6.26.*** the concentration profiles $\phi(\eta)$ and $\phi_p(\eta)$ are plotted for different parameters involved in our study. We observe through ***Figs 6.21.-6.22.*** that when we enhance the values of the unsteadiness parameter A and suction parameter S there is a decline in the concentration profiles of both fluid and dust particles. ***Fig.6.23.*** demonstrates the nature of concentration with variation of vortex viscosity parameter R_1. With increase in the values of R_1 the concentration profile drops. Through ***Figs.6.24.-6.26*** it is observed that by rise in the values of thermophoretic parameter Nt, there is

an increase in concentration profiles. Whereas, increase in Schimdt number Sc and Brownian motion parameter Nb decreases the concentration as well as the thickness of the boundary layer. This is because of the fact that an increase in Sc implies a decrease in the molecular diffusivity. ***Fig.6.27.*** is drawn to see the behavior of Nusselt number by varying the values of Nt and Nb. Increasing the values of both Nt and Nb decreases the Nusselt number. ***Fig.6.28.*** depicts the variance in dimensionless mass transfer rates against Nt, Nb, Sc and Pr for VEST and VEHF cases. ***Fig.6.28. (a)*** exhibits that the Sherwood number decreases with the enhancement of Nt for lower Pr value. Similar to the Nusselt number, the variation in the mass transfer rates is significant for minute values of the parameter Nb and shows a rise in its value with the rise in Nb. On the contrary, for larger values of Pr both the parameters have opposite effects. The impact of Sc on Sherwood number or dimensionless mass transfer can be observed by comparing ***Figs.6.28. (c,d)*** and ***6.28. (e,f)*** for same Prandtl number. The change in Sherwood number is monotonic throughout for larger and smaller values of Sc. For validation of our results with the existing literature a comparison table is illustrated in ***Table 6.4.***

Table 6.4. Comparison with the existing literature for skin friction and heat transfer rate taking $N_t = N_b = R_1 = n = 0$.

A	*M*	Pavithra et al. $f''(0)$	Present analysis	Pavithra et al. $\theta'(0)$	Present analysis
0.0		**-1.75075**	**-1.75079**	**-0.52678**	**-0.52680**
0.1	**0.5**	**-1.79715**	**-1.79720**	**-0.67457**	**-0.67461**
0.2		**-1.84300**	**-1.84306**	**-0.79060**	**-0.79065**
	0.5	**-1.79715**	**-1.79720**	**-0.67457**	**-0.67461**
0.1	**1.0**	**-1.95373**	**-1.95377**	**-0.64168**	**-0.64172**
	1.5	**-2.09640**	**-2.09645**	**-0.61316**	**-0.61320**

6.6 Conclusion

We examined the flow of two phase micropolar dusty fluid also containing nanoparticles. The flow occurred due to the exponential stretching of the bounding surface. Considering different surrounding effects along with the above mentioned fluid the substantial outcomes are enlisted below.

- Dust phase temperature and concentration is lower than that of fluid phase.
- Increase in unsteadiness parameter and suction parameter decreases the concentration of nanofluid.
- Micropolar nanofluid increases the rate of heat transfer.
- Thermophoresis parameter and Brownian motion parameter increase the temperature profile while Schmidt number decreases temperature.
- Due to increase in particle rotation the temperature and concentration both decrease.
- Concentration increases with an increase in Thermophoresis parameter whereas it reduces when we increase Brownian motion parameter and Schmidt number.
- The Nusselt number decreases with an increase in Thermophoresis parameter and Brownian motion parameter whereas it increases with an increase in Prandtl number and Schmidt number.

7. Concluding remarks and further study

The research conducted in this thesis has made rich contribution in the field of non-Newtonian fluid mechanics. Explicitly its main focus has been on the mathematical modeling for the micropolar fluid by incorporating different physical geometries. This concluding chapter is a gist of the findings of this thesis and provides road map for further study.

7.1 Summary of the Results

The key outcomes of this research work are outlined below:

- Presence of nanoparticles inside fluid hinders the motion of the fluid but increases its temperature.
- Addition of nano meter sized metallic particles boosts the heat transfer rate.
- Micropolar fluid together with nanoparticles improves the heat transfer rate marginally.
- Porosity parameter boosts the temperature.
- We observe that in the case of hybrid nanofluid the heat transfer rate is substantially high in comparison with simple nanofluid.
- It is also seen a visible increment in the temperature of the micropolar hybrid nanofluid even under the same quantity of nanoparticle volume fraction.
- Due to rotation, the velocity profile decreases of both hybrid and simple nanofluid.
- Local Nusselt number increases due to hybridity as well as with increment in particle volume fraction and vortex viscosity parameter R_1 but decreases with augmentation in rotation and porosity parameter.
- The skin friction coefficients C_{fx} and C_{fy} escalate for increasing values of vortex viscosity parameter R_1, stretching ratio parameter λ, and porosity parameter K_p both in the case of nanofluid and hybrid nanofluid.
- Rotation parameter ε has diminishing impact on C_{fx} whereas opposite behavior is observed in case of C_{fy} for both nanofluid and hybrid nanofluid.

- For stronger magnetic field both linear and angular velocities decrease whereas the temperature increases.
- Entropy generation rate and Bejan number enhance in the presence of Br.
- In two phase fluid-dust suspension dust phase temperature and concentration is lower than that of fluid phase.
- Increase in unsteadiness parameter and suction parameter decreases the concentration of nanofluid.
- Concentration increases with an increase in Thermophoresis parameter whereas it reduces when we increase Brownian motion parameter and Schmidt number.
- The Nusselt number decreases with an increase in Thermophoresis parameter and Brownian motion parameter whereas it increases with an increase in Prandtl number and Schmidt number.
- Sherwood number decreases with an increase in Thermophoresis parameter while it increases with an increase in Brownian motion parameter and Schmidt number.

7.2 Suggestions for Future Work

In this thesis, we have exhibited the mathematical formulation and analytical/numerical solutions for hybrid nanofluid and non-Newtonian micropolar fluid. The outcomes of our computations leave room for further development and expansion in this extremely intriguing new class of nanofluid called hybrid nanofluid along with micropolar fluid model. Here we will talk about a few, however not all, of the numerous conceivable future extensions. Initially, it would be an interesting extension to think about the heat transfer properties of hybrid nanofluid by taking different but suitable compositions of nano particles with micropolar fluid over different surfaces such as cylinder, wedge, curved surfaces, rotating disks, annular pipe and inclined surface etc. which can have a lot of technological and industrial applications. Similarly, there is a great deal of more examination that should be addressed in the field of dusty fluid. For example, the study of 3D dusty fluid in the context of the unsteady boundary-layer flows over a various surfaces. No experimental examinations have yet occurred to the best of our information. Subsequently, the present piece of work obviously persuades the need for comprehensive experimental outcomes to think about for the comparison of this examination.

8. Bibliography

1. A.C. Eringen, Simple microfluids, Intl. J. Eng. Sci., 2(2) (1964) 205-217.
2. A.C. Eringen, Theory of micropolar fluids, J. Math. Mech., 16 (1966) 1-18.
3. G. Lukaszewicz, Micropolar fluids: theory and applications, Birkhäuser, Basel (1999).
4. A.C. Eringen, Microcontinuum Field Theories, II: Fluent Media, Springer, New York 2 (2001).
5. T.C. Chiam, Micropolar fluid flow over a stretching sheet, ZAMM, 62(10) (1982) 565-568.
6. I.A. Hassanien, A.A. Abdullah and R.S.R. Gorla, Numerical solutions for heat transfer in a micropolar fluid over a stretching sheet, Appl. Mech. Eng., 3 (1998) 377-391.
7. N.A. Kelson and A. Desseaux, Effect of surface condition on flow of micropolar fluid driven by a porous stretching sheet, Int. J. Eng. Sci., 39 (2001) 1881-1897.
8. M.A.A. Mahmoud, Thermal radiation effects on MHD flow of a micropolar fluid over a stretching surface with variable thermal conductivity, Physica A, 375 (2007) 401-410.
9. B. Mohanty, S.R. Mishra and H.B. Pattanayak, Numerical investigation on heat and mass transfer effect of micropolar fluid over a stretching sheet through porous media, Alex. Eng. J., 54 (2015) 223-232.
10. S.T. Hussain, S. Nadeem and R.U. Haq, Model-based analysis of micropolar nanofluid flow over a stretching surface, Eur. Phys. J. Plus, 129 (8) (2014) 161.
11. A.J. Chamkha, M. Jaradat and I. Pop, Three- dimensional micropolar flow due to a stretching flat surface, Int. J. Fluid Mech. Res. 30(4) (2003) 357-366.
12. K. Ahmad, R. Nazar, A. Ishaq and I. Pop, Unsteady three-dimensional boundary layer flow due to a stretching surface in a micropolar fluid, Int. J. Numer. Method. Fluids, 68 (2012) 1561-1573.
13. S.T. Mohyud-Din, S.U. Jan, U. Khan and N. Ahmed, MHD flow of radiative micropolar nanofluid in a porous channel: optimal and numerical solutions, Neural. Comput. Appl. (2016) 1-9.

14. M.A. El-Aziz, Viscous dissipation effect on mixed convection flow of a micropolar fluid over an exponentially stretching sheet, Can. J. Phys., 87(4) (2009) 359-368.
15. V.V. Shelukhin and V.V. Neverov, Thermodynamics of micropolar Bingham fluids, J. Non-Newtonian Fluid Mech., 236 (2016) 83-90.
16. S.U.S Choi and J.A. Eastman, Enhancing thermal conductivity of fluids with nanoparticles, ASME Pub. Fed., 231 (1995) 99-106.
17. J. Buongiorno, Convective transport in nanofluids, J. heat transf., 128(3) (2006) 240-250.
18. N. Bachok, A. Ishak and I. Pop, Unsteady boundary-layer flow and heat transfer of a nanofluid over a permeable stretching/shrinking sheet, Int. J. Heat Mass Transf., 55 (2012) 2102-2109.
19. S. Naramgari and C. Sulochana, Dual solutions of radiative MHD nanofluid flow over an exponentially stretching sheet with heat generation/absorption, Appl. Nanosci., 6 (1) (2016) 131-139.
20. R.U. Haq, S. Nadeem, Z.H. Khan, N.S. Akbar, Thermal radiation and slip effects on MHD stagnation point flow of nanofluid over a stretching sheet, Phys. E., 65 (2015) 17-23.
21. P. Besthapu, R. Haq, S. Bandari and Q.M. Al-Mdallal, Mixed convection flow of thermally stratified MHD nanofluid over an exponentially stretching surface with viscous dissipation effect, J. Taiwan Inst. Chem. Eng., 71 (2017) 307-314.
22. S. Nadeem, R.U. Haq and Z.H. Khan, Heat transfer analysis of water-based nanofluid over an exponentially stretching sheet, Alexandria Eng. J., 53 (2014) 219-224.
23. M.H. Abolbashari, N. Freidoonimehr, F. Nazari and M.M. Rashidi, Entropy analysis for an unsteady MHD flow past a stretching permeable surface in nano-fluid, Powder Technol., 267 (2014) 256-267.
24. K. Zaimi, A. Ishak and I. Pop, Boundary layer flow and heat transfer over a nonlinearly permeable stretching/shrinking sheet in a nanofluid, Sci. Rep., 4 (2014) 4404 10.1038/srep04404

25. M. Hatami, M. Sheikholeslami and D.D. Ganji, Laminar flow and heat transfer of nanofluid between contracting and rotating disks by least square method, Powder Technol., 253 (2014) 769-779.
26. M. Sheikholeslami and D.D. Ganji, Heat transfer of Cu-water nanofluid flow between parallel plates, Powder Technol., 235 (2013) 873-879.
27. Y. Xuan and Q. Li, Investigation on convective heat transfer and flow features of nanofluids, J. Heat Transf., 125 (2003) 151-155.
28. H. Masuda, A. Ebata and K. Teramae, Alteration of thermal conductivity and viscosity of liquid by dispersing ultra-fine particles (dispersions of γ-Al_2O_3, SiO_2, and TiO_2 ultra-fine particles), Netsu Bussei (Japan), 4 (1993) 227-233.
29. A.S. Ahuja, Augmentation of heat transport in laminar flow of polystyrene suspensions. I. Experiments and results, J. Appl. Phys., 46(8) (1975) 3408-3416.
30. D. Madhesh, R. Parameshwaran and S. Kalaiselvam, Experimental investigation on convective heat transfer and rheological characteristics of Cu–TiO2 hybrid nanofluids, Exp. Therm. Fluid Sci., 52 (2014) 104-115.
31. M. Hemmat Esfe, A.A. Abbasian Arani, M. Rezaie, W.M. Yan and A. Karimipour, Experimental determination of thermal conductivity and dynamic viscosity of Ag–MgO/water hybrid nanofluid, Int. Commun. Heat Mass, 66 (2015) 189-195.
32. S. Suresh, K.P. Venkitaraj, P. Selvakumar and M. Chandrasekar, Effect of Al2O3–Cu/water hybrid nanofluid in heat transfer, Exp. Therm. Fluid Sci., 38 (2012) 54-60.
33. M.A. Adriana, Hybrid nanofluids based on Al2O3, TiO2 and SiO2: numerical evaluation of different approaches, Int. J. Heat Mass Transfer, 104 (2017), 852-860.
34. G.G. Momin, Experimental investigation of mixed convection with water-Al2O3 & hybrid nanofluid in inclined tube for laminar flow, Int. J. Sci. Technol. Res., 2 (2013) 193-202.
35. M. Mollamahdi, M. Abbaszadeh and G.A. Sheikhzadeh, Flow field and heat transfer in a channel with a permeable wall filled with Al2O3-Cu/water micropolar hybrid nanofluid, effects of chemical reaction and magnetic field, J. Heat Mass Transf. Res., 3(2) (2016) 101-114.

36. S. Suresh, K.P. Venkitaraj, P. Selvakumar and M. Chandrasekar, Synthesis of Al2O3–Cu/water hybrid nanofluids using two step method and its thermo physical properties, Colloids Surf. A: Physicochem. Eng. Asp., 388(1-3) (2011) 41-48.
37. N.A. Che Sidik, I.M. Adamu, M. Mahmud Jamil, G. Kefayati, R. Mamat and G. Najafi, Recent progress on hybrid nanofluids in heat transfer applications: a comprehensive review, Int. Commun. Heat Mass Transf., 78 (2016) 68-79.
38. P.G. Saffman, The stability of laminar flow of a dusty gas, J. Fluid Mech., 13 (1962) 120-128.
39. K. Vajravelu and J. Nayfeh, Hydromagnetic flow of a dusty fluid over a stretching sheet, Int. J. Nonlinear Mech., 27 (1992) 937-945.
40. G.M. Pavithra and B.J. Gireesha, Unsteady flow and heat transfer of a fluid particle suspension over an exponentially stretching sheet, Ain Shams Eng. J., 5 (2014) 613-624.
41. B.J. Gireesha, B. Mahanthesh and R.S.R. Gorla, Suspended particle effect on nanofluid boundary layer flow past a stretching surface, J. Nanofluids, 3 (2014) 1-11.
42. H.I. Andersson, MHD flow of a visco-elastic fluid past a stretching surface, Acta Mechanica, 95 (1992) 227-230.
43. M.Q. Al-Odat, R.A. Damseh and T.A. Al-Azab, Thermal boundary layer on an exponentially stretching continuous surface in the presence of magnetic field effect, Int. J. Appl. Mech. Eng., 11(2) (2006) 289-299.
44. A. Ishak, MHD boundary layer flow due to an exponentially stretching sheet with radiation effect, Sains Malays., 40(4) (2011) 391-395.
45. M. Sheikholeslami, M. Hatami and D.D. Ganji, Analytical investigation of MHD nanofluid flow in a semi-porous channel, Powder Technol., 246 (2013) 327-336.
46. D. Lu, M. Ramzan, S. Ahmad, J.D. Chung and U. Farooq, A numerical treatment of MHD radiative flow of micropolar nanofluid with homogeneous-heterogeneous reactions past a nonlinear stretched surface, Sci. Rep., 8(1) (2018) 12431, https://doi.org/10.1038/s41598-018-30965-x.
47. F.S. Ibrahim, A.M. Elaiw and A.A. Bakr, Influence of viscous dissipation and radiation on unsteady MHD mixed convection flow of micropolar fluids, Appl. Math. Inf. Sci., 2 (2008) 143-162.

48. E.M.A. Elbashbeshy, T.G. Emam and K.M. Abdelgaber, Effects of thermal radiation and magnetic field on unsteady mixed convection flow and heat transfer over an exponentially stretching surface with suction in the presence of internal heat generation/absorption, J. Egypt. Math. Soc., 20 (2012) 215-222.
49. H.I. Andersson, J.B. Aarseth, N. Braud and B.S. Dandapat, Flow of a power-law fluid film on unsteady stretching surface, J. Non-Newtonian Fluid Mech., 62 (1996) 1-8.
50. A. Malvandi, F. Hedayati and D.D. Ganji, Slip effects on unsteady stagnation point flow of a nano fluid over a stretching sheet, Powder Technol., 253 (2014), 377-384.
51. S.F. Ahmmed, R. Biswas and M. Afikuzzaman, Unsteady Magnetohydrodynamic Free Convection Flow of Nanofluid Through an Exponentially Accelerated Inclined Plate Embedded in a Porous Medium with Variable Thermal Conductivity in the Presence of Radiation, J. Nanofluids, 7(5) (2018) 891-901.
52. A. Bejan, Entropy Generation Through Heat and Fluid Flow, John Wiley & Sons Inc., Canada (1994).
53. A. Bejan, Entropy Generation Minimization, CRC Press, Boca Raton, New York, USA (1996).
54. G.C. Shit, R. Haldar and S. Mandal, Entropy generation on MHD flow and convective heat transfer in a porous medium of exponentially stretching surface saturated by nanofluids, Adv. Powder Technol., 28 (2017) 1519-1530.
55. N. Dalir, M. Dehsara and S.S. Nourazar, Entropy analysis for magnetohydrodynamic flow and heat transfer of a Jeffrey nanofluid over a stretching sheet, Energy, 79 (2015) 351-362.
56. L.S. Maganti and P. Dhar, Consequences of flow configuration and nanofluid transport on entropy generation in parallel microchannel cooling systems, Int. J. Heat Mass Transfer, 109 (2017) 555-563.
57. S. Malik and A.K. Nayak, MHD convection and entropy generation of nanofluid in a porous enclosure with sinusoidal heating, Int. J. Heat Mass Transfer, 111 (2017) 329-345.

58. T. Hayat, M. Rafiq, B. Ahmad and S. Asghar, Entropy generation analysis for peristaltic flow of nanoparticles in a rotating frame, Int. J. Heat Mass Transfer, 108 (2017) 1775-1786.
59. Y. Wang, Z. Chen and X. Ling, Entropy generation analysis of particle suspension induced by Couette flow, Int. J. Heat Mass Transfer, 90 (2015) 499-504.
60. G.C. Shit, R. Haldar and S. Mandal, Entropy generation on MHD flow and convective heat transfer in a porous medium of exponentially stretching surface saturated by nanofluids, Adv. Powder Technol., 28 (2017) 1519-1530.
61. M. Sheikholeslami and D.D. Ganji, Entropy generation of nanofluid in presence of magnetic field using lattice Boltzmann method, Physica A, 417 (2015) 273-286.
62. M.T. Kamel, D. Roach and M.H. Hamdan, On the Micropolar Fluid Flow through Porous Media, Mathematical Methods, System Theory and Control, Proceedings of the 11th MAMECTIS ’09, 978-960-474-094-9, WSEAS Press (2009) 190-197.
63. M.W. Heruska, L.T. Watson and K.K. Sankara, Micropolar flow past a porous stretching sheet, Comput. Fluids, 14 (1986) 117-129.
64. S. Nadeem, Rizwan Ul Haq, N.S. Akbar and Z.H. Khan, MHD three-dimensional Casson fluid flow past a porous linearly stretching sheet, Alexandria Eng. J., 52 (2013) 577-582.
65. H. Hashemi, Z. Namazian and S.A. Mehryan, Cu-water micropolar nanofluid natural convection within a porous enclosure with heat generation, J. Mol. Liq., 236 (2017) 48-60.
66. N.A. Sheikh, F. Ali, I. Khan, M. Saqib and A. Khan, MHD flow of micropolar fluid over an oscillating vertical plate embedded in porous media with constant temperature and concentration, Math. Prob. Eng., (2017).
67. M. Turkyilmazoglu, Flow of a micropolar fluid due to a porous stretching sheet and heat transfer, Int. J. Non-Linear Mech., 83 (2016) 59-64.
68. J.H. Merkin, On dual solutions occurring in mixed convection in a porous medium, J. Eng. Math., 20 (1986) 171-179.

69. P.D. Weidman, D.G. Kubitschek, and A.M.J. Davis, The effect of transpiration on self-similar boundary layer flow over moving surfaces, Int. J. Eng. Sci., 44 (2006) 730-737.
70. A.V. Roşca, and I. Pop, Flow and heat transfer over a vertical permeable stretching/shrinking sheet with a second order slip, Int. J. Heat Mass Transf., 60 (2013) 355-364.
71. L.F. Shampine, J. Kierzenka and M.W. Reichelt, Solving boundary value problems for ordinary differential equations in MATLAB with bvp-4c, (2000) 1-27.
72. S. Liao, An optimal homotopy-analysis approach for strongly nonlinear differential equations, Commun. Nonlinear Sci. Numer. Simul., 15 (2010) 2003–2016

Turnitin Originality Report

Boundary Layer Flow of Micropolar Fluid by an Exponentially Stretching Surface by turnitin
Maryam Subhani .

From DRSM (DRSML)

- Processed on 16-Mar-2020 11:39 PKT
- ID: 1276330278
- Word Count: 26125

Similarity Index
18%
Similarity by Source

Internet Sources:
10%
Publications:
11%
Student Papers:
12%

Focal Person (Turnitin)
Quaid-i-Azam University
Islamabad

sources:

1 1% match (student papers from 02-Jan-2015)
Submitted to Higher Education Commission Pakistan on 2015-01-02

2 < 1% match (Internet from 31-Jan-2020)
https://res.mdpi.com/bookfiles/book/685/Recent_Developments_of_Nanofluids.pdf?v=1580528305

3 < 1% match (publications)
S.S. Ghadikolaei, Kh. Hosseinzadeh, M. Yassari, H. Sadeghi, D.D. Ganji, "Boundary layer analysis of micropolar dusty fluid with TiO 2 nanoparticles in a porous medium under the effect of magnetic field and thermal radiation over a stretching sheet", Journal of Molecular Liquids, 2017

4 < 1% match (publications)
Gowdara M. Pavithra, Bijjanal J. Gireesha, "Unsteady flow and heat transfer of a fluid-particle suspension over an exponentially stretching sheet", Ain Shams Engineering Journal, 2014

5 < 1% match (Internet from 30-Jun-2018)
https://link.springer.com/content/pdf/10.1140%2Fepje%2Fi2018-11682-y.pdf

6 < 1% match (student papers from 03-Dec-2017)
Submitted to Universiti Teknologi Petronas on 2017-12-03

7 < 1% match (publications)
M.R. Krishnamurthy, B.C. Prasannakumara, B.J. Gireesha, Rama S.R. Gorla, "Effect of viscous dissipation on hydromagnetic fluid flow and heat transfer of nanofluid over an exponentially stretching sheet with fluid-particle suspension", Cogent Mathematics, 2015

8 < 1% match (publications)
S Rawat, "Transient magneto-micropolar free convection heat and mass transfer through a non-Darcy porous medium channel with variable thermal conductivity and heat source effects", Proceedings of the Institution of Mechanical Engineers Part C Journal of Mechanical Engineering Science, 10/01/2009

9 < 1% match (student papers from 07-Aug-2017)
Submitted to Higher Education Commission Pakistan on 2017-08-07